Title 40 CFR Part 191
Subparts B and C
Compliance Recertification Application 2026
for the
Waste Isolation Pilot Plant
Appendix GEOCHEM-2026
Implementation of Chemistry Conceptual Models

United States Department of Energy
Waste Isolation Pilot Plant

Carlsbad Field Office
Carlsbad, New Mexico

Compliance Recertification Application 2026
Appendix GEOCHEM-2026
Implementation of Chemistry Conceptual Models

Table of Contents

GEOCHEM-1.0 INTRODUCTION 1

GEOCHEM-1.1 WIPP Chemistry and Actinide Release 2
GEOCHEM-1.1.1 Brine Volumes 3
GEOCHEM-1.1.2 Actinide Carrying Capacity 3

GEOCHEM-1.2 Changes since CRA-2019 4

GEOCHEM-2.0 GAS GENERATION 4

GEOCHEM-2.1 Gas Generation Conceptual Model 4
GEOCHEM-2.1.1 Homogeneous Gas Generation 4
GEOCHEM-2.1.2 Oxygen Depletion and Temperature 4
GEOCHEM-2.1.3 Corrosion of Ferrous Metals 5
GEOCHEM-2.1.4 Corrosion of Non-Ferrous Metals 5
GEOCHEM-2.1.5 Microbial Degradation of CPR 5
GEOCHEM-2.1.6 Steel Passivation 6
GEOCHEM-2.1.7 MgO Hydration and Carbonation 6
GEOCHEM-2.1.8 Hydromagnesite Conversion to Magnesite 6
GEOCHEM-2.1.9 Radiolysis 6

GEOCHEM-2.2 Gas Generation Process Models 6
GEOCHEM-2.2.1 Process Model for Corrosion of Ferrous Metals 7
GEOCHEM-2.2.2 Process Model for Microbial Degradation of CPR 9
GEOCHEM-2.2.3 Process Model for MgO Hydration and Carbonation 10
GEOCHEM-2.2.4 Process Model for Hydromagnesite to Magnesite Conversion 11
GEOCHEM-2.2.5 Process Model for Radiolysis 11

GEOCHEM-2.3 Parameterization of the Gas Generation Process Models 12
GEOCHEM-2.3.1 Parameters for Corrosion of Ferrous Metals 12
GEOCHEM-2.3.2 Parameters for Microbial Gas Generation 13
GEOCHEM-2.3.3 Parameters for MgO Hydration and Carbonation 13
GEOCHEM-2.3.4 Parameters for Hydromagnesite Conversion to Magnesite 13
GEOCHEM-2.3.5 Parameters for Radiolysis 14

GEOCHEM-2.4 Gas Generation Uncertainty Quantification 14
GEOCHEM-2.4.1 Corrosion of Ferrous Metals 14
GEOCHEM-2.4.2 Microbial Degradation of CPR 14
GEOCHEM-2.4.3 MgO Hydration Rate 15
GEOCHEM-2.4.4 Hydromagnesite Conversion Rate 15
GEOCHEM-2.4.5 Radiolysis 15

GEOCHEM-2.5 Summary of Updates since CRA-2019 16

GEOCHEM-3.0 CHEMICAL CONDITIONS 16

GEOCHEM-3.1 Representation of WIPP Chemical Conditions 18
GEOCHEM-3.1.1 Ionic Strength, Brine pH, pcH, pmH, E_h, and Fugacity of CO_2 19
GEOCHEM-3.1.2 Salado and Castile Minerals 20
GEOCHEM-3.1.3 Salado and Castile Brines 20
GEOCHEM-3.1.4 Magnesium Oxide 21
GEOCHEM-3.1.5 Organic Ligands 21
GEOCHEM-3.1.6 Borate 21

GEOCHEM-3.1.7 Lead 21
GEOCHEM-3.1.8 Iron 22
GEOCHEM-3.2 Parameterization of the Chemical Conditions Process Model 22
GEOCHEM-3.2.1 Salado and Castile Mineral Parameters 22
GEOCHEM-3.2.2 Salado and Castile Brine Parameters 23
GEOCHEM-3.2.3 Magnesium Oxide Parameters 27
GEOCHEM-3.2.4 Organic Ligand Parameters 27
GEOCHEM-3.2.5 Borate Parameters 30
GEOCHEM-3.2.6 Lead Parameters 31
GEOCHEM-3.2.7 Iron Parameters 32
GEOCHEM-3.3 Chemical Conditions Uncertainty Quantification 33
GEOCHEM-3.4 Summary of Updates since CRA-2019 34
GEOCHEM-4.0 DISSOLVED ACTINIDE SOURCE TERM 34
GEOCHEM-4.1 Dissolved Actinide Source Term Conceptual Model 34
GEOCHEM-4.1.1 A Well-Mixed Repository at Equilibrium 35
GEOCHEM-4.1.2 Use of the Pitzer Model 35
GEOCHEM-4.1.3 Use of Standard Brines 36
GEOCHEM-4.1.4 Oxidation-state Analogy 36
GEOCHEM-4.1.5 Redox State of the Actinides 37
GEOCHEM-4.1.6 Effect of Organic Ligands 37
GEOCHEM-4.1.7 Immobile Substrates 38
GEOCHEM-4.1.8 Phase Stability/Crystallinity 38
GEOCHEM-4.1.9 Solubility-Controlling Phases 38
GEOCHEM-4.2 Dissolved Actinide Source Term Process Models 39
GEOCHEM-4.2.1 +III Actinides 39
GEOCHEM-4.2.2 +IV Actinides 40
GEOCHEM-4.2.3 +V Actinides 42
GEOCHEM-4.3 Parameterization of Dissolved Actinide Source Term Process Models 42
GEOCHEM-4.3.1 +III Actinide Parameters 43
GEOCHEM-4.3.2 +IV Actinide Parameters 48
GEOCHEM-4.3.3 +V Actinide Parameters 49
GEOCHEM-4.4 Dissolved Actinide Source Term Uncertainty Quantification 50
GEOCHEM-4.4.1 Conceptual Model Uncertainty 50
GEOCHEM-4.4.2 Process Model Uncertainty 51
GEOCHEM-4.4.3 Dissolved Actinide Source Term Uncertainty Analysis from Recent Technical Literature 54
GEOCHEM-4.4.4 Alternative Analysis of Actinide Uncertainty 60
GEOCHEM-4.5 Summary of Updates since CRA-2019 60
GEOCHEM-5.0 COLLOIDAL ACTINIDE SOURCE TERM 60
GEOCHEM-5.1 Colloidal Actinide Source Term Conceptual Model 60
GEOCHEM-5.2 Colloidal Actinide Source Term Process Model 61
GEOCHEM-5.2.1 Mineral Fragment Colloids Process Model 62
GEOCHEM-5.2.2 Intrinsic Colloids Process Model 63
GEOCHEM-5.2.3 Humic Substance Colloids Process Model 63
GEOCHEM-5.2.4 Microbial Colloids Model 64

GEOCHEM-5.3 Parameterization of Colloidal Actinide Source Term Process Model 64
GEOCHEM-5.3.1 Mineral Fragment Colloids Model Parameterization 66
GEOCHEM-5.3.2 Intrinsic Colloids Model Parameterization 67
GEOCHEM-5.3.3 Humic Colloids Model Parameterization 67
GEOCHEM-5.3.4 Microbial Colloids Model Parameterization 69
GEOCHEM-5.4 Quantification of Uncertainty in the Colloids Source Term Model 71
GEOCHEM-5.4.1 Mineral Fragment Colloids Model Uncertainty 71
GEOCHEM-5.4.2 Intrinsic Colloids Model Uncertainty 71
GEOCHEM-5.4.3 Humic Colloids Model Uncertainty 72
GEOCHEM-5.4.4 Microbial Colloids Model Uncertainty 73
GEOCHEM-5.5 Summary of Updates since CRA-2019 74
GEOCHEM-6.0 REFERENCES 74

List of Tables

Table GEOCHEM-1. Chemistry-related Conceptual and Process Models....2

Table GEOCHEM-2. Composition of GWB and ERDA-6 Brine before Reaction with Anhydrite, Brucite and Hydromagnesite. 18

Table GEOCHEM-3. Salado and Castile Mineral Dissolution Reactions for CRA-2026 22

Table GEOCHEM-4. Salado and Castile Brine Dissociation Reactions for CRA-2026....23

Table GEOCHEM-5. Pitzer Interactions for Salado and Castile Brines for CRA-2026 25

Table GEOCHEM-6. Pitzer Interactions for Salado and Castile Brines for CRA-2026 Continued ..26

Table GEOCHEM-7. MgO Solid Dissolution Reactions for CRA-2026....27

Table GEOCHEM-8. EDTA Reactions for CRA-2026....28

Table GEOCHEM-9. Citrate Reactions for CRA-2026 28

Table GEOCHEM-10. Oxalate, Lactate, and Acetate Reactions for CRA-2026 28

Table GEOCHEM-11. Organic Ligand Pitzer Interactions for CRA-2026 29

Table GEOCHEM-12. Borate Reactions for CRA-2026 30

Table GEOCHEM-13. Pitzer Interactions for Borate for CRA-2026....31

Table GEOCHEM-14. Lead Reactions for CRA-2026....31

Table GEOCHEM-15. Pitzer Interactions for Lead for CRA-2026 32

Table GEOCHEM-16. Iron Reactions for CRA-2026....32

Table GEOCHEM-17. Pitzer Interactions for Iron for CRA-2026 33

Table GEOCHEM-18. Dissolution and Dissociation Reactions for Americium Solids and Species for CRA-2026. 39

Table GEOCHEM-19. Dissolution and Dissociation Reactions for Thorium Solids and Species for CRA-2026. 41

Table GEOCHEM-20. Dissolution and Dissociation Reactions for Neptunium Solids and Species for CRA-2026. 42

Table GEOCHEM-21. Actinide Solubilities (M) for CRA-2026. CRA-2019 DPA values in parentheses. 43

Table GEOCHEM-22. Amorphous Am(III) - Hydroxide Log K values and Pitzer parameters for the $Nd(OH)_3(s)$ - $MgCl_2$ - H_2O system. From Jang et al. (2021). 47

Table GEOCHEM-23. Pitzer Interactions for Am^{3+} for CRA-2026....48

Table GEOCHEM-24. Pitzer Interactions for Th^{4+} for CRA-2026 49

Table GEOCHEM-25. Pitzer Interactions for NpO_2^+ for CRA-2026....50

Table GEOCHEM-26. Comparison of Actinide Solubilities (M) for Compliance-Related Calculations from the CCA to CRA-2026. 52

Table GEOCHEM-27. WIPP Colloid Model Parameter Summary and Description 65

Table GEOCHEM-28. WIPP Colloid Parameter Values Used in CRA-2026 Final-State (FS) and Interim-State (IS) (Kaplan et al. 2025; Mariner 2025a, 2025b). 66

List of Figures

Figure GEOCHEM-1. pH-Dependent An(III) Solubility for 5.0 M NaCl (left) and 0.25 M $MgCl_2$ and $CaCl_2$ Solutions (right). Measured Data (dark blue diamonds, pink squares) and EQ3/6 Simulations (all others) of amorphous (am) Am-hydroxide phase (more soluble) and crystalline aged (cr-aged) Am-hydroxide phase (less soluble) displayed by matrix cation (Figure 1D and Figure 2A from [Domski 2022]). 44

Figure GEOCHEM-2. An(III) Models Compared to Measured An(III) Data 46

Figure GEOCHEM-3. Histogram of the Difference D = log10 Sm – log10 Sp for Am(III) 57

Figure GEOCHEM-4. CDF of the Difference D = log10 Sm – log10 Sp for Am(III) 58

Figure GEOCHEM-5. Histogram of the Difference D = log10 Sm – log10 Sp for Th(IV) 59

Figure GEOCHEM-6. CDF Plot for the CRA-2026 of the Difference D = log10 Sm – log10 Sp for Th(IV). 59

ACRONYMS AND ABBREVIATIONS

%	percent
A	surface area
α	alpha particle
am	amorphous
aq	aqueous
β	(apparent) stability constant, or beta particle
B_{fc}	parameter to account for the uncertainty in microbial gas generation
°C	Celsius; centigrade
c	concentration
CAPHUM	maximum (cap) actinide concentration associated with mobile humic colloids
CAPMIC	maximum actinide concentration that could be associated with microbes
CCA	Compliance Certification Application
CDF	cumulative distribution function
CFR	Code of Federal Regulations
cm	centimeter
CONCINT	actinide concentration associated with mobile actinide intrinsic colloids
CONCMIN	actinide concentration associated with mobile mineral fragment colloids
CPR	cellulosic, plastic, and rubber materials
cr	crystalline phase
CRA	Compliance Recertification Application
DBR	direct brine release
D_c	mass concentration of cellulosics; (material mass)/(disposal volume)
D_{HM}	mass concentration of MgO; (hydromagnesite mass)/(disposal volume)
DLVO	Derjaguin-Landau-Verwey-Overbeek
D_m	mass concentration of MgO; (MgO mass)/(disposal volume)

DOE	U.S. Department of Energy
DRZ	Disturbed Rock Zone
D_s	surface area concentration of steel; (surface area steel)/(disposal volume)
EDTA	ethylenediaminetetraacetic acid
Eh	Oxidation-reduction (redox) potential relative to the standard hydrogen electrode
EPA	U.S. Environmental Protection Agency
EQ3/6	software program for geochemical modeling of aqueous systems
EQ3NR	An aqueous solution speciation-solubility modeling code
ERDA	Energy Research and Development Administration
eV	electron volt
F	Fahrenheit or function containing fγ and ionic strength derivatives of Pitzer model 2nd virial coefficient terms
FA-Suw	Suwannee River fulvic acid
f_{CO2}	fugacity of carbon dioxide
F_{NO3}, F_{SO4}	fraction of carbon consumed through microbial denitrification or sulfate reduction
g	gamma radiation or activity coefficient, or gaseous, or gram, or gravity of Earth
G	molecular yield in molecules/100 eV of absorbed ionizing radiation or Gibbs free energy (Gxs is excess or non-ideal contribution to Gibbs free energy)
GWB	Generic Weep Brine
HAal-Gor	Gorleben humic acid
HAal-LBr	Lake Bradford humic acid
I	ionic strength
K	degree Kelvin or stability constant
kg	kilogram
L	liter

LANL	Los Alamos National Laboratory
log	logarithm
M	mole per liter
m	meter, molal
m^2	square meter
m^3	cubic meter
meq	milliequivalents
meV	millielectron volts
mg	milligram
min	minimum
mM	millimole per liter
mol	mole
m/s	meters per second
N	degree of polymerization number
n	neutron, number, or number of moles
nm	Nanometer
PA	performance assessment
PABC	Performance Assessment Baseline Calculation
PAIR	Performance Assessment Inventory Report
PAVT	Performance Assessment Verification Test
pC_{H+} or pcH	Negative logarithm of H+ concentration in moles per liter
pH	negative logarithm of H+ activity
PHUMCIM	Proportionality constant for the actinide concentration associated with mobile humic colloids, in Castile brine
PHUMSIM	Proportionality constant for the actinide concentration associated with mobile humic colloids, in Salado brine
pmH	negative logarithm of H+ concentration in molal

ppm	parts per million
PROPMIC	proportionality constant describing the bioassociation of actinides with mobile microorganisms
qr	gas (qrg), brine (qrb) generation rates by corrosion, sulfidation, microbes, MgO, or hydromagnesite – trailing subscripted c, s, m, h, & hc, respectively
Q	Ion activity product in the SI = log Q/K expression
ρ	Density
R_c	corrosion rate in either inundated (Rci) or humid air (Rch)
redox	Oxidation-reduction
R_h	MgO hydration rate in either inundated (Rhi) or humid air (Rhh)
R_{hc}	rate of conversion of hydromagnesite to magnesite
R_m	biodegradation rate in either inundated (Rmi) or humid air (Rmh)
RPPCR	Replacement Panels Planned Change Request
s	solid or second
Sb	brine saturation
SI	Saturation Index (SI) = log Q/K; Q = ion activity product, K = stability constant
SNL	Sandia National Laboratories
SOTERM	Actinide Chemistry Source Term (WIPP)
SPC	Salado Primary Constituents
TDS	Total dissolved solids
TIC	Total Inorganic Carbon
V	volt, vanadium, or volume
WIPP	Waste Isolation Pilot Plant
X	stoichiometric coefficient for gas generation by corrosion, microbes, MgO hydration, or hydromagnesite conversion – trailing subscripted c, m, h, & hc, respectively
XANES	X-ray absorption near-edge spectroscopy

Z	sum of products for each species' molality multiplied by absolute value of its valence charge
z_s	valence charge of solute species s

ELEMENTS AND CHEMICAL COMPOUNDS

Al	Aluminum
Am	Americium
Am^{3+}	Americium cation in the +3 oxidation state
$AmCl^{2+}$	Americium (III) chloride ion – (1:1) complex
$AmCl_2^{+}$	Americium (III) chloride ion – (1:2) complex
$AmCO_3^{+}$	Americium (III) carbonate ion – (1:1) complex
$Am(CO_3)_2^{2-}$	Americium (III) carbonate ion – (1:2) complex
$Am(CO_3)_3^{3-}$	Americium (III) carbonate ion – (1:3) complex
$Am(CO_3)_4^{5-}$	Americium (III) carbonate ion – (1:4) complex
$AmOH^{2+}$	Americium (III) hydroxide ion – (1:1) complex
$Am(OH)_2^{+}$	Americium (III) hydroxide ion – (1:2) complex
$Am(OH)_3$	Americium hydroxide
$AmOHCO_3$	Americium (III) hydroxycarbonate
$AmSO_4^{+}$	Americium (III) sulfate ion – (1:1) complex
$Am(SO_4)_2^{-}$	Americium (III) sulfate ion – (1:2) complex
An	Actinide
An(III)	General actinide in the +3 oxidation state
An(IV)	General actinide in the +4 oxidation state
An(V)	General actinide in the +5 oxidation state
An(VI)	General actinide in the +6 oxidation state
AnHS	Actinide (III) hydrogen sulfide
$B(OH)_3$	Hydroxyborate, boric acid
$B(OH)_4^{-}$	Orthoborate, tetrahydroxyborate anion
$B_3O_3(OH)_4^{-}$	Triborate anion
$B_4O_5(OH)_4^{2-}$	Tetraborate anion
Br^{-}	Bromide anion
C	Carbon or concentration
Ca	Calcium
Ca^{2+}	Calcium cation
$CaB(OH)_4^{+}$	Calcium boron hydroxide

$CaCl_2$	Calcium chloride
$CaCl_2 \bullet 4H_2O$	Calcium dichloride tetrahydrate
$Ca_2Cl_2(OH)_2 \bullet H_2O$	Calcium hydroxychloride
$Ca_4Cl_2(OH)_6 \bullet 13H_2O$	Calcium hydroxychloride triskaidecahydrate
$CaCO_3$	Calcium carbonate, aragonite, calcite
$C_6H_{10}O_5$	Cellulose
$CaMg(CO_3)_2$	Calcium magnesium carbonate, dolomite
$CaNa_2(CO_3)_2 \bullet 5H_2O$	Calcium sodium carbonate pentahydrate, gaylussite
$Ca(OH)_2$	Calcium hydroxide, portlandite
$CaOxalate \bullet 2H_2O$	whewellite
$CaSO_4$	Calcium sulfate, anhydrite
$CaSO_4 \bullet 2H_2O$	Calcium sulfate dihydrate, gypsum
Cl	Chlorine
Cl^-	Chloride anion
ClO_4^-	Perchlorate anion
Cm(III)	Curium in the +3 oxidation state
CO_2	Carbon dioxide
CO_3^{2-}	Carbonate anion
Fe	Iron
Fe^{2+}	Iron cation in the +2 oxidation state, ferrous cation
$Fe_2Cl(OH)_3$	Ferrous iron chloride trihydroxide, hibbingite
$FeCO_3$	Iron (II) carbonate, ferrous carbonate, siderite
$Fe(CO_3)_2^{2-}$	Ferrous iron carbonate dianion
$Fe_2CO_3(OH)_2$	Ferrous iron carbonate dihydroxide, chukanovite
Fe_3O_4	Magnetite, iron (II,III) oxide
$FeOH^+$	Ferrous iron hydroxide ion
$Fe(OH)_2$	Ferrous iron hydroxide
$Fe(OH)_3^-$	Ferrous iron trihydroxide ion
$Fe(OH)_4^{2-}$	Ferrous iron tetrahydroxide ion
FeS	Iron (II) sulfide, mackinawite
$FeSO_4$	Ferrous iron sulfate

$FeSO_4•H_2O$	Ferrous iron sulfate monohydrate, szomolnokite
$FeSO_4•7H_2O$	Ferrous iron sulfate heptahydrate, melanterite
H^+	Hydrogen cation
H_2	Hydrogen
HCO_3^-	Bicarbonate anion, hydrogen carbonate anion
H_2O	Water
HSO_4^-	Hydrogen sulfate anion
K	Potassium
K+	Potassium cation
$KB_5O_8•4H_2O$	Potassium pentaborate
$K_2B_4O_7•4H_2O$	Potassium tetraborate
$K_2Ca(SO_4)2•H_2O$	Potassium calcium sulfate hydrate, syngenite
KCl	Potassium chloride, sylvite
$KHCO_3$	Potassium bicarbonate, kalicinite
$K_8H_4(CO_3)_6•3H_2O$	Potassium bicarbonate trihydrate
$KHSO_4$	Potassium bisulfate, mercallite
$K_8H_6(SO_4)_7$	Potassium hydrogen sulfate, misenite
$K_2MgCa_2(SO_4)_4•2H_2O$	Potassium magnesium calcium sulfate dihydrate, polyhalite
$KMgCl_3•6H_2O$	Potassium magnesium chloride hexahydrate, carnallite
$KMgClSO_4•3H_2O$	Potassium magnesium chloride sulfate trihydrate, kainite
$K_2Mg(SO_4)2•4H_2O$	Potassium magnesium sulfate tetrahydrate, leonite
$KNaCO_3•6H_2O$	Potassium sodium carbonate hexahydrate
$K_2NaH(CO_3)_2•2H_2O$	Potassium sodium bicarbonate dihydrate, trona
$KNpO_2CO_3$	Potassium neptunium (V) oxide carbonate – (1:1:1) complex
K_2SO_4	Potassium sulfate, arcanite
Mg^{2+}	Magnesium cation
$MgB(OH)_4^+$	Magnesium orthoborate ion
$Mg_2CaCl_6•12H_2O$	Magnesium calcium chloride dodecahydrate, tachyhydrite
$MgCl_2•6H_2O$	Magnesium chloride hexahydrate, bischofite
$Mg_2Cl(OH)_3•4H_2O$	Magnesium hydroxychloride tetrahydrate, phase 3, korshunovskite

$Mg_3Cl(OH)_5•4H_2O$	Magnesium hydroxychloride tetrahydrate, phase 5
$MgCO_3$	Magnesium carbonate, magnesite
$MgCO_3•3H_2O$	Magnesium carbonate trihydrate, nesquehonite
$Mg_4(CO_3)_3(OH)_2•3H_2O$	Magnesium carbonate hydroxide trihydrate, hydromagnesite-4323
$Mg_5(CO_3)_4(OH)_2•4H_2O$	Magnesium hydroxycarbonate tetrahydrate, hydromagnesite-5424
MgO	Magnesium oxide, periclase
$Mg(OH)_2$	Magnesium hydroxide, brucite
$MgOH^+$	Magnesium hydroxide ion
$MgSO_4$	Magnesium sulfate
$MgSO_4•H_2O$	Magnesium sulfate hydrate, kierserite
$MgSO_4•6H_2O$	Magnesium sulfate hexahydrate, hexahydrite
$MgSO_4•7H_2O$	Magnesium sulfate heptahydrate, epsomite
N_2	Nitrogen
Na	Sodium
Na^+	Sodium cation
$NaAm(CO_3)_2$	Sodium americium (III) carbonate
$NaAm(CO_3)_2•6H_2O$	Sodium americium (III) carbonate hexahydrate
$Na_2B_4O_7•10H_2O$	Sodium tetraborate decahydrate, borax
$NaB_5O_8•5H_2O$	Sodium pentaborate hexahydrate
$NaBO_2•4H_2O$	Sodium metaborate tetrahydrate
$NaBO_2•NaCl•2H_2O$	Sodium metaborate sodium chloride dihydrate, teepleite
$Na_2Ca(CO_3)_2•2H_2O$	Sodium calcium carbonate dihydrate, pirssonite
$Na_2Ca(SO_4)_2$	Sodium calcium disulfate, glauberite
$Na_4Ca(SO_4)_3•2H_2O$	Sodium calcium trisulphate dihydrate, labile salt
NaCl	Sodium chloride, halite
$Na_2CO_3•H_2O$	Sodium carbonate hydrate, thermonatrite
$Na_2CO_3•7H_2O$	Sodium carbonate heptahydrate
$Na_2CO_3•10H_2O$	Sodium carbonate decahydrate, natron
$Na_6CO_3(SO_4)_2$	Sodium carbonate sulfate tetrahydrate, burkeite
$NaHCO_3$	Sodium bicarbonate, nahcolite

$Na_3H(CO_3)_2 \bullet 2H_2O$	Sodium hydrogen carbonate, trona
$Na_3H(SO_4)_2$	Sodium hydrogen disulphate
$NaK_3(SO_4)_2$	Sodium potassium disulphate, Aphthitalite, Glaserite
$Na_2Mg(SO_4)_2 \bullet 4H_2O$	Sodium magnesium sulfate tetrahydrate, bloedite
$NaNpO_2CO_3 \bullet 3.5H_2O$	Sodium neptunium (V) oxide carbonate hydrate – (1:1:1) complex
$Na_3NpO_2(CO_3)_2$	Sodium neptunium (V) oxide carbonate – (3:1:2) complex
$NaPb_2(CO_3)_2(OH)$	Sodium lead hydroxycarbonate, Abellaite
Na_2SO_4	Sodium sulfate, thenardite
$Na_2SO_4 \bullet 10H_2O$	Sodium sulfate decahydrate, mirabilite
Nd	Neodymium
$Nd(OH)_3$	Neodymium (III) hydroxide
NO_3^-	Nitrate anion
Np	Neptunium
$NpO_2CO_3^-$	Neptunium (V) oxide carbonate ion – (1:1) complex
$NpO_2(CO_3)_2^{3-}$	Neptunium (V) oxide carbonate ion – (1:2) complex
$NpO_2(CO_3)_3^{5-}$	Neptunium (V) oxide carbonate ion – (1:3) complex
NpO_2OH	Neptunium (V) oxide hydroxide
$NpO_2(OH)_2^-$	Neptunium (V) oxide hydroxide ion – (1:2) complex
O	Oxygen
O_2	Molecular oxygen
OH^-	Hydroxide anion
Pb	Lead
Pb^{2+}	Lead cation in the +2 oxidation state
$PbCl_2$	Lead (II) chloride
$PbCl^+$	Chloridoplumbate (II) ion
$PbCl_3^-$	Trichloridoplumbate (II) ion
$PbCO_3$	Lead (II) carbonate, cerussite
$Pb(CO_3)_2^{2-}$	Lead (II) carbonate ion
$Pb(CO_3)(OH)$	Lead hydroxy carbonate, hydrocerussite
$Pb(OH)_2$	Lead (II) hydroxide
Pu	Plutonium

SO_4^{2-}	Sulfate anion
Th^{4+}	Thorium cation in the +4 oxidation state
$Th(CO_3)_5^{6-}$	Thorium (IV) pentacarbonyl ion complex
ThO_2	Thorium dioxide
$Th(OH)_2^{2+}$	Thorium (IV) hydroxide ion – (1:2) complex
$Th(OH)_3^{+}$	Thorium (IV) hydroxide ion – (1:3) complex
$Th(OH)_4$	Thorium hydroxide
$Th_4(OH)_{12}^{4+}$	Thorium (IV) hydroxide ion – (4:12) complex
$Th_6(OH)_{15}^{9+}$	Thorium (IV) hydroxide ion – (6:15) complex
$Th(SO_4)_3^{2-}$	Thorium (IV) sulfate ion – (1:3) complex
$Th(SO_4)_2$	Thorium (IV) sulfate
$Th(SO_4)_2 \bullet 8H_2O$	Thorium (IV) sulfate octahydrate
$Th(SO_4)_2 \bullet 9H_2O$	Thorium (IV) sulfate enneahydrate
$Th(SO_4)_2 \bullet Na_2SO_4 \bullet 6H_2O$	Thorium (IV) sulfate sodium sulfate hexahydrate

GEOCHEM-1.0 INTRODUCTION

Appendix GEOCHEM documents the chemistry-related conceptual and process models that are used by Performance Assessment (PA) to calculate mobile actinide (An) releases from the Waste Isolation Pilot Plant (WIPP). The WIPP chemistry-related conceptual models are:

- Gas Generation,
- Chemical Conditions,
- Dissolved Actinide Source Term, and
- Colloidal Actinide Source Term.

Each conceptual model relies on simplifying assumptions and a set of process models. The underlying process models are mathematical descriptions of individual phenomena in the respective conceptual models. For example, the Corrosion of Ferrous Metals process model uses rate equations that predict hydrogen (H_2) production from corrosion and is thus under the umbrella of the Gas Generation Conceptual Model. Table GEOCHEM-1 lists the chemistry-related conceptual models and links them to their associated process models.

Process model input parameters can be fixed or varied to quantify uncertainty. Uncertainty can be associated with the conceptual model, the process model, and/or parameterization of the process models. The uncertainty can be in the model and parameters, or it can be related to the occurrence of future events. Conceptual model uncertainty is addressed through sensitivity analyses, alternative models, or expert judgment documented elsewhere, and scenario uncertainty through defined PA scenarios. Two uncertain parameters for the Corrosion of Ferrous Metals process model are the inundated and humid corrosion rates. To represent uncertainty in experimental corrosion measurements PA samples both corrosion rates with cumulative distribution functions.

Table GEOCHEM-1. Chemistry-related Conceptual and Process Models

Conceptual Model	Process Models (Section)
Gas Generation	Corrosion of Ferrous Metals (Appendix GEOCHEM-2.2.1) Microbial Gas Generation (Appendix GEOCHEM-2.2.2) MgO Hydration and Carbonation (Appendix GEOCHEM-2.2.3) Hydromagnesite to Magnesite Conversion (Appendix GEOCHEM-2.2.4) Radiolysis (Appendix GEOCHEM-2.2.5)
Chemical Conditions	Ionic strength, pH, pcH, pmH, E_h, and Fugacity of CO_2 (Appendix GEOCHEM-3.1.1) Salado and Castile Minerals (Appendix GEOCHEM-3.1.2) Salado and Castile Brines (Appendix GEOCHEM-3.1.3) Magnesium Oxide (Appendix GEOCHEM-3.1.4) Organic Ligands (Appendix GEOCHEM-3.1.5) Borate (Appendix GEOCHEM-3.1.6) Lead (Appendix GEOCHEM-3.1.7) Iron (Appendix GEOCHEM-3.1.8)
Dissolved Actinide Source Term	+III Actinides (Appendix GEOCHEM-4.2.1) +IV Actinides (Appendix GEOCHEM-4.2.2) +V Actinides (Appendix GEOCHEM-4.2.3)
Colloidal Actinide Source Term	Mineral Fragment Colloids (Appendix GEOCHEM-5.2.1) Intrinsic Colloids (Appendix GEOCHEM-5.2.2) Humic Substance Colloids (Appendix GEOCHEM-5.2.3) Microbial Colloids (Appendix GEOCHEM-5.2.4)

GEOCHEM-1.1 WIPP Chemistry and Actinide Release

The actinide (An)-carrying capacity of WIPP brine—both dissolved and colloidal—is used in PA to estimate potential An release from the repository. Determination of this capacity requires information on:

1. The effects of waste materials, packaging materials, and magnesium oxide (MgO) on brine chemistry
2. Actinide solubilities in the resulting brine; and
3. The stability of colloids and their associated An-carrying capacity.

For scenarios involving a direct brine release (DBR) resulting from future drilling, estimates of actinide release additionally require determination of the DBR volume and its corresponding An-carrying capacity.

GEOCHEM-1.1.1 Brine Volumes

The minimum brine volume is used to calculate the initial concentrations of organic ligands in baseline solubility calculations for PA (Domski 2025a). The starting concentrations of acetate, citrate, oxalate, and ethylenediaminetetraacetic acid (EDTA) in EQ3/6 calculations are their respective inventories from the Performance Assessment Inventory Report (PAIR) (Van Soest 2025) divided by the brine volume.

Organic ligand concentrations are calculated for the minimum brine volume as well as 2, 3, 4, and 5 times the minimum brine volume. Baseline An solubilities are then calculated for each brine volume. Simulations are run using the five baseline solubilities to correlate organic ligand concentrations with repository brine volumes.

The minimum brine volume is:

$$(V_{brine})_{Min} = S_{b,med}\ V_{void,consolidated}\ N_{rooms,equivalent} \qquad \text{(GEOCHEM.1)}$$

where:

$(V_{brine})_{Min}$ = minimum brine volume (in the entire repository)
$S_{b,med}$ = median sampled residual brine saturation
$V_{void,consolidated}$ = consolidated void volume of a single room
$N_{rooms,equivalent}$= number of equivalent repository rooms

The minimum brine volume was most recently calculated by Brunell (2025) to be 6,314 cubic meters (m^3), using the methodology of Stein (2005), Clayton (2008), and Docherty (2024). The minimum brine volume used in Compliance Recertification Application – 2019 (CRA-2019) was 17,400 m^3. The new minimum brine volume of Brunell (2025) is the result of reduced disposal room porosities derived from more recent geomechanical modeling (Docherty 2024) applied to the 12-panel interim state repository.

GEOCHEM-1.1.2 Actinide Carrying Capacity

The chemical makeup of repository fluid is qualitatively predicted with reaction between an incoming Salado or Castile brine and the contents of the disposal area. Corrosion of steel (Fe) and lead (Pb) packaging consumes water (H_2O) and produces Fe/Pb-corrosion-products plus H_2. Cellulosic, plastic, and rubber material (CPR) biodegradation will consume sulfate and nitrate and produce hydrogen sulfide (H_2S), nitrogen (N_2) and carbon dioxide (CO_2); and the CO_2 will react with MgO to form hydromagnesite. Organic ligands included in the waste might potentially complex actinides.

The key products of these reactions are dissolved and colloidal An levels, whose concentrations depend on the bulk chemistry of the final DBR brine, particularly hydrogen potential (pH), organic-ligand levels, and colloidal concentrations. The Chemical Conditions

Model constrains the bulk chemistry of brine. The Dissolved Actinide Source Term Model calculates An solubilities in brine. The Colloidal Actinide Source Term Model calculates the concentrations of the colloidal carriers of Ans in brine, and the extent of An partitioning to each. The Gas Generation Model tracks gas accumulation to predict gas transport and repository pressure.

GEOCHEM-1.2 Changes since CRA-2019

Changes to the WIPP PA since CRA-2019 described in Appendix-GEOCHEM include a revised calculation of corroding iron surface area (Appendix GEOCHEM-2.2.1 Process Model for Corrosion of Ferrous Metals), updated analyses feeding the Gas Generation Model (Appendix GEOCHEM-2.5 Summary of Updates since CRA-2019), a new inundated MgO hydration rate (Appendix GEOCHEM-2.3.3 Parameters for MgO Hydration and Carbonation), new chemical reactions and analyses incorporated into the Chemical Conditions Model (Appendix GEOCHEM-3.4 Summary of Updates since CRA-2019), new thermodynamic data and analyses in the Dissolved Actinide Source Term Model (Appendix GEOCHEM-4.5 Summary of Updates since CRA-2019), and new updates to the Colloidal Actinide Source Term Model (Appendix GEOCHEM-5.5 Summary of Updates since CRA-2019).

GEOCHEM-2.0 GAS GENERATION

The Gas Generation Conceptual Model accounts for the major sources and sinks of H_2, H_2S, N_2, and CO_2 in the WIPP disposal area: ferrous metal corrosion, CPR biodegradation, reaction with the MgO engineered barrier, and radiolysis. Brine production and consumption by the same processes are also tracked.

GEOCHEM-2.1 Gas Generation Conceptual Model

The assumptions of the Gas Generation Conceptual Model follow.

GEOCHEM-2.1.1 Homogeneous Gas Generation

Waste, packaging, and MgO in the WIPP will be homogeneously distributed as directed by 40 CFR § 194.24 (d). Inundated and humid gas generation rates are applied homogeneously through the repository. Variability in gas generation depends only on variability in brine saturation.

GEOCHEM-2.1.2 Oxygen Depletion and Temperature

Oxygen will be present while the repository is open but quickly consumed by corrosion of metals and CPR upon closure, making the repository anoxic (U.S. DOE 1996, Appendix PEER 1, Section 3.22.1). The temperature of the disposal area is assumed to be constant with time at WIPP ambient 27 degrees Celsius (°C) (Bennett et al. 1996).

GEOCHEM-2.1.3 Corrosion of Ferrous Metals

Iron corrosion to H_2 will occur under anoxic conditions after closure (U.S. DOE 1996, Appendix PEER 1, Section 3.22.1):

$$Fe(s) + 2H_2O(l) \rightarrow Fe(OH)_2 + H_2(g) \quad \text{(GEOCHEM.3)}$$

$$3Fe(s) + 4H_2O(l) \rightarrow Fe_3O_4(s) + 4H_2(g) \quad \text{(GEOCHEM.4)}$$

Other corrosion products that might form include the iron hydroxychloride, hibbingite, $Fe_2(OH)_3Cl$, and green rust, an Fe-containing layered hydroxide (Nemer et al. 2011; Wang et al. 2001).

GEOCHEM-2.1.4 Corrosion of Non-Ferrous Metals

Gas generation by corrosion of the non-ferrous metals Pb and aluminum (Al) are not included because of their low masses relative to Fe (Kirkes 2019).

GEOCHEM-2.1.5 Microbial Degradation of CPR

Microbes that degrade CPR are assumed to be viable in WIPP brine in PA calculations (Nemer et al. 2005). The CPR will be degraded by denitrifying and sulfate-reducing microbes using respectively nitrate in the waste and sulfate from the Salado and waste. The degradation of CPR will produce N_2 (denitrification), H_2S (sulfate reduction), CO_2 (both), and water (both), recognizing that microbial degradation of CPR, represented simplistically below as $C_6H_{10}O_5(s)$, is a complex process involving a host of interfacial and aqueous phase reactions.

Denitrification

$$C_6H_{10}O_5(s) + 4.8H^+(aq) + 4.8NO_3^-(aq) \rightarrow 7.4H_2O(l) + 6CO_2(g) + 2.4N_2(g) \quad \text{(GEOCHEM.5)}$$

Sulfate-reduction

$$C_6H_{10}O_5(s) + 6H^+(aq) + 3SO_4^{2-}(aq) \rightarrow 5H_2O(l) + 6CO_2(g) + 3H_2S(g) \quad \text{(GEOCHEM.6)}$$

Denitrification will be minor because of low nitrate levels in the waste, the only source of nitrate. Sulfate reduction will dominate as abundant sulfate is available from the Salado (Appendix GEOCHEM-2019, Section GEOCHEM-2.1.5). Much of the produced CO_2 will be consumed by reaction with the MgO engineered barrier and is therefore excluded from the gas accounting for pressure purposes. Conversely, the low level of CO_2 in equilibrium with the MgO engineered barrier is important for chemical reasons and is therefore included in the Chemical Conditions analysis.

GEOCHEM-2.1.6 Steel Passivation

The CO_2 generated by microbial degradation of CPR will not passivate steel because CO_2 will be consumed by the MgO backfill (U.S. DOE 2019, Appendix MgO). The H_2S is assumed to not passivate steel (U.S. EPA 2017, Section 3.2.3).

GEOCHEM-2.1.7 MgO Hydration and Carbonation

The MgO will hydrate to brucite, $Mg(OH)_2(s)$, which will combine with CO_2 from CPR degradation to form hydromagnesite, $Mg_5(CO_3)_4(OH)_2 \bullet 4H_2O(s)$ (Domski 2025a)

MgO Hydration	$MgO(s) + H_2O(aq,g) \rightarrow Mg(OH)_2(s)$	(GEOCHEM.7)
Hydromagnesite Formation	$5Mg(OH)_2(s) + 4CO_2(g) \rightarrow Mg_5(CO_3)_4(OH)_2 \bullet 4H_2O(s)$	(GEOCHEM.8)

GEOCHEM-2.1.8 Hydromagnesite Conversion to Magnesite

Over time hydromagnesite will convert to magnesite, $MgCO_3(s)$, producing brucite and water (Brush and Roselle 2006; Clayton 2013).

Hydromagnesite Conversion	$Mg_5(CO_3)_4(OH)_2 \bullet 4H_2O(s) \rightarrow 4MgCO_3(s) + Mg(OH)_2 + 4H_2O(l)$	(GEOCHEM.9)

The conversion from hydromagnesite to magnesite is sluggish at near-ambient temperatures as suggested by Brush and Roselle (2006) and Gautier et al. (2014). Brush and Roselle (2006) provide arguments based on geochemical calculations and field observations on the occurrence of hydromagnesite and magnesite to indicate the former will be predominant in the early stages of the 10,000-year regulatory period. They also cite the statement from the U.S. EPA (1998) indicating that in the long-term magnesite will replace part or the majority of hydromagnesite throughout the 10,000-year regulatory period.

GEOCHEM-2.1.9 Radiolysis

Alpha radiolysis of brine by dissolved and colloidal radionuclides, and of brine films on wetted solid radionuclides by the underlying radionuclides, will be the most important radiolytic gas generation mechanisms (Day 2019). Radiolysis of CPR will be an insignificant contributor to gas generation. Radiolysis by alpha particles dominates over that of gamma radiation, which is not tracked (Day 2019). Calculated net gas radiolytic production of O_2 is assumed to be zero as a result of reaction with metals in the waste and packaging.

GEOCHEM-2.2 Gas Generation Process Models

The combined rate of gas generation from steel corrosion, microbial degradation of CPR, and radiolysis, q_{rg} (kg/m^3/s), is:

$$q_{rg} = q_{rgc} + q_{rgm} + q_{rgr} \quad \text{(GEOCHEM.10)}$$

where q_{rgc} is the rate of gas production from steel corrosion, q_{rgm} is the gas production rate from microbial degradation of CPR, and q_{rgr} is the gas production rate from radiolysis. PA tracks the amount of gas in the system, but not the composition of the gas. All of the gas in the system is given the fluid flow properties of H_2 (Appendix MASS, Section MASS-2.2).

The water production rate, q_{rb} (kg/m^3/s), is:

$$q_{rb} = q_{rbm} + q_{rbhc} - q_{rbc} - q_{rbh} - q_{rbr} \quad \text{(GEOCHEM.11)}$$

where q_{rbm} is the rate of water production from microbial degradation of CPR, q_{rbhc} is the rate of water production due to hydromagnesite conversion to magnesite, q_{rbc} is the rate of water consumption from steel corrosion, q_{rbh} is the rate of water consumption by hydration of MgO, and q_{rbr} is the rate of radiolytic consumption of water.

$$S_g^* = \begin{cases} 1 - S_{b,eff} & \text{if } S_{b,eff} > 0 \\ 0 & \text{if } S_{b,eff} = 0 \end{cases}$$

GEOCHEM-2.2.1 Process Model for Corrosion of Ferrous Metals

The rate of gas generation from corrosion, q_{rgc}, is:

$$q_{rgc} = \left(R_{ci} S_{b,eff} + R_{ch} S_g^*\right) D_s \rho_{Fe} X_c (H_2|Fe) M_{H_2} \quad \text{(GEOCHEM.12)}$$

where:

R_{ci} = corrosion rate under inundated conditions (m steel/s)

$S_{b,eff}$ = effective brine saturation due to capillary action in the waste materials

where:

$$S_{b,eff} = \mathrm{Max}\left[\mathrm{Min}\left(S_b - S_{min} + S_{wick}\left\{1 - exp\left[\alpha\left(\mathrm{Max}(S_b - S_{min}, 0)\right)^2\right]\right\}, 1\right), 0\right]$$

S_b = brine saturation

S_{wick} = brine saturation due to wicking

S_{min} = lower cut off in saturation

α= numerical smoothing parameter (-1,000).

R_{ch} = corrosion rate under humid conditions (m steel/s)

D_s = initial surface area of steel in the repository (m^2 surface area steel/ m^3 disposal volume)

ρ_{Fe} = molar density of steel (mol/m^3), 1.41 x 10^5 mol/m^3 (Telander and Westerman 1993)

$X_c(H_2|Fe)$ = moles of H_2 produced by the consumption of 1 mole of Fe (mol H_2/mol Fe) = 1

M_{H2} = molecular weight of H_2 (kg H_2/mol H_2).

The terms $S_{b,eff}$ and S_g^*, which are functions of location and time, correct for the amount of substrate exposed to inundated and humid conditions, respectively. Corrosion is assumed to cease when no brine is
present, hence S_g^*= 0 replaces S_g = 1 in the definition of S_g^*.
The rate of brine consumption by corrosion, q_{rbc}, is:

$$q_{rbc} = \frac{q_{rgc} X_c(H_2O|H_2) M_{H_2O}}{M_{H_2}} \qquad \text{(GEOCHEM.13)}$$

where:

$X_c(H_2O|H_2)$ = moles of water (H_2O) consumed per mole of H_2 generated by corrosion (mol H_2O/mol H_2)
M_{H2O} = molecular weight of H_2O (kg H_2O/mol H_2O)

In 2021, a change in the calculation of D_s was written and recommended for implementation into PA (King 2021b).

Previously in CRA-2019, D_s, the surface area of iron per repository volume, was calculated using the old method as the average iron surface area per drum and the optimal loading of drums in the repository:

$$D_s = A_d \frac{n_d}{V_r} \qquad \text{(GEOCHEM.14)}$$

where:

A_d = the surface area of iron per drum
n_d = the number of drums per room assuming optimal loading
V_r = the volume of a room

In this scenario, the reaction rate for gas generation from iron corrosion was unaffected by the amount of iron present in a grid block, and thus the gas generation from iron was independent of the iron inventory. An alternative method for calculation of the iron surface area was developed and recommended for incorporation into WIPP PA (King 2021b). This new approach ties the total iron surface area to the mass of the iron inventory instead of the repository volume and is based on a conversion factor from the mass to the surface area of iron. For this calculation, the surface area estimation technique from (Day 2015) is used with the emplaced

waste in the WIPP repository (the calculation was performed on the inventory as of December 31, 2020) to determine the iron surface area per kg of emplaced waste.

The calculation for D_s has been reformulated to be dependent on the iron inventory and not just repository volume and was recalculated following:

$$D_s = \frac{FESAPKG * WTFETOT}{V_R} \qquad \text{(GEOCHEM.15)}$$

where:

FESAPKG = the Fe surface area per kg Waste (0.105 m^2/kg from King 2021b)

WTFETOT = the total mass of iron in the inventory

V_R = the total volume of the repository

GEOCHEM-2.2.2 Process Model for Microbial Degradation of CPR

The rate of gas production by microbial degradation of CPR is:

$$q_{rgm} = \left(R_{mi} S_{b,eff} + R_{mh} S_g^*\right) D_c X_m(H_2|C) M_{H_2} B_{fc} \qquad \text{(GEOCHEM.16)}$$

where:

R_{mi} = rate of carbon-equivalent cellulosics biodegradation under inundated conditions (mol $C_6H_{10}O_5$/kg $C_6H_{10}O_5$/s)

R_{mh} =rate of carbon-equivalent cellulosics biodegradation under humid conditions (mol $C_6H_{10}O_5$/kg $C_6H_{10}O_5$/s)

D_C = initial mass concentration of cellulosics in the repository (kg carbon equivalent cellulosics /m^3 disposal volume)

$X_m(H_2|C)$ = moles of H_2S and N_2 gas generated per mole of carbon consumed by microbial degradation of cellulose, = $2.4/6\, F_{NO3} + 3/6\, F_{SO4}$ (see Equations (GEOCHEM.5) and (GEOCHEM.6)); where F_{NO3} is the fraction of carbon consumed through denitrification and F_{SO4} is the fraction of carbon consumed by sulfate reduction. F_{NO3} is calculated by comparing the moles of NO_3^- initially present in the repository and the moles of carbon that could be consumed by biodegradation. F_{SO4} is 1 - F_{NO3}. Moles of H_2S and N_2 are summed and treated as H_2 by PA.

B_{fc} = parameter to account for uncertainty in whether microbial gas generation will occur in the WIPP at experimentally measured rates.

The rate of brine production by microbial degradation of CPR is:

$$q_{rgm} = \left(R_{mi} S_{b,eff} + R_{mh} S_g^*\right) D_c X_m(H_2|C) M_{H_2} B_{fc} \qquad \text{(GEOCHEM.17)}$$

where:

$X_m(H_2O|H_2)$ = the moles of H_2O produced per mole of H_2S and N_2 gas generated by microbial degradation of cellulose = $7.4/6\ F_{NO3} + 5/6\ F_{SO4}$ (see Equations (GEOCHEM.5) and (GEOCHEM.6))

Microbial biodegradation is assumed to continue until CPR is exhausted. Biodegradation is assumed to cease if no brine is present. How PA calculates biodegradation of plastic and rubber is described below in Appendix GEOCHEM-2.3.2 Parameters for Microbial Gas Generation.

GEOCHEM-2.2.3 Process Model for MgO Hydration and Carbonation

The rate of brine consumption by MgO hydration is:

$$q_{rbh} = \left(R_{hi}S_{b,eff} + R_{hh}S_g^*\right)D_m X_h(H_2O|MgO)M_{H_2O} \qquad \text{(GEOCHEM.18)}$$

where:

R_{hi} = MgO hydration rate under inundated conditions (mol MgO/kg MgO/s)

R_{hh} = MgO hydration rate under humid conditions (mol MgO/kg MgO/s)

D_m = initial mass concentration of MgO in the repository (kg MgO/m^3 disposal volume) $= 1.2D_c\ M_{MgO}/M_c$, where 1.2 = MgO excess factor (mol MgO/ mole organic carbon); D_c = mass concentration of CPR in the repository (kg biodegradable material/m^3 disposal volume); M_{MgO} = molecular weight of MgO (kg MgO/mol MgO); and M_c = molecular weight of cellulosics (kg cellulosics/mol cellulosics), 2.70 x 10^{-2} kg/mol

$X_h(H_2O|MgO) =$ moles of H_2O consumed by hydration of a mole of MgO = 1

The hydromagnesite production rate due to brucite carbonation, q_{rHMp}, is a function of the rate of CO_2 production from CPR biodegradation:

$$q_{rHMp} = \left(\frac{q_{rgm}}{X_m(H_2|C)M_{H_2}}\right)X_m(CO_2|C)X_{HMprod}(HM|CO_2)M_{brucite} \qquad \text{(GEOCHEM.19)}$$

where:

$X_{HMprod}(HM|CO_2)$ = moles of hydromagnesite produced per mole of CO_2 consumed = 1/4

M_{brucite} = molecular weight of brucite (mol brucite/kg brucite).

The magnesite production rate due to MgO carbonation is:

$$q_{rmp} = (\frac{q_{rgm}}{X_m(H_2|C)M_{H_2}})X_m(CO_2|C)X_{mag_{prod}}(Mag|CO_2)M_{mag} \quad \text{(GEOCHEM.20)}$$

where:

$X_{mag,prod}(Mag|CO_2)$ = moles of magnesite produced per mole of CO_2 consumed = 1

M_{mag} = molecular weight of magnesite (mol magnesite/kg magnesite)

GEOCHEM-2.2.4 Process Model for Hydromagnesite to Magnesite Conversion

The rate of brine production by hydromagnesite conversion to magnesite is:

$$q_{rbhc} = R_{hc}D_{HM}X_{hc}(H_2O|HM)M_{H_2O} \quad \text{(GEOCHEM.21)}$$

where:

R_{hc} = rate of hydromagnesite conversion to magnesite (mol hydromagnesite/kg hydromagnesite/s)

D_{HM} = instantaneous mass concentration of hydromagnesite in the repository (kg hydromagnesite/m^3 disposal volume)

$X_{hc}(H_2O|HM)$ = moles of water produced per mole of hydromagnesite converted to magnesite = 4

The mass concentration of hydromagnesite, mass of hydromagnesite divided by the repository volume, D_{HM}, is calculated dynamically and is a function of the biodegradation rate and the hydromagnesite to magnesite conversion rate.

GEOCHEM-2.2.5 Process Model for Radiolysis

Gas (H_2) generation by radiolysis of brine and wetted solids, q_{rgr} (kg/m^3/s), is calculated as the summed individual reactions decayed as a function of time, $R_{H_2,i}$:

$$q_{rgr} = \frac{M_{H_2}\sum_i R_{H_2,i}}{V_g} \quad \text{(GEOCHEM.22)}$$

$$R_{H_2,i} = (M(t)_{sol,i} + M(t)_{wet,i}\,P_{dep})(\lambda_i\,E_{dis,i}\,G(H_2)_{avg}) \quad \text{(GEOCHEM.23)}$$

where:

V_g = grid volume (m^3)

$M(t)_{sol,i}$ = the time-dependent amount of a given radionuclide in solution (moles); is the product of the volume of waste, porosity, water saturation,

mole fraction of the radionuclide with respect to other radionuclides of the same element, and the sum of the dissolved and colloidal concentrations of the given radionuclide

$M(t)_{wet,i}$ = the time-dependent amount of a given radionuclide on wetted solids (moles); the difference between the total inventory and the inventory in solution multiplied by the brine saturation

P_{dep} = energy deposition probability for wetted solids

λ_i = radionuclide radioactive decay constant (s^{-1})

$E_{dis,i}$ = disintegration energy of radionuclide in electron volts (eV)

$G(H_2)_{avg}$ = average number of H_2 molecules produced per 100 millielectron volts (meV) of absorbed energy (molecule/eV)

Water consumption by radiolysis, q_{rbr} (kg/m^3/s), is: $q_{rbr} = q_{rgr} \frac{M_{H_2O}}{M_{H_2}}$, which converts kg H_2/m^3/s produced to kg H_2O consumed/m^3/s.

GEOCHEM-2.3 Parameterization of the Gas Generation Process Models

GEOCHEM-2.3.1 Parameters for Corrosion of Ferrous Metals

In CRA-2026, both the inundated (R_{ci}) and humid (R_{ch}) corrosion rates are sampled parameters for PA (the range and distribution for these parameters are discussed in Appendix GEOCHEM-2.4.1 Corrosion of Ferrous Metals). The S_{min} is 0.015 (Nemer and Clayton 2008). The wicking saturation, S_{wick}, is treated as an uncertain variable, as in CRA-2019. The corrosion surface area, D_s, is updated in PA to reflect the new calculation based on the total surface area of iron that is tied to the mass of iron in the repository as shown in Equation (GEOCHEM.15).

To conservatively determine the total surface area of iron, both the inner and outer surface areas of the containers are considered by doubling the surface area determined from the bounding external payload container dimensions (dependent on geometry, either cylindrical or prismatic). For overpacked containers, the summation of the surface area of the outer and all overpacked inner payload containers is included. Using these surface area calculations, the iron-based metal waste contents are estimated by two methods: spherical waste or sheet waste. The first method assumes the total surface area of iron per kg based on the number of 1-centimeter (cm) spheres required to achieve the average iron-based metal waste weight, whereas the sheet method determines the total surface area of iron per kg based on the product of the waste weight and the payload container's surface area to tare weight.

The iron surface area per kg of emplaced waste was calculated as 0.094 m^2/kg for the spherical assumption and 0.105 m^2/kg for the sheet waste assumption (when applied to the December 31, 2020 inventory, King 2021b). As the higher iron surface area per kilogram is assumed to be

conservative, the sheet waste assumption calculation is used in WIPP PA and applied in CRA-2026.

GEOCHEM-2.3.2 Parameters for Microbial Gas Generation

The WIPP biodegradable materials are cellulosics, plastics, and rubber materials. Cellulosics are the most biodegradable (Francis et al. 1997). Microbial gas generation in the repository will depend on whether (1) microbes capable of consuming CPR will be present and active, (2) sufficient electron acceptors will be available, and (3) sufficient nutrients will be available.

Inundated and humid CPR degradation rates are described in Appendix GEOCHEM-2.4.2 Microbial Degradation of CPR.

In PA vectors where biodegradation of rubber materials and plastics occur, these materials are converted into an equivalent quantity of cellulosics based on their carbon equivalence (Wang and Brush 1996). Their density is calculated as:

$$D_c = \begin{cases} m_{cel}/V_R \; cellulosics \; only \\ \left(m_{cel} + m_r + 1.7m_p\right)/V_r \; CPR \end{cases} \qquad \text{(GEOCHEM.24)}$$

where V_R is the excavated storage volume of the repository, m_{cel} is the mass of cellulosics (kg), m_r is the mass of rubber materials (kg), and m_p is the mass of plastics (kg) in the waste inventory. The factor 1.7 is the assumed molar-mass ratio of cellulose to plastics (on an equivalent carbon-number basis).

GEOCHEM-2.3.3 Parameters for MgO Hydration and Carbonation

The CRA-2026 uses a maximum inundated MgO hydration rate, R_{hi}, in Generic Weep Brine (GWB) of 2.9×10^{-7} mol/kg/s; a minimum value of 0 mol/kg/s; a mean of 1.4×10^{-7} mol/kg/s; and a truncated normal distribution. The CRA-2026 uses a maximum inundated MgO hydration rate, R_{gi}, in Energy Research and Development Administration (ERDA)-6 brine of 8.8×10^{-8} mol/kg/s; a minimum value of 7.6×10^{-8} mol/kg/s; a mean of 8.2×10^{-8} mol/kg/s; and a truncated normal distribution. Inundated hydration parameter values above have been updated since CRA-2019 based on hydration studies of Martin Marietta MgO (Nemer 2025).

CRA-2026 uses a humid hydration rate, R_{hh}, with a maximum of 2.19×10^{-8} moles/kg/s, a minimum of 1.81×10^{-8} moles/kg/s, and a truncated normal distribution with a mean of 2.00×10^{-8} moles/kg/s (Feng and Kicker 2025).

GEOCHEM-2.3.4 Parameters for Hydromagnesite Conversion to Magnesite

CRA-2026 uses a range of conversion rates between 0 and 3.4×10^{-10} mol/kg/s, and uniform distribution with a mean of 1.7×10^{-10} mol/kg/s (Feng and Kicker 2025) and was discussed in Appendix GEOCHEM-2019 (Section GEOCHEM-2.4.4). This has not changed since CRA-2019.

Note that the baseline actinide solubility model (Appendix GEOCHEM-4.2 Actinide Source Term Process Models) assumes that hydromagnesite forms and persists for the regulatory period, while the gas generation model assumes that hydromagnesite forms and transforms to magnesite, as a function of a sampled conversion rate, during the regulatory period. The assumption that hydromagnesite persists in the actinide solubility model is conservative because the brucite-hydromagnesite buffer maintains a higher f_{CO2} than the brucite-magnesite buffer, which can increase actinide solubility.

GEOCHEM-2.3.5 Parameters for Radiolysis

The process model for H_2 production and water consumption by brine radiolysis requires values for: P_{dep}, λ_i, $E_{dis,i}$, and $G(H_2)_{avg}$. The energy deposition probability P_{dep} is a sampled parameter between 0 and 0.5 (discussed in Appendix GEOCHEM-2.4.5 Radiolysis). Decay constants λ_i are previously established PA analysis parameters. Total Emitted Energy from Annex A. Radionuclides of the ICRP-07 Collection (ICRP 2008) are conservatively used for radionuclide disintegration energies $E_{dis,i}$. The average G-value for H_2 $G(H_2)_{avg}$ comes from the WIPP-relevant brine radiolysis experimental measurements of Reed et al. (1993).

GEOCHEM-2.4 Gas Generation Uncertainty Quantification

Uncertainties in gas generation include: the identity of the corrosion product(s); the relative proportions of CPR material consumed by microbes; unit gas production rates for corrosion and degradation; the probability for wetted solid radionuclides to contribute to radiolytic gas generation; and unit brine consumption/production rates for MgO hydration and hydromagnesite conversion to magnesite.

GEOCHEM-2.4.1 Corrosion of Ferrous Metals

The corrosion parameters of interest for ferrous metals are R_{ci}, the corrosion rate under inundated conditions in meters per second (m/s), and R_{ch}, the corrosion rate under humid conditions in m/s. In CRA-2019, a cumulative distribution function (CDF) was developed to represent the R_{ci} based on equally weighting (giving all inputs the same probability of occurrence) all non-negative corrosion rates reported by Roselle (2013) (Zeitler and Hansen 2015a). This distribution was adjusted by a factor of two to account for the potential of enhanced corrosion rates at the elevated repository pressure (U.S. EPA 2017). For R_{ch}, a CDF was developed for 5 parts per million (ppm) CO_2 (selected as it was an order of magnitude greater than the expected CO_2 fugacity in the repository and thus bounding) by linearly interpolating from the 0 and 350 ppm CO_2 humid corrosion rates in Roselle (2013) (Zeitler and Hansen 2015b). The CDF for R_{ci} and R_{ch} are similarly applied in CRA-2026. No changes were made from the CRA-2019 to the CRA-2026.

GEOCHEM-2.4.2 Microbial Degradation of CPR

In CRA-2026 PA samples four CPR degradation parameters (Appendix GEOCHEM-2019, Section GEOCHEM-2.4.2):

1. R_{mi}, the rate of cellulose biodegradation under inundated conditions (mol $C_6H_{10}O_5$/kg $C_6H_{10}O_5$/s); its values range uniformly between 3.08×10^{-11} and 5.57×10^{-10} moles organic carbon consumed per kg cellulose per second.
2. R_{mh}, the rate of cellulose biodegradation under humid conditions (mol $C_6H_{10}O_5$/kg $C_6H_{10}O_5$/s); its values range uniformly between 0 and 1.03×10^{-9} moles organic carbon consumed per kg cellulose per second. Subsequent to sampling, a conditional relationship is applied between the humid and inundated rates, such that the inundated rate always exceeds the humid rate (King and Zeitler 2025; Section 4.3.1).
3. B_{fc} is the uncertainty factor defining the probability that microbial activity will occur at experimentally observed rates. B_{fc} is uniformly sampled from 0 to 1.
4. Parameter PROBDEG accounts for the probability of plastic and rubber degradation, in addition to cellulose degradation. PROBDEG is sampled by PA with a delta distribution; the D_C term in Equation (GEOCHEM.17) is changed accordingly as seen in Equation (GEOCHEM.24). There is a 25% chance of realizing plastic and rubber degradation.

PA performs conditional sampling of R_{mi} and R_{mh} (King and Zeitler 2025; Equation 1).

Sampling of B_{fc} accounts for uncertainty in (Brush 2005) whether microbes will survive for a significant fraction of the 10,000-year regulatory period,

Appendix SOTERM, Section SOTERM-4.1 discusses work at Los Alamos National Laboratory (LANL) to determine if microbes will be active under WIPP conditions.

GEOCHEM-2.4.3 MgO Hydration Rate

Although Kirchner (2013) showed that computed radionuclide releases are not sensitive to MgO hydration rates, the range of humid and inundated hydration rates are sampled by PA for CRA-2026 (Appendix GEOCHEM-2.3.3 Parameters for MgO Hydration and Carbonation).

GEOCHEM-2.4.4 Hydromagnesite Conversion Rate

For CRA-2026, uncertainty in the hydromagnesite to magnesite conversion rate is accounted for by PA sampling the range of assumed rates (Appendix GEOCHEM-2.3.4 Parameters for Hydromagnesite Conversion to Magnesite).

GEOCHEM-2.4.5 Radiolysis

The key uncertainty in the radiolysis calculation is the probability for wetted solid radionuclides to contribute to radiolytic gas generation. This uncertainty is accounted for in PA by uniformly sampling P_{dep}, the energy deposition probability, between 0 and 0.5 (Day 2019). The upper bound of 50 percent (%) energy deposition is consistent with the particle size distribution average of multiple representative plutonium processes utilized in the DOE complex (Narlesky et al. 2012). The lower bound of 0 % energy deposition represents the limiting case in which alpha energy from wetted solid radionuclides is fully attenuated before reaching brine, through particle self-attenuation and absorption in adjacent non-brine

materials. Day (2019) specifically identifies non-hydrogenous materials for this lower-bound example; hydrogenous materials such as paper or other CPR can also attenuate alpha particles, but energy absorbed in CPR may contribute to CPR radiolysis rather than being gas-inert.

Subsequent analyses of radiolytic gas production uncertainty indicate that: 1. Radiolytically generated gas from a single panel containing a disproportionate amount of surplus plutonium and pit production waste would not significantly affect WIPP performance (King et al. 2023b); 2. Gas generation by radiolysis of water adsorbed on non-brine inundated solid radionuclides will be relatively minor compared to that of brine (King et al. 2023b) and that: 3. Gas generation by radiolysis of CPR should continue to be screened out because of minimal impact (King et al. 2023b). King et al. (2023a) showed that, while gas generation by radiolysis of adsorbed water slightly increases repository pressures, it also decreases brine saturation, leading to slightly lower repository releases.

GEOCHEM-2.5 Summary of Updates since CRA-2019

Additions to the Gas Generation Model since CRA-2019 are a new method for calculating Fe surface area (Appendix GEOCHEM-2.2.1 Process Model for Corrosion of Ferrous Metals), and a new saturated MgO hydration rate (GEOCHEM-2.3.3 Parameters for MgO Hydration and Carbonation).

GEOCHEM-3.0 CHEMICAL CONDITIONS

To predict repository chemical conditions equilibrium is assumed between brine, the Salado Formation primary minerals, Fe and Pb corrosion products, MgO, and organic ligands in the waste.

In the Chemical Conditions Conceptual Model:

> *Brine and waste are modeled as a uniform mix of dissolved and solid phases. Thermodynamic equilibrium is assumed for dissolved actinides but not for redox reactions amongst the actinides. Further, chemical homogeneity and solubility equilibrium are assumed. This allows for the assumption of instantaneous reactions. Chemical microenvironments are not believed to persist for this reason. DOE assumes there will not be conditions whereby supersaturation can exist for long periods of time. Temperatures will increase a total of approximately 5.4°C (radioactive decay and exothermic reactions), and it is assumed that there will be negligible effects due to this increase* (U.S. DOE 1996, Appendix PEER 1, Section 3.22.1).

The repository is assumed to be reducing and at, or near, a temperature of 27 ^{o}C. The pH of the repository is assumed to be largely controlled by reactions between CO_2, H_2O, and MgO.

Brine that reacts with the waste under any intrusion scenario will have a composition of Salado or Castile brine. In the undisturbed scenario, Salado brine is used. Culebra groundwater that

might enter the repository will quickly dissolve halite and develop a composition like Salado brine. Because the Salado and Castile brines bracket the possible brine compositions, experiments and modeling performed with Salado and Castile compositions are adequate for describing the repository geochemistry (U.S. DOE 2014, Appendix SOTERM-2014, Section SOTERM-2.3.1). These assumptions were deemed adequate in the original WIPP peer review (U.S. DOE 1996, Appendix PEER).

The density and total dissolved solids (TDS) values of the unreacted GWB and ERDA-6 brines are used to calculate the solids scaling factor for each brine volume: Solid Scaling Factor = $1/([r_{brine} – TDS] \times V_{DBR})$; where r_{brine} = brine density (kg/m^3), TDS = brine total dissolved solids (kg/m^3), and V_{DBR} = brine volume (m^3) during a DBR event. The GWB formulation is used to simulate Salado brine, and ERDA-6 brine is used to simulate Castile brine (Table GEOCHEM-2). The GWB and ERDA-6 compositions are used in PA simulations.

Table GEOCHEM-2. Composition of GWB and ERDA-6 Brine before Reaction with Anhydrite, Brucite and Hydromagnesite.

Ion or property[1]	GWB Brine Composition[2]	ERDA-6 Brine Composition[3]
$B(OH)_3$	158 mM	63 mM
Na^+	3.53 M	4.87 M
Mg^{2+}	1.02 M	19 mM
K^+	0.467 M	97 mM
Ca^{2+}	14 mM	12 mM
SO_4^{2-}	177 mM	170 mM
Cl^-	5.86 M	4.8 M
Br^-	26.6 mM	11 mM
Total Inorganic C (as HCO_3^-)	16 mM[4]	16 mM
pH	7.0[5]	6.17
Ionic Strength (M)	7.44	5.32

[1]Ions listed represent the total of all species containing the ion. [2]From Snider 2003. [3]From Popielak et al. 1983. [4]The total inorganic carbon value for ERDA-6 is used for GWB because it was not reported for the latter. [5]GWB pH is set to 7 because it was not reported.

In most PA realizations, significant uncorroded ferrous metal is predicted to be present throughout the 10,000-year regulatory period. Fe and Pb corrosion products will limit dissolved Fe and Pb levels. Organic ligands from the waste will dissolve into solution. The MgO engineered barrier will hydrate, then react with CO_2 from CPR biodegradation to form hydromagnesite, buffering pH to 8.7 - 9.0. Radiolysis can lead to locally oxidizing conditions but will not change the overall reducing environment (Appendix SOTERM, Section SOTERM 3.4).

GEOCHEM-3.1 Representation of WIPP Chemical Conditions

An equilibrium chemical model implemented in EQ3/6 version 8.0a (Wolery and Jarek 2003; Wolery et al. 2010) simulates the interaction of WIPP brines (GWB and ERDA-6) with Salado mineralogy, MgO engineered barrier, waste package materials, and waste components.

The chemical equilibrium model combines parts of the chemical conditions and the dissolved actinide source term process model in a single computational model to provide the near-field

chemical conditions and the total dissolved actinide (+III, +IV, and +V) solubility values for WIPP PA calculations. This combined chemical-equilibrium model is known as the "baseline solubility model" (Appendix GEOCHEM-4.1.2 Use of the Pitzer Model). The CRA-2026 baseline solubility model differs from the 2019 Compliance Recertification Application Deferred Performance Assessment (CRA-2019 DPA) baseline solubility model (Domski 2019) in four ways:

- The updated WIPP thermodynamic database DATA0.FM6 (Domski 2023a; also see U.S. DOE 2024a; U.S. DOE 2024b) is used rather than DATA0.FM4. The updates and additions since DATA0.FM4 towards DATA0.FM6 include: Pitzer parameter evaluations to the Pb-Cl-Na-Mg-SO_4-CO_3 system, calcium citrate solid phase earlandite, Fe-SO_4 and Fe-organic complexes, Nd(III) hydroxide amorphous solid to represent $Am(OH)_3$(am), and Mg-oxalate system including the Mg-oxalate solid phase glushinskite.
- The CRA-2026 is based on a new 12-panel repository geometry, which decreased the minimum brine volume required for a direct brine release (Brunell 2025) which in turn affects the organic ligand concentrations, as well as the scaling of the reactants, used in the solubility model.
- A new inventory is used for the CRA-2026 (Van Soest 2025) which provides updated inventories used in the solubility model,
- Model assumptions are updated with regard to calcite precipitation, phase 5 ($Mg_3Cl(OH)_5$•$4H_2O$) precipitation, and scaling of the reactants.

The Chemical Conditions Process Models collect the information needed to constrain the bulk composition of a repository fluid which controls brine actinide (ion) solubilities. Data needed are the individual chemical reactions involved and their equilibrium constants. The Dissolved Actinide Source Term Model (Appendix GEOCHEM-4.0 Dissolved Actinide Source Term) uses this information to calculate the dissolved solubility of an actinide (in a specific oxidation state). Actinide speciation, solubility reactions, and Pitzer interactions are described in Appendix GEOCHEM-4.0 Dissolved Actinide Source Term; non-actinide reactions and interactions are the focus here. The following sections describe specific features of the WIPP Chemical Conditions Process Model.

GEOCHEM-3.1.1 Ionic Strength, Brine pH, pcH, pmH, E_h, and Fugacity of CO_2

Brine ionic strength, pH, E_h, and CO_2 fugacity control actinide solubility and, with the exception of E_h, are calculated parameters. Sometimes, pcH and pmH are used to quantify brine acidity instead of pH.

The ionic strength of a solution is:

$$I = \frac{1}{2}\sum m_s z_s^2 \qquad \text{(GEOCHEM.25)}$$

where m_s and z_s are the molality and valence charge, respectively, of each solute species,

pH is the negative common logarithm of aqueous hydrogen ion activity in a solution, -log a_{H+}. In brines, pcH (pC_{H+}), the negative common logarithm of the molar concentration of hydrogen ions, or pmH (pm_{H+}), the negative common logarithm of the molal concentration of hydrogen ions, are used. pH and pcH (or pmH) are typically related through empirical correlations.

The WIPP Chemical Conditions Process Model does not include individual oxidation/reduction reactions, though reducing conditions are assumed over the 10,000-year regulatory period because of Fe corrosion to ferrous iron and H_2.

Magnesium oxide is emplaced as an engineered barrier and acts as a pH buffer to offset the effect of pH-lowering carbon dioxide produced by microbial activity in the post-closure repository. In the absence of MgO, high CO_2 fugacity could occur, lowering pH in the repository brine. To mitigate this possibility, MgO will hydrate to form brucite, $Mg(OH)_2$, which will in turn react with CO_2 to form hydromagnesite (which might convert to magnesite) and buffer pH.

GEOCHEM-3.1.2 Salado and Castile Minerals

Minerals that might be present and in contact with WIPP repository waste were characterized prior to initial certification (Powers et al. 1978).

The Salado and Castile minerals in DATA0.FM6 (Domski 2023a) for CRA-2026 are: Sodium-bearing minerals: halite (NaCl), nahcolite ($NaHCO_3$), trona ($Na_3H[CO_3]_2•2H_2O$), natron ($Na_2CO_3•10H_2O$), $Na_2CO_3•7H_2O$(s), thermonatrite ($Na_2CO_3•H_2O$), pirssonite ($Na_2Ca[CO_3]_2•2H_2O$), burkeite ($Na_6CO_3[SO_4]_2$), mirabilite ($Na_2SO_4•10H_2O$), thenardite (Na_2SO_4), $Na_3H(SO_4)_2$(s), aphthitalite ($NaK_3[SO_4]_2$), glauberite ($Na_2Ca[SO_4]_2$), bloedite ($Na_2Mg[SO_4]_2•4H_2O$), gaylussite ($CaNa_2[CO_3]_2•5H_2O$), $KNaCO_3•6H_2O$, K-trona($K_2NaH[CO_3]_2•2H_2O$), and labile salt ($Na_4Ca[SO_4]_3•2H_2O$); Potassium-bearing minerals: mercallite ($KHSO_4$), sylvite (KCl), misenite ($K_8H_6[SO_4]_7$), arcanite (K_2SO_4), syngenite ($K_2Ca[SO_4]_2•H_2O$), kalicinite ($KHCO_3$), $K_2CO_3•1.5H_2O$(s), $K_8H_4(CO_3)_6•3H_2O$(s), $KNaCO_3•6H_2O$(s), carnallite ($KMgCl_3•6H_2O$), kainite ($KMgClSO_4•3H_2O$), picromerite ($K_2Mg[SO_4]_2•6H_2O$), leonite ($K_2Mg[SO_4]_2•4H_2O$), polyhalite ($K_2MgCa_2[SO_4]_4•2H_2O$), $K_3H(SO_4)_2$, aphthitalite/glaserite ($NaK_3[SO_4]_2$), and K-trona ($K_2NaH[CO_3]_2•2H_2O$); and Calcium-bearing minerals: $CaCl_2•4H_2O$(s), $Ca_4Cl_2(OH)_6•13H_2O$(s), $Ca_2Cl_2(OH)_2•H_2O$(s), aragonite ($CaCO_3$), portlandite ($Ca[OH]_2$), calcite ($CaCO_3$), gaylussite ($CaNa_2[CO_3]_2•5H_2O$), anhydrite ($CaSO_4$), dolomite ($CaMg[CO_3]_2$), gypsum ($CaSO_4•2H_2O$), tachyhydrite ($Mg_2CaCl_6•12H_2O$), pirssonite ($Na_2Ca[CO_3]_2•2H_2O$), glauberite ($Na_2Ca[SO_4]_2$), labile salt ($Na_4Ca[SO_4]_3•2H_2O$), syngenite ($K_2Ca[SO_4]_2•H_2O$), and polyhalite ($K_2MgCa_2[SO_4]_4•2H_2O$).

GEOCHEM-3.1.3 Salado and Castile Brines

The major elements in the Salado and Castile brines are sodium, magnesium, potassium, chloride, carbonate, sulfate, and borate (Table GEOCHEM-3). Chemical reactions involving sulfide produced by microbial activity are not included in CRA-2026.

GEOCHEM-3.1.4 Magnesium Oxide

The MgO engineered barrier limits CO_2 levels by CO_2 reaction with magnesium solids. The Magnesium solids in DATA0.FM6 (Domski 2023a) for CRA-2026 are: brucite ($Mg[OH]_2$), bischofite ($MgCl_2•6H_2O$), phase 3 ($Mg_2Cl[OH]_3•4H_2O$), tachyhydrite ($Mg_2CaCl_6•12H_2O$), carnallite ($KMgCl_3•6H_2O$), dolomite ($CaMg[CO_3]_2$), magnesite ($MgCO_3$), nesquehonite ($MgCO_3•3H_2O$), hydromagnesite4323 ($Mg_4[CO_3]_3[OH]_2•3H_2O$), hydromagnesite-5424 ($Mg_5[CO_3]_4[OH]_2•4H_2O$) (U.S. DOE 2024a), leonite ($K_2Mg[SO4]_2•4H_2O$), bloedite ($Na_2Mg[SO_4]_2•4H_2O$), epsomite ($MgSO_4•7H_2O$), hexahydrite ($MgSO_4•6H_2O$), kieserite ($MgSO_4•H_2O$), picromerite ($K_2Mg[SO_4]_2•6H_2O$), polyhalite ($K_2MgCa_2[SO_4]_4•2H_2O$), and kainite ($KMgClSO_4•3H_2O$). Note that Phase 5 ($Mg_3Cl[OH]_5•4H_2O$) is suppressed in actinide solubility calculations based on the analysis of Domski and Nemer (2023a) pointing to uncertainty in the solubility of Phase 5 relative to that of Phase 3. Other mineral phases suppressed for CRA-2025 solubility calculations are: calcite, dolomite, magnesite, nesquehonite, and $Am(OH_3)$ (Domski 2025a). It should be noted that although picromerite and polyhalite were not part of the MgO solid list in section GEOCHEM-3.2.4 of CRA-2019, these were present in DATA0.FM4.

GEOCHEM-3.1.5 Organic Ligands

Organic ligand solids in DATA0.FM6 (Domski 2023a) for CRA-2026 are: NaHOxalate•H_2O(s), Na_2Oxalate(s), whewellite (CaOxalate•$2H_2O$), and H_2Oxalate•$2H_2O$(s), earlandite ($Ca_3Citrate_2•4H_2O$), and glushinskite (MgOxalate•$2H_2O$). Organic ligand aqueous species considered for CRA-2026 are: HAcetate, $MgAcetate^+$, $CaAcetate^+$, H_3Citrate (aq), $H_2Citrate^-$, $HCitrate^{2-}$, $MgCitrate^-$, $CaCitrate^-$, FeCitrate-, $FeOHCitrate^{2-}$, H_4EDTA(aq), H_3EDTA^-, H_2EDTA^{2-}, $HEDTA^{3-}$, $FeEDTA^{2-}$, $MgEDTA^{2-}$, $CaEDTA^{2-}$, H_2Oxalate(aq), $HOxalate^-$, MgOxalate(aq), $Mg(Oxalate)_2^{2-}$, CaOxalate(aq), HLactate(aq). These solids and aqueous species were included in the CRA-2019.

GEOCHEM-3.1.6 Borate

Borate minerals in DATA0.FM6 (Domski 2023a) for CRA-2026 include: borax ($Na_2B_4O_7•10H_2O$), boric acid ($B[OH]_3$), K-pentaborate ($KB_5O_8•4H_2O$), K-tetraborate ($K_2B_4O_7•4H_2O$), Na-metaborate ($NaBO_2•4H_2O$), Na-pentaborate ($NaB_5O_8•5H_2O$), and teepleite ($NaBO_2•NaCl•2H_2O$); along with the aqueous species $B(OH)_4^-$, $B(OH)_3$(aq), $CaB(OH)_4^+$, $MgB(OH)_4^+$, $B_3O_3(OH)_4^-$, and $B_4O_5(OH)_4^{2-}$. These solids and aqueous species were included in the CRA-2019.

GEOCHEM-3.1.7 Lead

Lead is present in waste and in shielded containers. Lead minerals in DATA0.FM6 (Domski 2023a) for CRA-2026 are: cotunnite ($PbCl_2$) (U.S. DOE 2025), cerussite ($PbCO_3$) (U.S. DOE 2024b), abellaite ($NaPb_2[CO_3]_2[OH]$), hydrocerussite ($2Pb[CO_3]_2•Pb[OH]_2$) (U.S. DOE 2025), and anglesite ($PbSO_4$); along with the aqueous species Pb^{2+}, $PbCl^+$, $PbCl_2$(aq), $PbCl_3^-$, $PbHCO_3^+$, $PbCO_3$(aq), $Pb(CO_3)_2^{2-}$, $Pb(CO_3)_3^{4-}$, and $Pb(CO_3)(OH)^-$. These Pb solids were included in the CRA-2019, except for cotunnite, abellaite, and hydrocerussite. Note that the PbO (litharge) solid in

CRA-2019 is not included in DATA0.FM6 for CRA-2026. Similarly, these Pb aqueous species were also included in CRA-2019, except for $PbHCO_3^+$ and $Pb(CO_3)_3^{4-}$. Note that the aqueous species $PbOH^+$, $Pb(OH)_2(aq)$, $Pb(CO_3)Cl^-$, and $Pb(SO_4)(aq)$ in CRA-2019 are not in DATA0.FM6 for CRA-2026.

GEOCHEM-3.1.8 Iron

Iron is present in the waste and as packaging. Fe minerals included in DATA0.FM6 (Domski 2023a) for CRA-2026 are: ferrous iron hydroxide ($Fe[OH]_2$), hibbingite ($Fe_2Cl[OH]_3$), siderite ($FeCO_3$), chukanovite ($Fe_2CO_3[OH]_2$), szomolnokite ($FeSO_4•H_2O$), and melanterite ($FeSO_4•7H_2O$), along with the aqueous species; $FeOH^+$, $Fe(OH)_2(aq)$, $Fe(OH)_3^-$, $Fe(OH)_4^{2-}$, $FeCO_3(aq)$, $Fe(CO_3)_2^{2-}$, $FeCitrate^-$, and $FeOHCitrate^{2-}$. The formation of $FeEDTA^{2-}$ is suppressed in actinide solubility calculations.

GEOCHEM-3.2 Parameterization of the Chemical Conditions Process Model

GEOCHEM-3.2.1 Salado and Castile Mineral Parameters

Salado and Castile mineral reactions in DATA0.FM6 (Domski 2023a) for CRA-2026, Table GEOCHEM-3, have not changed since CRA-2019.

Table GEOCHEM-3. Salado and Castile Mineral Dissolution Reactions for CRA-2026

Dissolution Reaction
$NaCl(halite) \leftrightarrow Na^+ + Cl^-$
$NaHCO_3(nahcolite) \leftrightarrow Na^+ + HCO_3^-$
$Na_3H(CO_3)_2•2H_2O(trona) + H^+ \leftrightarrow 3Na^+ + 2HCO_3^- + 2H_2O$
$Na_2CO_3•10H_2O(natron) + H^+ \leftrightarrow 2Na^+ + HCO_3^- + 10H_2O$
$Na_2CO_3•7H_2O(s) + H^+ \leftrightarrow 2Na^+ + HCO_3^- + 7H_2O$
$Na_2CO_3•H_2O(thermonatrite) + H^+ \leftrightarrow 2Na^+ + HCO_3^- + H_2O$
$Na_6CO_3(SO_4)_2(s)\ (Burkeite) + H^+ = 6Na^+ + HCO_3^- + 2SO_4^{2-}$
$Na_2Ca(CO_3)_2•2H_2O(pirssonite) + 2H^+ \leftrightarrow 2Na^+ + Ca^{2+} + 2HCO_3^- + 2H_2O$
$Na_2SO_4•10H_2O(mirabilite) \leftrightarrow 2Na^+ + SO_4^{2-} + 10H_2O$
$Na_2SO_4(thenardite) \leftrightarrow 2Na^+ + SO_4^{2-}$
$Na_3H(SO_4)_2(s) \leftrightarrow 3Na^+ + H^+ + 2SO_4^{2-}$
$NaK_3(SO_4)_2(aphthitalite, glaserite) \leftrightarrow Na^+ + 3K^+ + 2SO_4^{2-}$
$Na_2Ca(SO_4)_2(glauberite) \leftrightarrow 2Na^+ + Ca^{2+} + 2SO_4^{2-}$
$Na_4Ca(SO_4)_3•2H_2O(labile\ salt) \leftrightarrow 4Na^+ + Ca^{2+} + 3SO_4^{2-} + 2H_2O$
$KHSO_4(mercallite) \leftrightarrow K^+ + SO_4^{2-} + H^+$

Dissolution Reaction
KCl (sylvite) ↔ $K^+ + Cl^-$
$K_8H_6(SO_4)_7$(misenite) ↔ $8K^+ + 6H^+ + 7SO_4^{2-}$
$K_3H(SO_4)_2$(s) = $3K^+ + H^+ + 2SO_4^{2-}$
K_2SO_4(arcanite) ↔ $2K^+ + SO_4^{2-}$
$K_2Ca(SO_4)_2•H_2O$(syngenite) ↔ $2K^+ + Ca^{2+} + 2SO_4^{2-} + H_2O$
$KHCO_3$(kalicinite) ↔ $K^+ + HCO_3^-$
$K_2CO_3•1.5H_2O$(s) + H^+ ↔ $2K^+ + HCO_3^- + 1.5H_2O$
$K_8H_4(CO_3)_6•3H_2O$(s) + $2H^+$ ↔ $8K^+ + 6HCO_3^- + 3H_2O$
$KNaCO_3•6H_2O$(s) + H^+ ↔ $K^+ + Na^+ + HCO_3^- + 6H_2O$
$K_2NaH(CO_3)_2•2H_2O$(K-trona) + H^+ ↔ $2K^+ + Na^+ + 2HCO_3^- + 2H_2O$
$CaCl_2•4H_2O$(s) ↔ $Ca^{2+} + 2Cl^- + 4H_2O$
$CaCl_2.6H_2O$(s) (Antarcticite) = $Ca^{+2} + 2Cl^- + 6H_2O$
$Ca_4Cl_2(OH)_6•13H_2O$(s) + $6H^+$ ↔ $4Ca^{2+} + 2Cl^- + 19H_2O$
$Ca_2Cl_2(OH)_2•H_2O$(s) + $2H^+$ ↔ $2Ca^{2+} + 2Cl^- + 3H_2O$
$CaCO_3$(aragonite) + H^+ ↔ $Ca^{2+} + HCO_3^-$
$CaCO_3$(calcite) + H^+ ↔ $Ca^{2+} + HCO_3^-$
$CaNa_2(CO_3)_2•5H_2O$(gaylussite) + $2H^+$ ↔ $Ca^{2+} + 2Na^+ + 2HCO_3^- + 5H_2O$
$Ca(OH)_2$(portlandite) + $2H^+$ ↔ $Ca^{2+} + 2H_2O$
$CaSO_4$(anhydrite) ↔ $Ca^{2+} + SO_4^{2-}$
$CaSO_4•2H_2O$(gypsum) ↔ $Ca^{2+} + SO_4^{2-} + 2H_2O$

GEOCHEM-3.2.2 Salado and Castile Brine Parameters

Dissociation reactions for Salado and Castile brines for CRA-2026, Table GEOCHEM-4, have not changed since CRA-2019. Pitzer interactions are shown in Table GEOCHEM-5 and Table GEOCHEM-6. They have not changed since CRA-2019.

Table GEOCHEM-4. Salado and Castile Brine Dissociation Reactions for CRA-2026

Dissociation Reaction
H_2O ↔ $OH^- + H^+$
HSO_4^- + H^+↔ SO_4^{2-} + H^+
CO_3^{2-} + H^+ ↔ HCO_3^-

Dissociation Reaction
$CO_2(aq) + H_2O = H^+ + HCO_3^-$
$CaCO_3(aq) + H^+ \leftrightarrow Ca^{2+} + HCO_3^-$
$MgOH^+ + H^+ \leftrightarrow Mg^{2+} + H_2O$
$MgCO_3(aq) + H^+ \leftrightarrow Mg^{2+} + HCO_3^-$

Table GEOCHEM-5. Pitzer Interactions for Salado and Castile Brines for CRA-2026

Cation-Anion	**H^+**	**Na^+**	**K^+**	**Ca^{2+}**	**Mg^{2+}**	**$MgOH^+$**			
OH^-		x	x	x					
ClO_4^-	x	x		x	x				
Cl^-	x	x	x	x	x	x			
HCO_3^-		x	x	x	x				
HSO_4^-	x	x	x	x	x				
SO_4^{2-}	x	x	x	x	x				
CO_3^{2-}		x	x						
$H_2PO_4^-$		x	x						
HPO_4^{2-}		x	x						
PO_4^{3-}		x	x						
Cation-Cation	**H^+**	**Na^+**	**Mg^{2+}**	**K+**	**Ca^{2+}**				
H^+		x	x	x	x				
Na^+			x	x	x				
Mg^{2+}					x				
K^+					x				
Ca^{2+}									
Anion-Anion	**OH^-**	**ClO_4^-**	**Cl^-**	**HCO_3^-**	**HSO_4^-**	**SO_4^{2-}**	**CO_3^{2-}**	**$H_2PO_4^-$**	
OH^-									
ClO_4^-	x								
Cl^-	x								
HCO_3^-		x	x						
HSO_4^-			x						
SO_4^{2-}	x		x	x					
CO_3^{2-}	x	x	x	x		x			
$H_2PO_4^-$			x						
Neutral-Cation	**Na^+**	**K^+**	**Ca^{2+}**	**Mg^{2+}**	**H^+**				
CO_2(aq)	x	x	x	x	x				
O_2(aq)	x	x	x	x	x				
H_3PO_4(aq)		x			x				
Neutral-Anion	**Cl^-**	**HSO_4^-**	**SO_4^{2-}**	**OH^-**	**$HCO3^-$**	**CO_3^{2-}**	**Br-**	**NO_3^-**	**$H_2PO_4^-$**
CO_2(aq)	x	x	x						
O_2(aq)	x		x	x	x	x	x	x	
H_3PO_4(aq)	x								x

x: Used. Single strikethrough down: Not used. Single strikethrough up: Diagonal reflection of other half.

Table GEOCHEM-6. Pitzer Interactions for Salado and Castile Brines for CRA-2026 Continued

Cation-Cation-Anion	Cl^-	HCO_3^-	HSO_4^-	SO_4^{2-}	CO_3^{2-}	ClO_4^-
Na^+, K^+	x	x		x	x	
Na^+, Ca^{2+}	x			x		
Na^+, Mg^{2+}	x			x		
Na^+, H^+	x		x			x
K^+, Ca^{2+}	x					
K^+, Mg^{2+}	x			x		
K^+, H^+	x		x	x		
Ca^{2+}, Mg^{2+}	x			x		
Ca^{2+}, H^+	x					
Mg^{2+}, $MgOH^+$	x					
Mg^{2+}, H^+	x		x			
Anion-Anion-Cation	**H^+**	**Na^+**	**K^+**	**Ca^{2+}**	**Mg^{2+}**	
Cl^-, SO_4^{2-}		x		x	x	
Cl^-, HSO_4^-	x	x				
Cl^-, OH^-		x	x	x		
Cl^-, HCO_3^-		x			x	
Cl^-, CO_3^{2-}		x	x			
Cl-, $H_2PO_4^-$			x			
ClO_4^-, HCO_3^-		x				
ClO_4^-, CO_3^{2-}		x				
SO_4^{2-}, HSO_4^-		x	x		x	
SO_4^{2-}, OH^-		x	x			
SO_4^{2-}, HCO_3^-		x			x	
SO_4^{2-}, CO_3^{2-}		x	x			
OH^-, CO_3^{2-}		x	x			
HCO_3^-, CO_3^{2-}		x	x			
Neutral-Anion-Cation	**H^+**	**Na^+**	**K^+**	**Ca^{2+}**		
$O_2(aq)$, OH^-		x	x			
$O_2(aq)$, Cl^-	x	x	x	x		
$O_2(aq)$, HCO_3^-		x				
$O_2(aq)$, SO_4^{2-}		x	x			
$O_2(aq)$, CO_3^{2-}		x				
$O_2(aq)$, NO_3^-		x	x	x		
$O_2(aq)$, Br-		x	x			

x: Used. Single strikethrough: Not used.

GEOCHEM-3.2.3 Magnesium Oxide Parameters

Reactions for MgO solids in DATA0.FM6 (Domski 2023a) for CRA-2026, Table GEOCHEM-7, have not changed since CRA-2019. Again, Phase 5 is suppressed in actinide solubility calculations based on the analysis of Domski and Nemer (2023a).

Table GEOCHEM-7. MgO Solid Dissolution Reactions for CRA-2026

MgO Solid Dissolution Reactions
$Mg(OH)_2$(brucite) + $2H^+ \leftrightarrow Mg^{2+} + 2H_2O$
$MgCl_2 \bullet 6H_2O$(bischofite) $\leftrightarrow Mg^{2+} + 2Cl^- + 6H_2O$
$Mg_2Cl(OH)_3 \bullet 4H_2O$(phase 3) + $3H^+ \leftrightarrow 2Mg^{2+} + Cl^- + 7H_2O$
$Mg_2CaCl_6 \bullet 12H_2O$(tachyhydrite) $\leftrightarrow 2Mg^{2+} + Ca^{2+} + 6Cl^- + 12H_2O$
$KMgCl_3 \bullet 6H_2O$(carnallite) $\leftrightarrow K^+ + Mg^{2+} + 3Cl^- + 6H_2O$
$MgCO_3$(magnesite) + $H^+ \leftrightarrow Mg^{2+} + HCO_3^-$
$MgCO_3 \bullet 3H_2O$(nesquehonite) + $H^+ \leftrightarrow Mg^{2+} + HCO_3^- + 3H_2O$
$Mg_4(CO_3)_3(OH)_2 \bullet 3H_2O$(hydromagnesite4323) + $5H^+ \leftrightarrow 4Mg^{2+} + 3HCO_3^- + 5H_2O$
$Mg_5(CO_3)_4(OH)_2 \bullet 4H_2O$(hydromagnesite5424) + $6H^+ \leftrightarrow 5Mg^{2+} + 4HCO_3^- + 6H_2O$
$K_2Mg(SO_4)_2 \bullet 4H_2O$(leonite) $\leftrightarrow 2K^+ + Mg^{2+} + 2SO_4^{2-} + 4H_2O$
$Na_2Mg(SO_4)_2 \bullet 4H_2O$(bloedite) $\leftrightarrow 2Na^+ + Mg^{2+} + 2SO_4^{2-} + 4H_2O$
$MgSO_4 \bullet 7H_2O$(epsomite) $\leftrightarrow Mg^{2+} + SO_4^{2-} + 7H_2O$
$MgSO_4 \bullet 6H_2O$(hexahydrite) $\leftrightarrow Mg^{2+} + SO_4^{2-} + 6H_2O$
$MgSO_4 \bullet H_2O$(kieserite) $\leftrightarrow Mg^{2+} + SO_4^{2-} + H_2O$
$CaMg(CO_3)_2$(dolomite) + $2H^+ \leftrightarrow Ca^{2+} + Mg^{2+} + 2HCO_3^-$
$K_2Mg(SO_4)_2 \bullet 6H_2O$ (picromerite) $\leftrightarrow 2K^+ + Mg^{2+} + 2SO_4^{2-} + 6H_2O$
$K_2MgCa_2(SO_4)_4 \bullet 2H_2O$ (polyhalite) $\leftrightarrow 2K^+ + Mg^{2+} + 2Ca^{2+} + 4SO_4^{2-} + 2H_2O$
$KMgClSO_4 \bullet 3H_2O$(kainite) $\leftrightarrow K^+ + Mg^{2+} + Cl^- + SO_4^{2-} + 3H_2O$

GEOCHEM-3.2.4 Organic Ligand Parameters

Organic ligand reactions and Pitzer interactions in DATA0.FM6 (Domski 2023a) for CRA-2026, Table GEOCHEM-8,

Table GEOCHEM-8. EDTA Reactions for CRA-2026

EDTA Reactions
$H_4EDTA(aq) \leftrightarrow EDTA^{4-} + 4H^+$
$H_3EDTA^- \leftrightarrow EDTA^{4-} + 3H^+$
$H_2EDTA^{2-} \leftrightarrow EDTA^{4-} + 2H^+$
$HEDTA^{3-} \leftrightarrow EDTA^{4-} + H^+$
$MgEDTA^{2-} \leftrightarrow Mg^{2+} + EDTA^{4-}$
$CaEDTA^{2-} \leftrightarrow Ca^{2+} + EDTA^{4-}$

Table GEOCHEM-9. Citrate Reactions for CRA-2026

Citrate Reactions
$Ca_3(Citrate)_2 \bullet 4H_2O$ (earlandite) $\leftrightarrow 3Ca^{2+} + 2Citrate^{3-} + 4H_2O$
$H_3Citrate (aq) \leftrightarrow 3H^+ + Citrate^{3-}$
$H_2Citrate^- \leftrightarrow Citrate^{3-} + 2H^+$
$HCitrate^{2-} \leftrightarrow Citrate^{3-} + H^+$
$MgCitrate^- \leftrightarrow Mg^{2+} + Citrate^{3-}$
$CaCitrate^- \leftrightarrow Ca^{2+} + Citrate^{3-}$

Table GEOCHEM-10. Oxalate, Lactate, and Acetate Reactions for CRA-2026

Oxalate, Lactate, and Acetate Reactions
$NaHOxalate \bullet H_2O(s) \leftrightarrow Na^+ + H^+ + Oxalate^{2-} + H_2O$
$Na_2Oxalate(s) \leftrightarrow 2Na^+ + Oxalate^{2-}$
$CaOxalate \bullet H_2O(s)(whewellite) \leftrightarrow Ca^{2+} + Oxalate^{2-} + H_2O$
$MgOxalate \bullet 2H_2O(s)(glushinskite) \leftrightarrow Mg^{+2} + Oxalate^{-2} + 2H_2O$
$H_2Oxalate \bullet 2H_2O(s) \leftrightarrow Oxalate^{2-} + 2H^+ + 2H_2O$
$H_2Oxalate(aq) \leftrightarrow Oxalate^{2-} + 2H^+$
$HOxalate^- \leftrightarrow Oxalate^{2-} + H^+$
$MgOxalate(aq) \leftrightarrow Mg^{2+} + Oxalate^{2-}$
$MgOxalate_2^{2-} \leftrightarrow Mg^{2+} + 2Oxalate^{2-}$
$CaOxalate(aq) \leftrightarrow Ca^{2+} + Oxalate^{2-}$

Oxalate, Lactate, and Acetate Reactions
$HLactate(aq) \leftrightarrow H^+ + Lactate^-$
$HAcetate(aq) \leftrightarrow H^+ + Acetate^-$
$MgAcetate^+ \leftrightarrow Mg^{2+} + Acetate^-$
$CaAcetate^+ \leftrightarrow Ca^{2+} + Acetate^-$

Pitzer interactions for organic ligands in DATA0.FM6 (Domski 2023a) for CRA-2026 are shown in Table GEOCHEM-11. They have not changed since CRA-2019.

Table GEOCHEM-11. Organic Ligand Pitzer Interactions for CRA-2026

Cation - Anion	**Na^+**	**K^+**
$EDTA^{4-}$	x	x
$HEDTA^{3--}$	x	x
H_2EDTA^{2-}	x	x
H_3EDTA^-	x	x
$CaEDTA^{2-}$	x	x
$MgEDTA^{2-}$	x	x
$Citrate^{3-}$	x	x
$HCitrate^{2-}$	x	x
$H_2Citrate^-$	x	x
$CaCitrate^-$	x	x
$MgCitrate^-$	x	x
$Oxalate^{2-}$	x	x
$HOxalate^-$	x	x
Acetate-	x	x
Lactate-	x	x
Anion-Anion	**Cl^-**	
Acetate-	x	
Neutral-Anion	**Cl^-**	
CaOxalate(aq)	x	
MgOxalate(aq)	x	
$CaAcetate^+$	x	
$MgAcetate^+$	x	
Anion-Anion-Cation	**Na^+**	
Cl^-, $Acetate^-$	x	

x: Used.

GEOCHEM-3.2.5 Borate Parameters

Borate reactions in DATA0.FM6 (Domski 2023a) for CRA-2026, Table GEOCHEM-12, have not changed since CRA-2019.

Table GEOCHEM-12. Borate Reactions for CRA-2026

Borate Reactions
$Na_2B_4O_7 \bullet 10H_2O(borax) \leftrightarrow 2Na^+ + 4B(OH)_4^- + 2H^+ + H_2O$
$B(OH)_3(s) + H_2O \leftrightarrow B(OH)_4^- + H^+$
$KB_5O_8 \bullet 4H_2O(K\text{-}pentaborate)\ (s) + 8H_2O \leftrightarrow K^+ + 5B(OH)_4^- + 4H^+$
$K_2B_4O_7 \bullet 4H_2O(K\text{-}tetraborate)\ (s) + 5H_2O \leftrightarrow 2K^+ + 4B(OH)_4^- + 2H^+$
$NaBO_2 \bullet 4H_2O(Na\text{-}metaborate)\ (s) \leftrightarrow Na^+ + B(OH)_4^- + 2H_2O$
$NaB_5O_8 \bullet 5H_2O(Na\text{-}pentaborate)\ (s) + 7H_2O \leftrightarrow Na^+ + 5B(OH)_4^- + 4H^+$
$NaBO_2 \bullet NaCl \bullet 2H_2O(teepleite)\ (s) \leftrightarrow 2Na^+ + B(OH)_4^- + Cl^-$
$B(OH)_3(aq) + H_2O \leftrightarrow B(OH)_4^- + H^+$
$CaB(OH)_4^+ \leftrightarrow Ca^{2+} + B(OH)_4^-$
$MgB(OH)_4^+ \leftrightarrow Mg^{2+} + B(OH)_4^-$
$B_3O_3(OH)_4^- + 5H_2O \leftrightarrow 3B(OH)_4^- + 2H^+$
$B_4O_5(OH)_4^{2-} + 7H_2O \leftrightarrow 4B(OH)_4^- + 2H^+$

Pitzer interactions in DATA0.FM6 (Domski 2023a) for borate for CRA-2026 are shown in Table GEOCHEM-13. They have not changed since CRA-2019.

Table GEOCHEM-13. Pitzer Interactions for Borate for CRA-2026

Cation-Anion	Na^+	K^+	$MgB(OH)_4^+$	$CaB(OH)_4^+$
$B(OH)_4^-$	x	x		
$B_3O_3(OH)_4^-$	x	x		
$B_4O_5(OH)_4^{2-}$	x	x		
Cl^-			x	x
Anion-Anion	**Cl^-**	**HCO_3^-**	**SO_4^{2-}**	
$B(OH)_4^-$	x		x	
$B_3O_3(OH)_4^-$	x	x	x	
$B_4O_5(OH)_4^{2-}$	x	x	x	
Neutral-Cation	**Na^+**	**K^+**	**H^+**	**$MgOH^+$**
$B(OH)_3(aq)$	x	x	x	x
Neutral-Anion	**Cl^-**	**SO_4^{2-}**	**$B_3O_3(OH)_4^-$**	
$B(OH)_3(aq)$	x	x	x	
Anion-Anion-Cation	**Na^+**			
Cl^-, $B(OH)_4^-$	x			
Cl^-, $B_3O_3(OH)_4^-$	x			
Cl^-, $B_4O_5(OH)_4^-$	x			
Neutral-Anion-Cation	**H^+**	**Na^+**		
$B(OH)_3(aq)$, Cl^-	x			
$B(OH)_3(aq)$, SO_4^{2-}	x	x		

x: Used. Single strikethrough: Not used. Double strikethrough: May show up in other tables.

GEOCHEM-3.2.6 Lead Parameters

Lead reactions with chloride, carbonate, and sulfate, Table GEOCHEM-14, were validated with measurements from the literature with the Pitzer activity model (Jang et al. 2021; Jang and Foli 2023; and references cited therein; also see U.S. DOE 2024b; U.S. DOE 2025) and have been added to DATA0.FM6 (Domski 2023a) for CRA-2026. Pitzer parameters are used for lead chloride reactions, but not for lead carbonate and lead sulfate reactions. Lead reactions with organic ligands are not included because measurements in higher ionic strength solutions were not available to test the reaction constants of lead-organic complexation.

Table GEOCHEM-14. Lead Reactions for CRA-2026

Lead Reactions
$PbCl_2(s)$ (Cotunnite) = $Pb^{2+} + 2Cl^-$
$PbCO_3(s)$ (Cerussite) + $H^+ = Pb^{+2} + HCO_3^-$
$NaPb_2(CO_3)_2(OH)(s)$ (Abellaite) + $3H^+ = Na^+ + 2Pb^{2+} + 2HCO_3^- + H_2O$

Lead Reactions
$2PbCO_3.Pb(OH)_2$(s) (Hydrocerussite) + $4H^+ = 3Pb^{2+} + 2HCO_3^- + 2H_2O$
$PbSO_4$(s) (Anglesite) = $Pb^{2+} + SO_4^{2-}$
$PbCl^+ = Pb^{2+} + Cl^-$
$PbCl_2$(aq) = $Pb^{2+} + 2Cl^-$
$PbCl_3^- = Pb^{2+} + 3Cl^-$
$PbHCO_3^+ = Pb^{2+} + HCO_3^-$
$PbCO_3$(aq) + $H^+ = Pb^{2+} + HCO_3^-$
$Pb(CO_3)_2^{2-} + 2H^+ = Pb^{2+} + 2HCO_3^-$
$Pb(CO_3)OH^- + 2H^+ = Pb^{2+} + HCO_3^- + H_2O$
$Pb(CO_3)_3^{4-} + 3H^+ = Pb^{2+} + 3HCO_3^-$

Pitzer interactions for lead for CRA-2026 are shown in Table GEOCHEM-15.

Table GEOCHEM-15. Pitzer Interactions for Lead for CRA-2026

Cation-Anion	**H^+**	**Na^+**	**Mg^{2+}**
$PbCl_3^-$	x	x	x
Cation-Cation	**H^+**		
Pb^{2+}	x		

GEOCHEM-3.2.7 Iron Parameters

Iron solid and aqueous speciation reactions, Table GEOCHEM-16, were validated with measurements from the literature with the Pitzer activity model (Jang et al. 2021; Jang and Foli 2023; and references cited therein). Iron chloride, hydroxide, carbonate, sulfate, EDTA, and citrate reactions are included in DATA0.FM6 (Domski 2023a) for CRA-2026. Again, the formation of $FeEDTA^{2-}$ is suppressed in actinide solubility calculations (also see U.S. DOE 2024b). These parameters have not changed since CRA-2019, except for the inclusion of the Fe-SO_4 solids $FeSO_4.H_2O$(s) (Szomolnokite) and $FeSO_4.7H_2O$(s) (Melanterite).

Table GEOCHEM-16. Iron Reactions for CRA-2026

Iron Reactions
$Fe(OH)_2$(s) (Ferrous Iron Hydroxide) + $2H^+ = Fe^{2+} + 2H_2O$
$Fe_2Cl(OH)_3$(s) (Hibbingite) + $3H^+ = 2Fe^{2+} + Cl^- + 3H_2O$

Iron Reactions
$FeCO_3(s)$ (Siderite) + $H^+ = Fe^{2+} + HCO_3^-$
$Fe_2(OH)_2CO_3(s)$ (Chukanovite) + $3H^+ = 2Fe^{2+} + HCO_3^- + 2H_2O$
$FeSO_4.H_2O(s)$ (Szomolnokite) = $Fe^{2+} + SO_4^{2-} + H_2O$
$FeSO_4.7H_2O(s)$ (Melanterite) = $Fe^{2+} + SO_4^{2-} + 7H_2O$
$FeOH^+ + H^+ = Fe^{2+} + H_2O$
$Fe(OH)_2(aq) + 2H^+ = Fe^{2+} + 2H_2O$
$Fe(OH)_3^- + 3H^+ = Fe^{2+} + 3H_2O$
$Fe(OH)_4^{2-} + 4H^+ = Fe^{2+} + 4H_2O$
$FeCO_3(aq) + H^+ = Fe^{2+} + HCO_3^-$
$Fe(CO_3)_2^{2-} + 2H^+ = Fe^{2+} + 2HCO_3^-$
$FeCitrate^- = Fe^{2+} + Citrate^{3-}$
$FeOHCitrate^{2-} + H^+ = Fe^{2+} + Citrate^{3-} + H_2O$

Pitzer interactions for iron for CRA-2026 are displayed in Table GEOCHEM-17. Except for the addition of Fe-citrate (also see U.S. DOE 2024b), Fe-SO_4, and Fe-EDTA (suppressed) reactions and interactions, they have not changed since CRA-2019.

Table GEOCHEM-17. Pitzer Interactions for Iron for CRA-2026

Cation-Anion	Fe^{2+}	Na^+	
Cl^-	x	~~x~~	
HSO_4^-	x	~~x~~	
SO_4^{2-}	x	~~x~~	
$Fe(CO_3)_2^{2-}$	~~x~~	x	
Cation-Cation	**Na^+**	**Mg^{2+}**	**H^+**
Fe^{2+}	x	x	x
Cation-Cation-Anion	**Cl^-**	**HSO_4^-**	
Fe^{2+}, Na^+	x	~~x~~	
Fe^{2+}, Mg^{2+}	x	~~x~~	
Fe^{2+}, H^+	~~x~~	x	

x: used. Single strikethrough: Not used. Double strikethrough: May show up in other tables.

GEOCHEM-3.3Chemical Conditions Uncertainty Quantification

The range of pcH, ionic strength (I), and total inorganic carbon (C_{TIC}) in WIPP brines estimated in Appendix GEOCHEM-2019 (Appendix GEOCHEM-3.1 Representation of WIPP Chemical

Conditions) were re-analyzed by Domski and Nemer (2023b) who applied ± 3σ rule of thumb expert judgement confidence interval to 31 WIPP brine compositions from Domski (2018). Below are the updated ranges used for CRA-2026:

1. 5.0 m ≤ Ionic Strength ≤ 9.5 m
2. 0.0 ≤ Mg ≤ 1.6 M
3. 0.0 ≤ Ca ≤ 0.5 M
4. 8.5 ≤ pcH ≤ 10.7
5. $0.0 \leq C_{TIC} \leq 2.0 \times 10^{-2}$ M

Otherwise, there have been no changes to the analyses of conceptual model uncertainty, process model uncertainty, or parameterization uncertainty in the Chemical Conditions Model.

GEOCHEM-3.4 Summary of Updates since CRA-2019

The Chemical Conditions Model has been updated since CRA-2019 with: new lead chloride, carbonate, and sulfate reactions (Appendix GEOCHEM-3.2.6 Lead Parameters), new Fe-citrate, and Fe-SO_4 species (Appendix GEOCHEM-3.2.7 Iron Parameters), and inclusion of earlandite (Appendix GEOCHEM-3.2.4 Organic Ligand Parameters).

GEOCHEM-4.0 DISSOLVED ACTINIDE SOURCE TERM

This section is a companion to Appendix SOTERM, which discusses the dissolved actinide source term process model in detail. The material presented here is strictly summary-level information outlining PA implementation of the Dissolved Actinide Source Term conceptual model, process model, parameterization, and quantification of uncertainty. Its inclusion in Appendix GEOCHEM is only for continuity of the narrative thread in the preceding sections. Data sources are described in Appendix SOTERM. The conceptual models and process models for calculating the Dissolved Actinide Source Term for CRA-2026 are the same as those used in CRA-2019 and previous recertifications. Changes to the thermodynamic database and uncertainty distribution applied to baseline solubilities for CRA-2026 are described here.

Calculation of the Dissolved Actinide Source Term feeds PA analysis of disposal area brine release to the ground surface, through the Salado Formation marker beds, and to the Culebra. The Chemical Conditions Conceptual Model, process model, and parameters set the backdrop for the Dissolved Actinide Source Term calculations. There are no new assumptions for CRA-2026.

GEOCHEM-4.1 Dissolved Actinide Source Term Conceptual Model

In addition to the assumptions outlined in Appendix GEOCHEM-3.1 Representation of WIPP Chemical Conditions for the Chemical Conditions Conceptual Model, the following specific assumptions are made in the Dissolved Actinide Source Term Conceptual Model. Further information on the WIPP actinide source term can be found in Appendix SOTERM-6.1 Overview of WIPP Approach to Calculate Mobile Actinide Concentrations and subsections.

GEOCHEM-4.1.1 A Well-Mixed Repository at Equilibrium

The chemistry analogy assumed for determining near-field chemical conditions is that of a batch reactor that has come to equilibrium. Thus, waste is considered well-mixed as directed by 40 CFR § 194.24 (d), the brine likewise, and the possible presence of supersaturated conditions are not assumed to persist in the repository. It follows that brine-chemistry homogeneity will be maintained. Equilibrium is assumed between dissolved actinides and actinide solid phases. Dissolved actinide concentrations will be controlled by equilibrium with anhydrite, halite, MgO, the lead and iron reactants, organic ligands, actinide-bearing solid phases, and the WIPP brines.

GEOCHEM-4.1.2 Use of the Pitzer Model

Actinide solubilities and the chemistry of the near-field environment are calculated using the thermodynamic mass-action approach with the ion-specific aqueous model of Pitzer (Pitzer 1973) as implemented in EQ3/6 Version 8.0a (Wolery and Jarek 2003). The Pitzer model is the most appropriate aqueous model for calculating activity coefficients in high concentration brines such as those observed at the WIPP. The Pitzer aqueous model has been used on the WIPP project since the Compliance Certification Application (CCA) PA.

The EQ3/6 Version 8.0a software package for geochemical modeling consists of two primary codes. The first code, EQ3NR, is an aqueous solution speciation-solubility code that provides the state of the solution and sets up the initial conditions for further reaction-path modeling with EQ6, the second primary code. The EQ3NR code computes the equilibrium state of an aqueous system by determination of the distribution of chemical species employing standard state thermodynamic data and equations describing the thermodynamic activity coefficients of these species in a database.

These species may include solids, simple ions, gases, and ion-complexes. The input files (*.3i) to EQ3NR include information about the aqueous solution, its density, total-dissolved solids, analytical data, and other parameters such as the pH, pcH, or pmH, and redox constraints. EQ3NR input may also include constraints that set the initial conditions for forthcoming EQ6 simulations, such as: equilibrium with a specified pure mineral phase(s), or electrical charge balance for a specific ion.

A list of mineral phases is input in the EQ3NR input file that are to be “suppressed” in subsequent EQ6 simulations: suppressed phases are not allowed to form in the EQ6 run. The choice of which phases are included in this list is based on knowledge of the system being modeled, and the analyst’s expert opinion.

The degree of disequilibrium is evaluated by EQ3NR in terms of the saturation index (SI = log Q/K) for all mineral phases in the thermodynamic database that share a common element, as specified for the aqueous solution in the EQ3NR input file. EQ3NR also calculates the theoretical equilibrium gas fugacity for each gas in the thermodynamic database that shares a common element, as specified for the aqueous solution in the EQ3NR input file.

The chief numerical method employed in EQ3NR is a modified Newton-Raphson technique. EQ3NR produces an output file (*.3o) that contains all input solution properties, and an extensive list of calculated solution properties. EQ3NR creates a “pickup” file (*.3p), which is a shorthand version of the output file that is appended to any future EQ6 input file and is used to initialize an EQ6 reaction path calculation.

After EQ3NR is executed and a pickup file is generated, an EQ6 input file is built to simulate the desired conceptual model. EQ6 calculates reaction paths (chemical evolution) in reacting water-rock and water-rock-waste systems. For the WIPP, EQ6 is used in closed-system titration mode, which means that a specified mass of reactants, from the input file, are added to 1 kg of solution, as specified in the pickup file, and the state of the solution is calculated at every reaction step. As phases become supersaturated, they “precipitate” from solution. The chemistry of the solution may change such that a phase that had previously precipitated may redissolve. The reaction path terminates either when the system reaches equilibrium or when the reactants are exhausted.

For CRA-2026 the thermodynamic database DATA0.FM6 (Domski 2023a) is used for the baseline solubility model and actinide uncertainty analysis (Domski 2025a; Domski 2025b; Domski 2025c). This is a change from CRA-2019 where the DATA0.FM4 database was used. All of the parameters in DATA0.FM6 are documented in Domski (2023a).

GEOCHEM-4.1.3 Use of Standard Brines

The WIPP PA predicts that: (1) intergranular brine could seep into the disposal rooms from the disturbed rock zone (DRZ) in the surrounding Salado Formation after the panels are filled and closed; (2) brine could flow down into the repository from overlying formations if future exploratory drilling inadvertently penetrates the repository; and (3) brine could flow up into the repository from reservoirs in the underlying Castile Formation if drilling penetrates both the repository and a Castile brine reservoir.

The WIPP PA assumes that, in the second case above, brine from formations above the repository would react with Salado minerals to an extent sufficient to produce a composition similar to that of intergranular Salado brines. Furthermore, PA assumes that mixtures of Salado and Castile brines will have compositions and other properties intermediate between these brines, so that actinide solubilities for these end member compositions can be used in PA to bracket expected brine compositions. This eliminates the need for brine-mixing calculations and predictions of solubilities for the resulting mixtures. These assumptions and predictions are described in detail in U.S. DOE (1996; 2004).

GEOCHEM-4.1.4 Oxidation-state Analogy

All actinides in the same oxidation state will form the same aqueous species and isostructural compounds, recognizing that subtle differences in ionic radii and electronic configurations can lead to variations. The solubilities of americium, curium, and plutonium in the +III oxidation state are modeled using the solubility model for americium(III). This model is based on

experimental data for americium(III), curium(III), and the lanthanide analogue neodymium(III). The solubilities of thorium, neptunium, plutonium, and uranium in the +IV oxidation state are modeled using the solubility of thorium(IV). The solubility model for neptunium(V) is based on experimental data for neptunium(V).

GEOCHEM-4.1.5 Redox State of the Actinides

The repository is assumed to be chemically reducing at the time of human intrusion primarily because of iron corrosion and microbial activity. The repository is assumed to realize one of three possible redox states. Actinide chemistry and redox state distributions are described in greater detail in Appendix SOTERM-5.0 WIPP-Relevant Actinide Chemistry and following subsections. The lowest redox state, which assumes solubilities are controlled by the +III oxidation state for Pu and the +IV oxidation state for Np and U, has a 25% chance of being realized. The intermediate redox state, which assumes solubilities are controlled by the +IV oxidation state for Pu, Np, and U, has a 25% chance of being realized. The highest oxidation state, which assumes solubilities are controlled by the +IV oxidation state for Pu, the +V oxidation state for Np, and the +VI oxidation state for U, has a 50% chance of being realized. This is a change from CRA-2019.

The technical basis for the change in redox state probabilities comes from X-ray Absorption Near-Edge Spectroscopy (XANES) analyses of the redox state of Pu in contact with magnetite surfaces in WIPP brine (Kaplan et al. 2025). Magnetite is an expected corrosion product at WIPP that is stabilized by radiolysis. 77 – 99% of magnetite-associated Pu was measured to be in the Pu(IV) state (Kaplan et al. 2025, Figure 2b).

GEOCHEM-4.1.6 Effect of Organic Ligands

The organic ligand concentrations used in CRA-2026 include the entire inventory of acetate, citrate, EDTA, and oxalate from the PAIR (Van Soest 2025) and a lower minimum brine volume. The effects of organic ligands (acetate, citrate, EDTA, and oxalate) are included in actinide solubility calculations using experimentally derived complexation constants. The effects of competition by calcium and magnesium ions are included, using the complexation constants for calcium and magnesium. Although DATA0.FM6 includes Fe-citrate and Fe-EDTA complexes, only Fe-citrate complexation is used for CRA-2026. Fe-EDTA complexation, which leads to a significant decrease in An(III) solubility, is conservatively suppressed because the Metal-EDTA system has not been completely parameterized (Domski, 2023b). The effect of Fe-citrate and Fe-EDTA complexes on actinide solubilities is described in Domski (2023b).

Iron and lead complexes with EDTA were not considered in actinide solubility calculations. The current WIPP thermodynamic database, DATA0.FM6, includes parameters for Fe-EDTA and Fe – citrate complexes, but no lead organic complexes. It was demonstrated for the RPPCR (Domski 2023b), that Fe – citrate complexes had negligible effect on the actinide solubilities, while the presence of Fe-EDTA complexes caused a significant decrease in the An(III) solubility under WIPP conditions and negligible effect on the +IV and +V actinide solubilities. Further

information on the effect of organic ligands can be found in Appendix SOTERM-3.3 Complexation of Actinides by Organic Complexing Agents and subsections.

GEOCHEM-4.1.7 Immobile Substrates

The Dissolved Actinide Source Term conceptual model specifies that actinides will not be sorbed on repository solids (McCormick et al. 2024), for example, the host rock, waste emplacement materials, and intact or corroded waste packages.

GEOCHEM-4.1.8 Phase Stability/Crystallinity

The Dissolved Actinide Source Term conceptual model provides guidance regarding mineral phase crystallinity and stability. From Wilson (1996) and McCormick et al. (2024): *"A second assumption is that actinide precipitates formed in laboratory experiments will allow the crystallinity to mature with time. Since solids are typically less soluble than amorphous precipitates, laboratory solubility studies can then provide an upper concentration limit."* In other words, the solubility controlling phases for the actinides are the amorphous form.

For CRA-2026 the amorphous forms of Am(III)-hydroxide and Th(IV)-hydroxide are used to set the initial solubilities of the +III and +IV actinides in the solutions, which are then reacted with the repository solids. This is a conservative assumption as it allows the maximum solubilities of each actinide to dissolve in the initial solutions. After reacting with the repository solids, the pH, total carbonate, and f_{CO2} of the initial solutions change and the solubility controlling phase and actinide solubilities vary in accordance with these chemical conditions (Domski 2025a).

GEOCHEM-4.1.9 Solubility-Controlling Phases

The inputs to the model include the solubility-controlling phases used to control the initial An(III), An(IV), and An(V) concentrations. For An(III) the amorphous americium hydroxide phase, $Am(OH)_3$(am) (Jang et al., 2021), was used to set the initial Am(III) concentration. This amorphous phase, contained in DATA0.FM6 as an analogy (Domski 2023a), is new to the WIPP database, and is ~2.4 log units more soluble than the previously used americium hydroxide phase, $Am(OH)_3$(s) of Morss and Williams (1994) The amorphous form of $Am(OH)_3$ was chosen as the solubility controlling phase over more crystalline forms, even though over the long-term the crystalline form may be more prevalent because: the amorphous phase is more soluble and provides an maximum solubility limit and is supported by the dissolved actinide conceptual model (Wilson et al. 1996); and (regarding An(III)-hydroxide phases): *"The use of the notation "crystalline" and "amorphous" to describe a solid phase and thereby its solubility is an oversimplification. The X-ray diffraction (XRD) data give only information of the bulk structure, while the solubility is determined by the surface characteristics or by fractions of smaller ("amorphous") particles included in a bulk crystalline solid."* (Neck et al. 2009).

When the initial solutions are reacted to equilibrium with the important repository solids, and the chemical conditions (pH, total carbonate, and p_{CO2}) change, the stable Am(III) solid phase is $AmOHCO_3$(c) (Domski 2022).

The An(IV) model uses the amorphous form of thorium oxide, $ThO_2(am)$, as the solubility-controlling phase. This phase has been used as the An(IV) solubility-controlling phase since the CCA, and it is consistent with the thorium model included in the database.

The An(V) solubility-controlling phase for CRA-2026 is $KNpO_2CO_3$, as it has been since the CCA.

GEOCHEM-4.2 Dissolved Actinide Source Term Process Models

The Dissolved Actinide Source Term process models consist of chemical reactions, mathematical expressions that represent the chemical reactions, and software that solves the mathematical expressions to obtain relevant chemical conditions. The following sections provide information about the specific chemical reactions involved in the WIPP Dissolved Actinide Source Term. Appendix GEOCHEM-4.1.2, Use of the Pitzer Model, provided a summary of the software used to solve the mathematical expressions. No process model changes are proposed by DOE for the Dissolved Actinide Source Term for CRA-2026.

GEOCHEM-4.2.1 +III Actinides

A comprehensive review of An(III) solubility data is provided in Appendix SOTERM-5.6 Americium and Curium Chemistry and subsections as well as Appendix SOTERM-5.5 Plutonium Chemistry and subsections. Table GEOCHEM-18 shows the Am(III) reactions that are implemented for CRA-2026. These reactions are also used to model Cm(III) and Pu(III) solubilities.

Table GEOCHEM-18. Dissolution and Dissociation Reactions for Americium Solids and Species for CRA-2026.

Am Dissolution and Dissociation Reactions
$AmOHCO_3(s) + 2H^+ \leftrightarrow Am^{3+} + H_2O + HCO_3^-$
$Am(OH)_3(am) + 3H^+ \leftrightarrow Am^{3+} + 3H_2O$
$NaAm(CO_3)_2 \bullet 6H_2O(s) + 2H^+ \leftrightarrow Na^+ + Am^{3+} + 2HCO_3^- + 6H_2O$
$AmCO_3^+ + H^+ \leftrightarrow Am^{3+} + HCO_3^-$
$Am(CO_3)_2^- + 2H^+ \leftrightarrow Am^{3+} + 2HCO_3^-$
$Am(CO_3)_3^{3-} + 3H^+ \leftrightarrow Am^{3+} + 3HCO_3^-$
$Am(CO_3)_4^{5-} + 4H^+ \leftrightarrow Am^{3+} + 4HCO_3^-$
$Am(OH)^{2+} + H^+ \leftrightarrow Am^{3+} + H_2O$
$Am(OH)_2^+ + 2H^+ \leftrightarrow Am^{3+} + 2H_2O$
$Am(OH)_3(aq) + 3H^+ \leftrightarrow Am^{3+} + 3H_2O$
$AmCl^{2+} \leftrightarrow Am^{3+} + Cl^-$

Am Dissolution and Dissociation Reactions
$AmCl_2^+ \leftrightarrow Am^{3+} + 2Cl^-$
$AmSO_4^+ \leftrightarrow Am^{3+} + SO_4^{2-}$
$Am(SO_4)_2^- \leftrightarrow Am^{3+} + 2SO_4^{2-}$
$AmAcetate^{2+} \leftrightarrow Am^{3+} + Acetate^-$
$AmCitrate(aq) \leftrightarrow Am^{3+} + Citrate^{3-}$
$AmEDTA^- \leftrightarrow Am^{3+} + EDTA^{4-}$
$AmLactate^{2+} \leftrightarrow Am^{3+} + Lactate^-$
$AmOxalate^+ \leftrightarrow Am^{3+} + Oxalate^{2-}$

GEOCHEM-4.2.1.1 Americium – Borate Complexation

Nemer (2023a) examined the technical literature on the effects of borate on An(III) solubility and concluded that under WIPP relevant conditions: 1) The borate system is complex and not well understood; and 2) An(III) – borate complexes can form, however, the data do not show that the complexation is significant. Therefore, insufficient data and theory exist to include an An(III)-borate model. An An(III) tetraborate species is not included in CRA-2026.

GEOCHEM-4.2.1.2 Americium – Silica Interactions

The effects of silica on actinide solubility and mobility have been investigated by DOE (Domski 2024; Beam 2022). Beam (2022) studied the effect of silica on the solubility and colloid formation of the +III and +IV actinides. For the +III actinides Beam (2022) found that for WIPP conditions Nd(III) hydrolysis was a “stronger force” than silica complexation and that sequential filtration did not indicate the presence of Nd(III)-silica colloids.

Domski (2024) determined that silica in the waste and the Salado Formation will be available to WIPP brine. While there is an abundance of silica – H_2O thermodynamic parameters, few exist for the silica – An(III) system. Parameters for the latter cannot be confidently extrapolated to WIPP conditions because they were measured at lower ionic strength and pH than WIPP. WIPP relevant measurements of silica-An(III) interactions would be needed to quantify any effect of silica on the current model.

GEOCHEM-4.2.2 +IV Actinides

A comprehensive review of An(IV) solubility data is provided in Appendix SOTERM-5.2 Thorium Chemistry, Appendix SOTERM-5.3 Uranium Chemistry, Appendix SOTERM-5.4 Neptunium Chemistry, Appendix SOTERM-5.5 Plutonium Chemistry, and associated subsections. Table GEOCHEM-19 shows the reactions with Th(IV) that are implemented for CRA-2026. These reactions are also used to model Np(IV), Pu(IV), and U(IV) solubilities.

Table GEOCHEM-19. Dissolution and Dissociation Reactions for Thorium Solids and Species for CRA-2026.

Th Dissolution and Dissociation Reactions
$ThO_2(am) + 4H^+ \leftrightarrow Th^{4+} + 2H_2O$
$Th(SO_4)_2 \bullet 9H_2O(s) \leftrightarrow Th^{4+} + 2SO_4^{2-} + 9H_2O$
$Th(SO_4)_2 \bullet 8H_2O(s) \leftrightarrow Th^{4+} + 2SO_4^{2-} + 8H_2O$
$Th(SO_4)_2 \bullet Na_2SO_4 \bullet 6H_2O(s) \leftrightarrow Th^{4+} + 3SO_4^{2-} + 2Na^+ + 6H_2O$
$Th(SO_4)_2 \bullet K_2SO_4 \bullet 4H_2O(s) \leftrightarrow Th^{4+} + 3SO_4^{2-} + 2K^+ + 4H_2O$
$Th(SO_4)_2 \bullet 2K_2SO_4 \bullet 2H_2O(s) \leftrightarrow Th^{4+} + 4SO_4^{2-} + 4K^+ + 2H_2O$
$2(Th[SO_4]_2 \bullet 7K_2SO_4(s)) \leftrightarrow 2Th^{4+} + 11SO_4^{2-} + 14K^+$
$Th(CO_3)_5^{6-} + 5H^+ \leftrightarrow Th^{4+} + 5HCO_3^-$
$Th(OH)_3(CO_3)^- + 4H^+ \leftrightarrow Th^{4+} + 3H_2O + HCO_3^-$
$Th(OH)_4(aq) + 4H^+ \leftrightarrow Th^{4+} + 4H_2O$
$Th(SO_4)_2(aq) \leftrightarrow Th^{4+} + 2SO_4^{2-}$
$Th(SO_4)_3^{2-} \leftrightarrow Th^{4+} + 3SO_4^{2-}$
$ThAcetate^{3+} \leftrightarrow Th^{4+} + Acetate^-$
$Th(Acetate)_2^{2+} \leftrightarrow Th^{4+} + 2Acetate^-$
$ThCitrate^+ \leftrightarrow Th^{4+} + Citrate^{3-}$
$ThEDTA(aq) \leftrightarrow Th^{4+} + EDTA^{4-}$
$ThLactate^{3+} \leftrightarrow Th^{4+} + Lactate^-$
$Th(Lactate)_2^{2+} \leftrightarrow Th^{4+} + 2Lactate^-$
$ThOxalate^{2+} \leftrightarrow Th^{4+} + Oxalate^{2-}$

GEOCHEM-4.2.2.1 Thorium(IV) – Silica Interactions

Beam (2022) examined the solubility and possibility of colloid formation of $U(OH)_4(s)$ in 5M NaCl solutions at WIPP relevant pH values with 4 mM silica. There was no effect of silica on U(IV) solubility at pH 9; sequential filtration showed that no U(IV) colloids were present. Beam (2022) did observe a slight increase in U(IV) solubility at pH > 10, outside the expected WIPP pH range, that he attributed to the $An(OH)(H_3SiO_4)_3^{2-}$ aqueous species.

Domski (2024) included the $An(OH)(H_3SiO_4)_3^{2-}$ aqueous species of Rai et al. (2008) in the EQ3/6 database and verified that it provided an acceptable fit to the experimental training data used to fit the log K value. Application of the Si – An(IV) model to the RPPCR baseline solubility

model showed that the An(IV) – silica aqueous species slightly increased the total An(IV) solubility in the RPPCR baseline solubility model.

GEOCHEM-4.2.3 +V Actinides

A comprehensive review of An(V) solubility data is provided in Appendix SOTERM-5.4 Neptunium Chemistry and subsections. The reactions for An(V) included in the CCA, and that have been included in all recertifications since, are included in CRA-2026. Table GEOCHEM-20 shows the reactions with Np(V) that are implemented for CRA-2026.

Table GEOCHEM-20. Dissolution and Dissociation Reactions for Neptunium Solids and Species for CRA-2026.

Np Dissolution and Dissociation Reactions
$NpO_2OH(aged) + H^+ \leftrightarrow NpO_2^+ + H_2O$
$NpO_2OH(am) + H^+ \leftrightarrow NpO_2^+ + H_2O$
$2(NaNpO_2CO_3 \bullet 7/2H_2O)(s) + 2H^+ \leftrightarrow 2NpO_2^+ + 2HCO_3^- + 2Na^+ + 7H_2O$
$Na_3NpO_2(CO_3)_2(s) + 2H^+ \leftrightarrow NpO_2^+ + 2HCO_3^- + 3Na^+$
$KNpO_2CO_3(s) + H^+ \leftrightarrow NpO_2^+ + HCO_3^- + K^+$
$K_3NpO_2(CO_3)_2(s) + 2H^+ \leftrightarrow NpO_2^+ + 2HCO_3^- + 3K^+$
$NpO_2CO_3^- + H^+ \leftrightarrow NpO_2^+ + HCO_3^-$
$NpO_2(CO_3)_2^{3-} + 2H^+ \leftrightarrow NpO_2^+ + 2HCO_3^-$
$NpO_2(CO_3)_3^{5-} + 3H^+ \leftrightarrow NpO_2^+ + 3HCO_3^-$
$NpO_2(OH)(aq) + H^+ \leftrightarrow NpO_2^+ + H_2O$
$NpO_2(OH)_2^- + 2H^+ \leftrightarrow NpO_2^+ + 2H_2O$
$NpO_2Acetate(aq) \leftrightarrow NpO_2^+ + Acetate^-$
$NpO_2Citrate^{2-} \leftrightarrow NpO_2^+ + Citrate^{3-}$
$NpO_2H_2EDTA^- \leftrightarrow NpO_2^+ + EDTA^{4-} + 2H^+$
$NpO_2HEDTA^{2-} \leftrightarrow NpO_2^+ + EDTA^{4-} + H^+$
$NpO_2EDTA^{3-} \leftrightarrow NpO_2^+ + EDTA^{4-}$
$NpO_2Lactate(aq) \leftrightarrow NpO_2^+ + Lactate^-$
$NpO_2Oxalate^- \leftrightarrow NpO_2^+ + Oxalate^{2-}$

GEOCHEM-4.3 Parameterization of Dissolved Actinide Source Term Process Models

Table GEOCHEM-21 shows the An solubilities in the +III, +IV, +V, and +VI oxidation states, respectively, which were calculated using the 1x minimum brine volumes of the Salado and

Castile brines by EQ3/6 and utilized by PA for CRA-2026. CRA-2026 An(III) solubilities are higher than CRA-2019 values because of changes in the parameterization of An(III) speciation and solubility (Domski 2023b, Section 4), and because the CRA-2026 minimum brine volume is substantially lower than the CRA-2019 value. The lower brine volume increases the organic ligand concentrations assumed in the solubility calculation which increases calculated An(III) solubilities due to the formation of more An(III)-EDTA complexes (Domski 2025a, Section 4). An(IV)s do not form strong complexes with organic ligands. Rather, they form hydroxide and hydroxy-carbonate complexes that are largely unaffected by the change in minimum brine volume and organic ligand levels. An(V)s form stronger complexes with acetate and oxalate accounting for their moderate solubility increases in CRA-2026 (Domski 2025a, Section 4). For CRA-2019 An(VI) (uranium) concentrations were set to 1.00 x 10^{-3} M, the value specified by the U.S Environmental Protection Agency (EPA) (U.S. EPA 2006). For CRA-2026, uranium concentrations are set to 3.00 x 10^{-6} M (Kaplan et al. 2025).

Table GEOCHEM-21. Actinide Solubilities (M) for CRA-2026. CRA-2019 DPA values in parentheses.

	An(III)	An(IV)	An(V)	An(VI)
Salado (GWB)	1.45 x 10^{-5} (1.63 x 10^{-7})	5.34 x 10^{-8} (5.45 x 10^{-8})	9.75 x 10^{-7} (4.02 x 10^{-7})	3.00 x 10^{-6} (1.00 x 10^{-3})
Castile (ERDA-6)	1.44 x 10^{-5} (1.78 x 10^{-7})	5.63 x 10^{-8} (5.44 x 10^{-8})	4.01 x 10^{-6} (1.20 x 10^{-6})	3.00 x 10^{-6} (1.00 x 10^{-3})

GEOCHEM-4.3.1 +III Actinide Parameters

The An(III) model implemented in the WIPP thermodynamic database has been relatively unchanged since Sandia National Laboratories (SNL) did an analysis of the Neck et al. (2009) study (Domski 2022), hereafter the "Neck model". Only a broad summary of Domski (2022) is provided herein (also see U.S. DOE 2024b). Neck et al. performed undersaturation experiments using $Nd(OH)_3(cr)$, which was used as the solubility controlling phase in matrix solutions of NaCl, $MgCl_2$, and $CaCl_2$ of 0.1, 0.5, 2.5, and 5.0 M for NaCl, and 0.25, 1.0, 2.5, 3.5 M for $MgCl_2$, and $CaCl_2$. The Neck et al. (2009) laboratory solubility data which is most representative of expected WIPP conditions are those collected in 5.0 M NaCl, 0.25 $MgCl_2$, and $CaCl_2$ matrix solutions. These are compared to the WIPP An(III) model below.

Based on their experimental data, Neck et al. (2009) derived a log K value for the $Nd(OH)_3(s)$ phase, and Neck states that their derived value falls between that of 18.66 ± 0.55 for fresh, amorphous precipitates of $Nd(OH)_3(s)$ and 16.02 ± 0.37 for aged and crystalline $Nd(OH)_3(s)$. Since a crystalline form of $Nd(OH)_3$ was identified in the post-test solids analysis of (Neck et al. 2009) it may be expected that the derived log K would reflect the higher crystallinity, however, the solubility might be controlled by more amorphous particles. This may explain why Neck's value of log K for $Nd(OH)_3(s)$ (17.2 ± 0.4) is intermediate between the amorphous and crystalline values of other authors. That is, while the system is far from equilibrium, the XRD

only detects the crystalline phase, whereas the solubility experimental measurements reflect the most soluble fraction of the $Nd(OH)_3$ solid.

Figure GEOCHEM-1 below, recreates Figures 1D and 2A (Domski 2022) showing the Neck model (both log K values and Pitzer parameters) fit to the experimental data of (Neck et al. 2009). Figure GEOCHEM-1 shows that the Neck derived log K value fits their measured NaCl, $MgCl_2$, and $CaCl_2$ data very well, as would be expected.

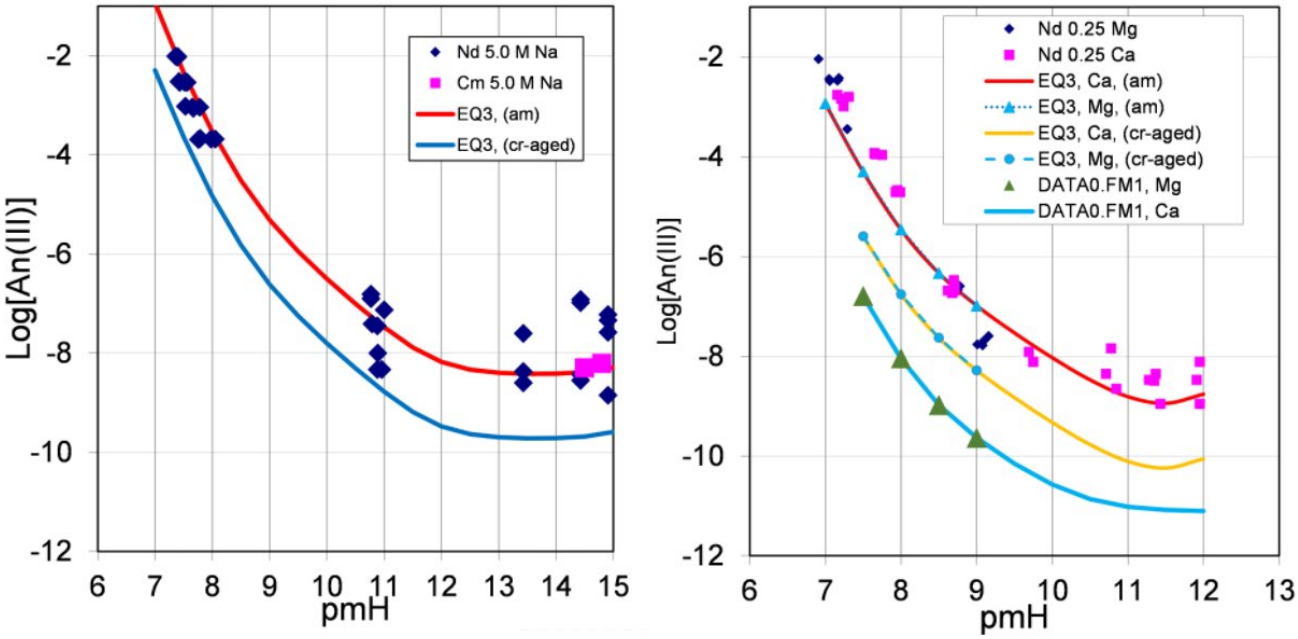


Figure GEOCHEM-1. pH-Dependent An(III) Solubility for 5.0 M NaCl (left) and 0.25 M $MgCl_2$ and $CaCl_2$ Solutions (right). Measured Data (dark blue diamonds, pink squares) and EQ3/6 Simulations (all others) of amorphous (am) Am-hydroxide phase (more soluble) and crystalline aged (cr-aged) Am-hydroxide phase (less soluble) displayed by matrix cation (Figure 1D and Figure 2A from [Domski 2022]).

In addition to implementing the Neck model in a test database, Domski (2022) examined the stability field of Am(III) solids for WIPP conditions and applied the Neck model to the CRA-2019 actinide solubility model. The results showed that for WIPP conditions $AmOHCO_3$(c) was more stable than $Am(OH)_3$(am), and that $Am(OH)_3$(s) was more stable than $AmOHCO_3$(c). The source of the log value for $Am(OH)_3$(s) was Morss and Williams (1994) in their paper describe the phase crystallinity: *From an evaluation of all thermodynamic data on lanthanide and actinide trihydroxides, we recommend log Ksp[$Pu(OH)_3$] = -(26.5 ± 2) and log Ksp [$Am(OH)_3$] = -(27.5 ±2. We conclude that crystalline $Am(OH)_3$ is significantly more stable with respect to its aqueous solution than has been predicted from lanthanide analogues or from solubility measurements on precipitates. We believe that this stability reflects the behavior of well-crystallized $Am(OH)_3$ in comparison with amorphous or "microcrystalline" $Am(OH)_3$.* Because $Am(OH)_3$(s) does not represent the amorphous form it is eliminated by the assumption of the dissolved actinide

conceptual model (Wilson et al., 1996). Thus, $AmOHCO_3$(c) becomes the solubility controlling phase in the WIPP (also see U.S. DOE 2024b).

Application of the Neck model to the baseline solubility model in the CRA-2019 and CRA-2026 was done for both the GWB and ERDA-6 brines at the five brine volumes. The results confirmed that $AmOHCO_3$(c) became the solubility controlling phase for both brine types. In addition, the total An(III) concentration was virtually unchanged, in other words, there was no impact on the An(III) concentration.

GEOCHEM-4.3.1.1 Comparison of the WIPP and Neck Models for An(III) Solubility

To compare the WIPP An(III) model to that of Neck, simulations comparing the three models to An(III) solubility data measured in 5 M NaCl from various authors are plotted in Figure GEOCHEM-2. The first feature to note in Figure GEOCHEM-2 is the scatter in the measured An(III) concentrations, which in extreme cases is 3 log units at a fixed pH. This spread in concentration highlights the difficulty and uncertainty of measuring concentrations at such low levels in high ionic strength solutions. The second feature to note in Figure GEOCHEM-2 is that each model provides an adequate fit when the spread in the measured data is considered. For the purposes of the Dissolved Actinide Source Term, Model 1, has been employed for the CRA-2026 to set the initial Am(III) concentration. This amounts to a net bias towards greater solubility than would be inferred from the majority of the data alone, i.e., Model 1 is conservative.

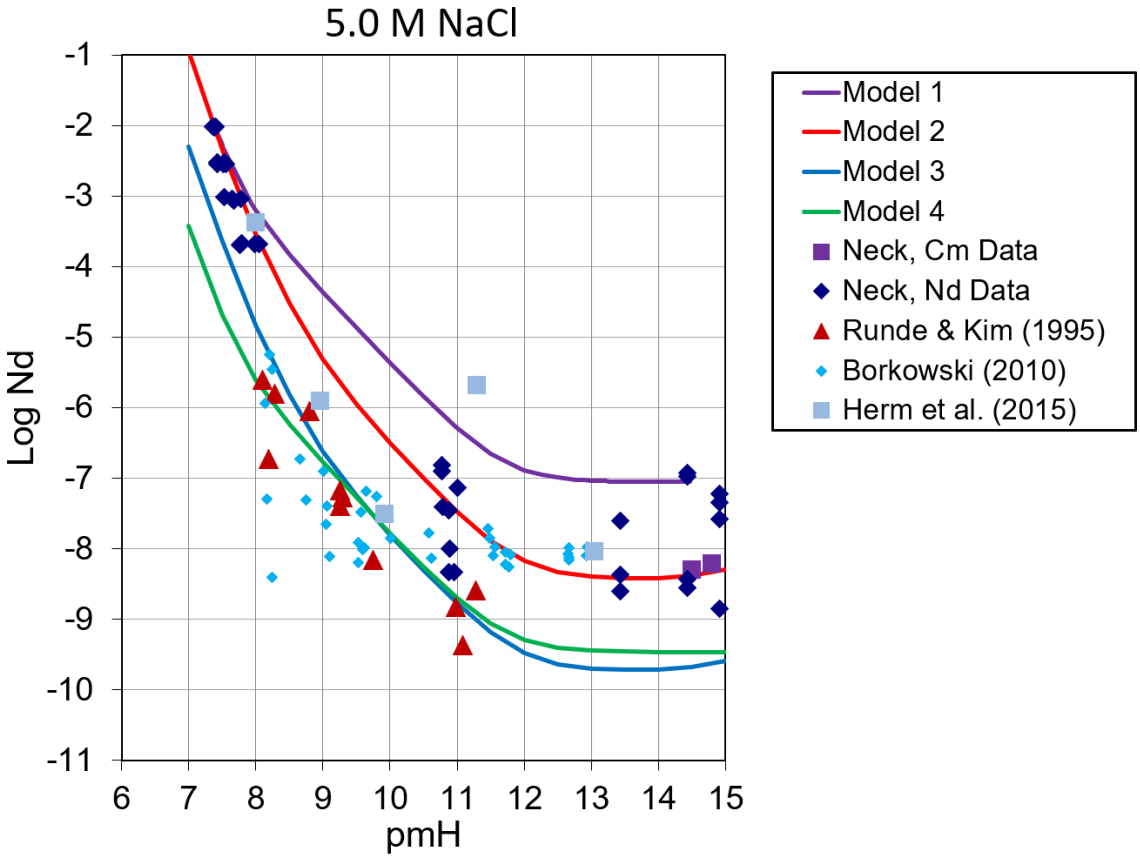


Figure GEOCHEM-2. An(III) Models Compared to Measured An(III) Data

Model descriptions follow:

- Model 1 and 2: The WIPP model, Model 1 DATA0.FM1 with the $Am(OH)_3$(am) log K (16.9) of Guillaumont (2003) from GEOC-21-11 (Jang et al. 2021) used in DATA0.FM6; Model 2 DATA0.FM1 $Am(OH)_3$(s) legacy value of Morss and Williams (1994) as solubility controlling phase.
- Model 3 and 4: The Neck model, DATA0.FM1 with the Neck et al. (2009) model fully implemented (i.e., Log K values of aqueous species and Pitzer parameters), Model 2 using the $Am(OH)_3$(am) log K, and Model 3 $Am(OH)_3$(cr-aged) values of Guillaumont (2003) as recommended by Neck, and documented in Domski (2022); the Neck model qualitatively provides a good fit to their measured data, however, for the An(III) – Cl – H_2O system a total of ~33 parameters, Log K values plus Pitzer parameters, are required to fit the measured data. With such a large degree of freedom the relative uncertainty of the parameters increases. In addition, the Neck model underpredicts other data sets for similar conditions**Error! Reference source not found.**, therefore the Neck model was not implemented for CRA-2026.
-

For CRA-2026 the WIPP model as presented in Figure GEOCHEM-2 above was used as implemented in DATA0.FM6. There are no parameter changes from the An(III) reactions that were implemented in CRA-2019, with the exception of the addition of $Am(OH)_3(am)$ and the Pitzer parameter for Mg^{2+} - $Am(OH)_2^+$ recommended by Jang et al. (2021). Table GEOCHEM-22 provides the updates to the Am(III) system implemented in DATA0.FM6 for CRA-2026 as documented in Jang et al. (2021) and Domski (2023a).

Table GEOCHEM-22. Amorphous Am(III) - Hydroxide Log K values and Pitzer parameters for the $Nd(OH)_3(s)$ - $MgCl_2$ - H_2O system. From Jang et al. (2021).

Reaction		log K	Source
$Am(OH)_3(am) + 3H^+ \leftrightarrow Am^{3+} + 3H_2O$		16.9	Guillaumont et al. (2003)
i	***j***	**θ_{ij}**	**Source**
$Am(OH)_2^+$	Mg^{2+}	0.302	Jang et al. (2021)

Pitzer interactions in DATA0.FM6 for Am^{3+} (An^{3+}) for CRA-2026 are shown in Table GEOCHEM-23.

Table GEOCHEM-23. Pitzer Interactions for Am^{3+} for CRA-2026

Cation-Anion	$Am(CO_3)_2^-$	$Am(CO_3)_3^{3-}$	$Am(CO_3)_4^{5-}$	$Am(SO_4)_2^-$	$AmEDTA^-$	Cl^-	ClO_4^-	SO_4^{2-}	$H_2PO_4^-$
Am^{3+}						x	x	x	x
Na^+	x	x	x	x	x				
K^+	x	x	x	x	x				
Mg^{+2}									
$AmCO_3^+$						x			
$Am(OH)_2^+$						x			
$AmSO_4^+$						x			
$AmCl^{2+}$						x			
$AmCl_2^+$						x			
$AmOH^{2+}$						x			
$AmLactate^{2+}$						x			
$AmAcetate^{2+}$						x			
$AmOxalate^+$						x			
Cation-Cation	**Na^+**	**K^+**	**Ca^{2+}**	**Mg^{2+}**					
Am^{3+}	x	x	x	x					
$AmCl_2^+$			x	x					
$AmCl^{2+}$			x	x					
$Am(OH)_2^+$				x					
Neutral-Cation	**H^+**	**Na^+**	**K^+**						
$Am(OH)_3(aq)$	x	x	x						
Neutral-Anion	**Cl^-**								
$Am(OH)_3(aq)$	x								
$AmCitrate(aq)$	x								

x: Used. Single strikethrough: Not used. Double strikethrough: May show up in other tables.

GEOCHEM-4.3.2 +IV Actinide Parameters

There are no parameter changes from the An(IV) reactions that were implemented in CRA-2019. Pitzer interactions in DATA0.FM6 for Th^{4+} for CRA-2026 are shown in Table GEOCHEM-24.

Table GEOCHEM-24. Pitzer Interactions for Th^{4+} for CRA-2026

Cation-Anion	**$Th(SO_4)_3^{2-}$**	**$Th(CO_3)_5^{6-}$**	**Cl^-**	**ClO_4^-**	**SO_4^{2-}**	**HSO_4^-**
Th^{4+}			x	x	x	x
H^+	x					
Na^+	x	x				
K^+	x	x				
$Th(Acetate)_2^{2+}$			x			
$ThAcetate^{3+}$			x			
$ThCitrate^+$			x			
$ThLactate^{3+}$			x			
$Th(Lactate)_2^{2+}$			x			
$ThOxalate^{2+}$			x			
Cation-Cation	**Na^+**	**K^+**	**Ca^{2+}**	**Mg^{2+}**	**H^+**	
Th^{4+}	x	x	x	x	x	
Anion-Anion	**Cl^-**	**ClO_4^-**				
$Th(CO_3)_5^{6-}$	x	x				
Neutral-Anion	**Cl^-**	**HSO_4^-**				
$Th(SO_4)_2(aq)$	x	x				
ThEDTA(aq)	x					
Cation-Cation-Anion	**Na^+**	**K^+**	**Ca^{2+}**	**Mg^{2+}**	**H^+**	
Th^{4+}, Cl^-	x	x	x	x	x	
Cation-Anion-Anion	**Na^+**	**K^+**				
$Th(CO_3)_5^{6-}$, Cl^-	x	x				

x: Used. Single strikethrough: Not used. Double strikethrough: May show up in other tables.

GEOCHEM-4.3.3 +V Actinide Parameters

There are no parameter changes from the An(V) reactions that were implemented in CRA-2019. Pitzer interactions in DATA0.FM6 for NpO_2^+ for CRA-2026 are shown in Table GEOCHEM-25.

Table GEOCHEM-25. Pitzer Interactions for NpO_2^+ for CRA-2026

Cation-Anion	Na^+	K^+	Ca^{2+}	Mg^{2+}	NpO_2^+
Cl-	~~x~~	~~x~~	~~x~~	~~x~~	x
ClO4-	~~x~~	~~x~~	~~x~~	~~x~~	x
$NpO_2(CO_3)_2^{3-}$	x	x	x	x	~~x~~
$NpO_2(CO_3)_3^{5-}$	x	x	x	x	~~x~~
$NpO_2CO_3^-$	x	x	x	x	~~x~~
$NpO_2Citrate^{2-}$	x	x	~~x~~	~~x~~	~~x~~
$NpO_2Oxalate^-$	x	x	~~x~~	~~x~~	~~x~~
NpO_2EDTA^{3-}	x	x	~~x~~	~~x~~	~~x~~
$NpO_2H_2EDTA^-$	x	x	~~x~~	~~x~~	~~x~~
NpO_2HEDTA^{2-}	x	x	~~x~~	~~x~~	~~x~~
Anion-Anion	**Cl^-**	**CO_3^{2-}**			
$NpO_2(CO_3)_2^{3-}$	x	~~x~~			
$NpO_2(CO_3)_3^{5-}$	x	x			
$NpO_2(OH)_2^-$	x	~~x~~			
$NpO_2CO_3^-$	x	~~x~~			
Neutral-Anion	**Cl^-**				
$NpO_2OH(aq)$	x				
$NpO_2Lactate(aq)$	x				
$NpO_2Acetate(aq)$	x				

x: Used. Single strikethrough: Not used. Double strikethrough: May show up in other tables.

GEOCHEM-4.4 Dissolved Actinide Source Term Uncertainty Quantification

The only uncertainties quantified for the Dissolved Actinide Source Term Model for the purposes of PA are uncertainties in the parametrization of the An(III) and An(IV) models. Appendix GEOCHEM-2019, Section GEOCHEM-4.4 describes uncertainties associated with the conceptual and process models. These discussions will not be repeated below except when a change from the CRA-2019 models has been implemented.

GEOCHEM-4.4.1 Conceptual Model Uncertainty

Conceptual model uncertainty originates in the assumptions that are made in characterizing the modeled system. These assumptions include variables and processes. For example, the mineralogy of the reactants would be considered variables, while the assumption of a well-mixed batch reactor would be classified as a process. Since neither of these assumptions can be tested firsthand, they constitute uncertainty in the conceptual model. Given that it is not possible to test every permutation of possible conceptual models, the result is variability in chemical conditions due to conceptual uncertainty.

GEOCHEM-4.4.1.1 Conceptual Model Uncertainty for An(III)

The use of Nd(III) as an analog for Am(III), and the use of Am(III) as an analogue for Pu(III), are uncertainties in the conceptual model. This uncertainty might be reduced through closer examination of their respective chemical behaviors. Uncertainty associated with the Am-solid that forms was discussed in Appendix GEOCHEM-4.3.1 III Actinide Parameters.

GEOCHEM-4.4.1.2 Conceptual Model Uncertainty for An(IV)

The use of Th(IV) as an analog for each of the An(IV) actinides is an uncertainty in the conceptual model.

The solubility-controlling phase for Th(IV) is amorphous thorium oxide, ThO_2(am). The conceptual model for An(IV) is predicated on the observation that amorphous, rather than crystalline, solids initially precipitate, even though the latter is more thermodynamically stable than the former. This is an expression of Ostwald's Step Rule, in which less soluble crystalline compounds are thermodynamically more stable, but their amorphous counterparts are kinetically favored and tend to precipitate first.

A recent investigation by Simonnet et al. (2016) reported that a fully crystalline state for ThO_2 could only be achieved through a high-temperature (between 850 and 1,500 °C) synthesis route. Attempts to synthesize ThO_2(cr) at room temperature were not successful. These observations support the argument that the WIPP conceptual model should assume that an amorphous or partially crystalline An(IV) phase controls the concentration of aqueous An(IV) in solution. The effect of ThO_2 crystallinity has not been quantified because the conceptual model assumptions are well supported by experimental data.

GEOCHEM-4.4.1.3 Conceptual Model Uncertainty for An(V)

The conceptual model uncertainty has not been quantified for dissolved An(V) because An(V) releases have insignificant effect on the long-term performance of the WIPP (Brush and Garner 2005; Domski 2025c).

GEOCHEM-4.4.2 Process Model Uncertainty

To assess process model uncertainty for the Dissolved Actinide Source Term, variability in calculated dissolved An(III), An(IV), and An(V) concentrations from two brines in six compliance calculations are shown in Table GEOCHEM-26. Process model uncertainty for dissolved actinides is largely uncertainty about which solids and species to include in the process models.

Table GEOCHEM-26. Comparison of Actinide Solubilities (M) for Compliance-Related Calculations from the CCA to CRA-2026.

PA Calculation	Th(IV) (M)	Np(V) (M)	Am(III) (M)
CCA (SPC, Magnesite, without Organics)[1]	4.4×10^{-6}	2.3×10^{-6}	5.82×10^{-7}
PAVT (SPC, Hydromagnesite without Organics)[2]	1.3×10^{-8}	2.4×10^{-7}	1.20×10^{-7}
CRA-2004 PA (GWB, Hydromagnesite, with Organics, Microbes)[3]	1.19×10^{-8}	1.02×10^{-6}	3.07×10^{-7}
CRA-2004 PABC (GWB, Hydromagnesite, with Organics)[4]	5.64×10^{-8}	3.55×10^{-7}	3.87×10^{-7}
CRA-2009 PABC (GWB, Hydromagnesite, with Organics)[5]	5.63×10^{-8}	3.90×10^{-7}	1.66×10^{-6}
CRA-2014 PA ($GWB_{min.\ vol.}$, Hydromagnesite, with Organics)[6]	6.05×10^{-8}	2.77×10^{-7}	2.59×10^{-6}
CRA-2019 ($GWB_{min.\ vol.}$, Hydromagnesite, with Organics, Pb, Fe)[7]	5.45×10^{-8}	4.02×10^{-7}	1.63×10^{-7}
RPPCR ($GWB_{min.\ vol.}$, Hydromagnesite, with Organics, Pb, Fe)[8]	5.34×10^{-8}	4.95×10^{-7}	3.40×10^{-6}
CRA-2026 ($GWB_{min.\ vol.}$, Hydromagnesite, with Organics, Pb, Fe)[9]	5.34×10^{-8}	9.75×10^{-7}	1.45×10^{-5}
CCA (ERDA-6, Magnesite, without Organics)[1]	6.00×10^{-9}	2.20×10^{-6}	6.52×10^{-8}
PAVT (ERDA-6, Hydromagnesite, without Organics)[2]	4.10×10^{-8}	4.80×10^{-7}	1.30×10^{-8}
CRA-2004 PA (ERDA-6, Hydromagnesite, with Organics, Microbes)[3]	2.47×10^{-8}	5.08×10^{-6}	1.69×10^{-7}
CRA-2004 PABC (ERDA-6, Hydromagnesite, with Organics)[4]	6.79×10^{-8}	8.24×10^{-7}	2.88×10^{-7}
CRA-2009 PABC (ERDA-6, Hydromagnesite, with Organics)[5]	6.98×10^{-8}	8.75×10^{-7}	1.51×10^{-6}
CRA-2014 PA ($ERDA\text{-}6_{min.\ vol.}$, Hydromagnesite, with Organics)[6]	7.02×10^{-8}	8.76×10^{-7}	1.48×10^{-6}
CRA-2019 ($ERDA\text{-}6_{min.\ vol.}$, Hydromagnesite, Pb, Fe with Organics)[7]	5.44×10^{-8}	1.20×10^{-6}	1.78×10^{-7}
RPPCR ($ERDA\text{-}6_{min.\ vol.}$, Hydromagnesite, with Organics, Pb, Fe)[8]	5.73×10^{-8}	1.80×10^{-6}	3.51×10^{-6}
CRA-2026 ($ERDA\text{-}6_{min.\ vol.}$, Hydromagnesite, with Organics, Pb, Fe)[9]	5.63×10^{-8}	4.01×10^{-6}	1.44×10^{-5}

1. From Novak et al. (1996) and U.S. DOE (1996), Appendix SOTERM, except that Novak et al. (1996) used molal instead of molar units. U.S. EPA (1998) cited Novak and Moore (1996) as the source of the CCA PA solubilities, but the Am(III) solubilities from Novak and Moore (1996) differ from those in Novak et al. (1996) and U.S. DOE 1996.

2. From Trovato (1997). Novak (1997) also calculated actinide solubilities for the Performance Assessment Verification Test (PAVT), but the EPA used the results of its own calculations.
3. From Brush and Xiong (2003a; 2003b; 2003c; 2003d) and U.S. DOE (2004), Appendix SOTERM.
4 Brush and Xiong (2005a; 2005b) and Brush (2005). These solubilities were also used for the CRA-2009 PA calculations (U.S. DOE 2009).
5. Brush et al. (2009)
6. Brush and Domski (2013)
7. Domski and Sisk-Scott (2019)
8. Domski (2023b)
9. Domski (2025a)

GEOCHEM-4.4.2.1 +III Actinides

Variability in the An(III) solubility derived from process model uncertainty can be discerned readily from Table GEOCHEM-26. The first process model for An(III) solubility did not include hydromagnesite. The CCA solubilities were 5.82×10^{-7} M (SPC brine) and 6.52×10^{-8} M (ERDA-6 brine). Hydromagnesite was added for the PAVT. The solubilities were 1.2×10^{-7} M (Salado PA brine) and 1.3×10^{-8} M (ERDA-6 brine). Organics were not included in the CCA or PAVT, but were added for CRA-2004. The CRA-2004 PABC solubilities were 3.87×10^{-7} M (GWB brine), and 2.88×10^{-8} M (ERDA-6 brine).

The process model change for CRA-2009 PABC was the addition of MgO Phase 5 to the model. The solubilities were 1.66×10^{-6} M (GWB brine) and 1.51×10^{-6} M (ERDA-6 brine). The order of magnitude change in solubility in this case was not because of the process model change; the root cause for the elevated solubility was an increase in the EDTA inventory. In CRA-2004, CRA-2009, and CRA-2014, organic ligand concentrations were PAIR inventory limited, not solubility limited, so any increase in inventory increased the organic ligand concentrations. The lower An(III) solubilities observed for CRA-2019 were caused by changes to the log K values for the EDTA complexes with Mg^{2+} and Ca^{2+} which were relatively stronger than the other CRAs. The increased An(III) solubilities observed for the CRA-2026, were due to decreases in the brine volume which acts to increase the EDTA concentrations, and likewise the total An(III) solubility.

The process model changes discussed above involved changes to the process model for chemical conditions. There have been no changes in the Dissolved Actinide Source Term Process Model.

GEOCHEM-4.4.2.2 +IV Actinides

Table GEOCHEM-26 shows only minor variability in the calculated An(IV) solubility since after the CCA, which ranges from 1.3×10^{-8} to 7.02×10^{-8} M. The hydrolysis of Th^{4+} has been examined by Ekberg et al. (2000), Rai et al. (2000), Moulin et al. (2001), and Okamoto et al. (2003). Hydrolysis of Th^{4+} was critically reviewed by Neck and Kim (2001) and Moriyama et al. (2005) who proposed an alternative process model that includes amorphous $Th(OH)_4(am)$

(Neck et al. 2002; Altmaier et al. 2005; Altmaier et al. 2006), crystalline ThO_2(cr) (Neck et al. 2003), $Th(OH)_3^+$, $Th(OH)_2^{2+}$, $Th(OH)_4$ (aq), $Th_6(OH)_{15}^{9+}$, and $Th_4(OH)_{12}^{4+}$ (Neck et al. 2006). The most abundant aqueous species is $Th(OH)_4$(aq) (Domski, 2023b). The solubility-controlling phase for the Th^{4+}/water system in the WIPP Dissolved Actinide Source Term Process Model is ThO_2(am).

For the Th^{4+} system with carbonate, the WIPP Dissolved Actinide Source Term Process Model includes $Th(CO_3)_5^{6-}$ and $Th(OH)_3(CO_3)^-$. Data from Altmaier et al. (2005) indicates that the use of the pentacarbonyl complex for the IV actinides is a conservative assumption that overpredicts the solubility of the Th^{4+} at pH > 10.

Appendix SOTERM (Section SOTERM-5.0) discusses potential enhancement of An(IV) solubility by calcium. Currently, the WIPP Dissolved Source Term Process Model only includes one interaction with Ca^{2+}, the interaction of Th^{4+} with Ca^{2+}. The DOE contends that this single interaction is sufficient to represent the role that Ca^{2+} may play in dissolving the An(IV) solid, given the calcium levels predicted in the WIPP.

GEOCHEM-4.4.2.3 +V Actinides

The process model uncertainty for dissolved An(V) has not been reexamined because An(V) releases do not affect the long-term performance of the WIPP (Brush and Garner 2005; Domski 2025c).

GEOCHEM-4.4.2.4 +VI Actinides

Previously, EPA specified a fixed value for its estimate of the solubility of U(VI) in GWB and ERDA-6 (U.S. EPA 2006). For CRA-2026 a U(VI) solubility of 3.0×10^{-6} M (Kaplan et al. 2025) is used. Kaplan et al. (2025) cite measured U(VI) solubilities of ~ 1.0×10^{-6} M and 1.77×10^{-6} M derived respectively from undersaturation and oversaturation approaches. These values were averaged, applied a ~ 40% margin of error to achieve ~ 95% confidence, and rounded up to produce the 3.0×10^{-6} M value used by PA.

GEOCHEM-4.4.3 Dissolved Actinide Source Term Uncertainty Analysis from Recent Technical Literature

Uncertainty is also assessed through screening of recent technical literature (Domski and Nemer 2023b) to test the solubility models under expected post-closure repository conditions. First, WIPP literature screening criteria are used to determine which experimental studies, or specific data, or subsets of data, from an experimental study, are included in the actinide uncertainty analysis. Screening criteria include:

G1 – Time Frame: *Preference given to data from studies after January 1990 with the emphasis on the period between the closure date of the most recent recertification cycle and the current recertification cycle. The closure date for the literature search is set to 3-months before the required parameter feed to performance assessment for the current recertification cycle.*

Studies prior to 1990 may be acceptable, provided the experimental and analytical methods are provided and defensible, and satisfies the remainder of the criteria listed herein.

G2 – Sources: *Include data from studies in peer-reviewed journals unpublished undergraduate/graduate theses or dissertations, national and international laboratories, and organizations (e.g., officially released reports from government and educational national and international laboratories.), as well as studies originating from industry.*

G3 – Type of Data: *Include only those studies that provide solubility data. Exclude studies that do not provide solubility data (e.g., studies of corrosion, leaching, sorption, or transport).*

G4 – Solvent and Composition: *Include only data from studies in which water was the solvent and the solution composition characterized; exclude studies in which no aqueous phase was present (e.g., solids, molten metal or salts, or pure organic liquids).*

G5 – Temperature and Pressure: *Include only data obtained from studies that were performed at atmospheric pressures and temperatures of 20 - 30°C.*

G6 *–* ***Use of Oxidation-State Analogs****: Include data from studies that contain actinides currently in the WIPP model, or their appropriate oxidation-state analogs.*

G7 – Phase Characterization and Thermodynamic Equilibrium: *Include data from studies with a well-characterized solubility-controlling solid (both the starting and final solid phases) for which solubility parameters are in the WIPP model. Characterization of the final phase(s) may be complicated due to the presence of low-crystallinity hydrated phases, which may not be easily identified. Methods used for phase identification must be well documented and appropriate for the experimental conditions. The solution separation technique (i.e., dissolved from colloidal) must be well documented and appropriate for the experimental conditions. The experimental procedure should discuss solid-phase synthesis procedures, including descriptions of precursors (solids and solutions); and whether equilibrium (including meta-stability) was obtained. Determination of equilibrium typically includes demonstration of stable concentrations and/or chemical conditions as a function of time.*

G8 – Applicability*: Include data from studies in which the participating chemical components (i.e., aqueous species and solid phases that may affect actinide solubility) are included in the WIPP model. Exceptions include the use of non-participating cations and/or anions, or additional known and characterized dissolved elements that have been demonstrated to not strongly complex or effect the solubility of the actinide(s) of interest.*

G9 – Repeatability and Reproducibility: *Include only data from studies in which: 1) The investigators provided a sufficient description of their experiments to allow the work to be repeated by a qualified investigator; and 2) sufficient experimental data are provided to allow computer simulation of the experiments.*

G10 – WIPP-Relevant Conditions: *Include data from experimental studies carried out under conditions [e.g., pcH, ionic strength, and total inorganic carbon (TIC)] similar to those expected for WIPP, as designated by the Chemical Conditions Conceptual Model.*

Experimental studies/data included in the WIPP actinide uncertainty analysis must meet the following conditions: Ionic strength (m), 5.0 – 9.5; Mg, 0 – 1.6 M; Ca, 0 – 0.5 M; pcH, 8.5 – 10.7; TIC, 0 – 0.02 M.

The screening criteria are intended for use in the WIPP actinide uncertainty analysis, they are NOT intended to be used to select parameters to be included in the WIPP actinide solubility model, i.e., the thermodynamic database. Secondly, the screened results are compared against WIPP actinide solubilities calculated using DATA0.FM6.

The literature screening for CRA-2026, carried out between January 9, 2023, and January 10, 2025, identified five potential experimental studies for the An(IV) actinides. But none met all the screening criteria, so no new literature data were added to the CRA-2026 An(IV) uncertainty analysis. Instead, the same uncertainty distribution that was used for the RPPCR was used for CRA-2026.

The An(III) literature screening identified five potential solubility studies which required in-depth screening to determine eligibility for the CRA-2026 uncertainty analysis, however, only one study met all the screening criteria. The An(III) literature search included: Am(III), Nd(III), Cm(III), and Pu(III). The literature search identified five potential studies with all but one screened out, that of Kutahyali Aslani (2022), which provided six additional data points to the An(III) uncertainty distribution. Kutahyali Aslani (2022) investigated the effect of citrate and EDTA on the solubility of $Nd(OH)_3(s)$. For the first time, the CRA-2026 An(III) uncertainty analysis includes data, three measurements, which account for how the WIPP An(III)-organic model performs and contributes to An(III) solubility uncertainty.

GEOCHEM-4.4.3.1+III Actinides

The histogram and empirical CDF plots for the +III actinides for CRA-2026 (Domski 2025c) are shown in Figure GEOCHEM-3 and Figure GEOCHEM-4 respectively. Sm is the measured solubility, and *S*p is the predicted solubility.

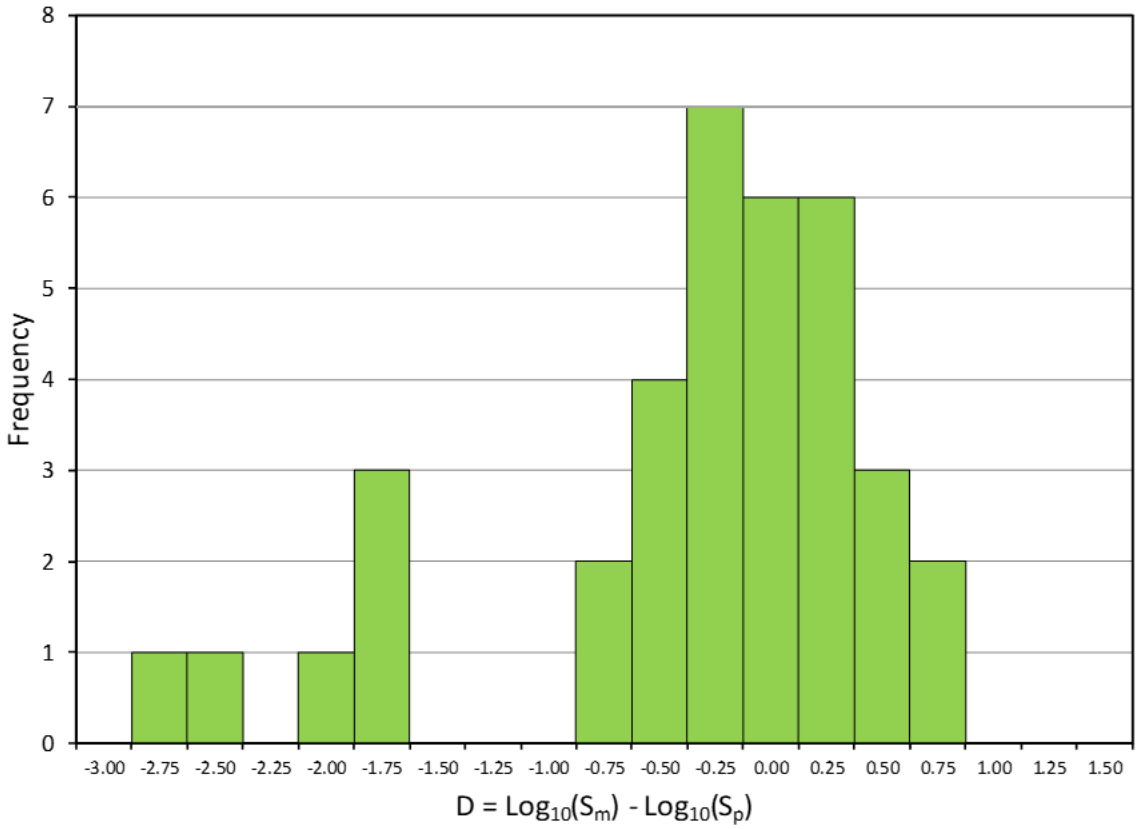


Figure GEOCHEM-3. Histogram of the Difference D = log10 Sm – log10 Sp for Am(III)

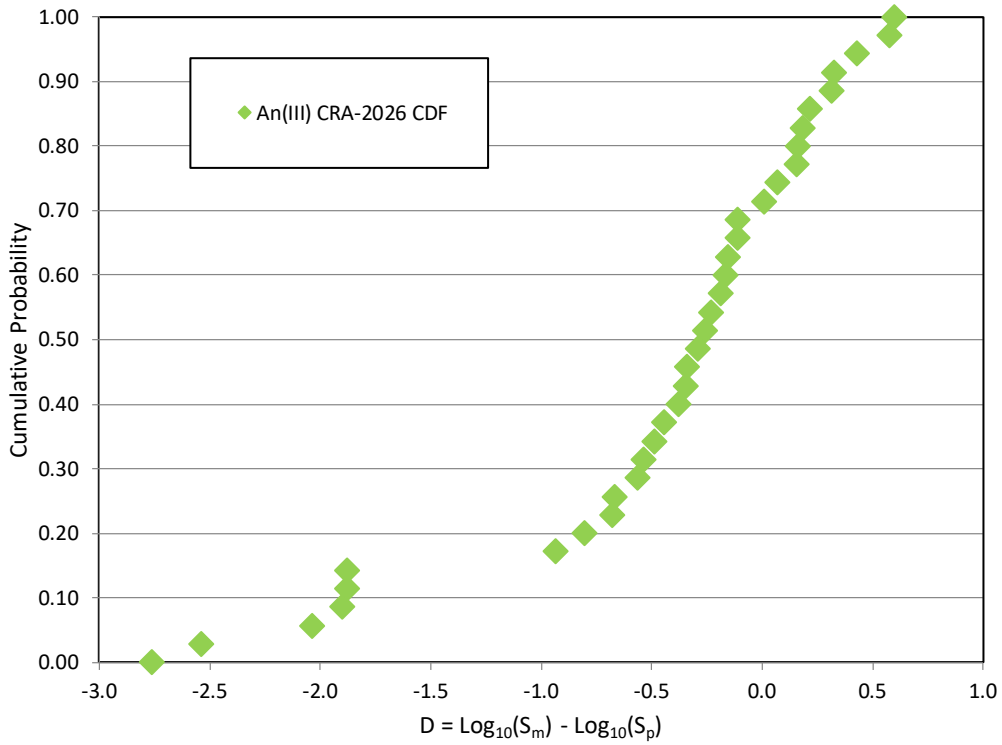


Figure GEOCHEM-4. CDF of the Difference D = log10 Sm – log10 Sp for Am(III)

GEOCHEM-4.4.3.2 +IV Actinides

The histogram and empirical CDF plots for the +IV actinides for the CRA-2026 (Domski 2025c) are shown in Figure GEOCHEM-5. and Figure GEOCHEM-6. respectively.

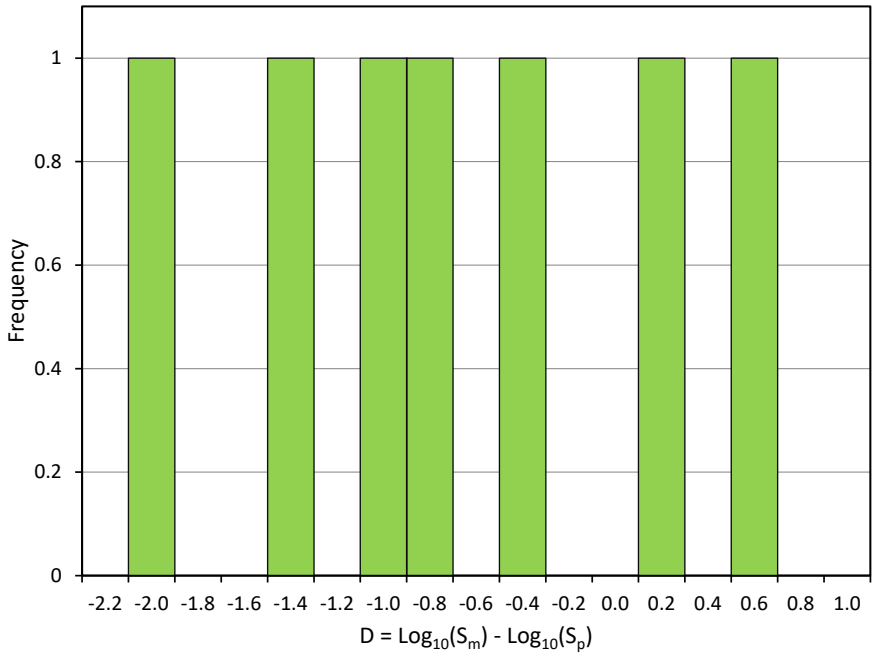


Figure GEOCHEM-5. Histogram of the Difference D = log10 Sm – log10 Sp for Th(IV)

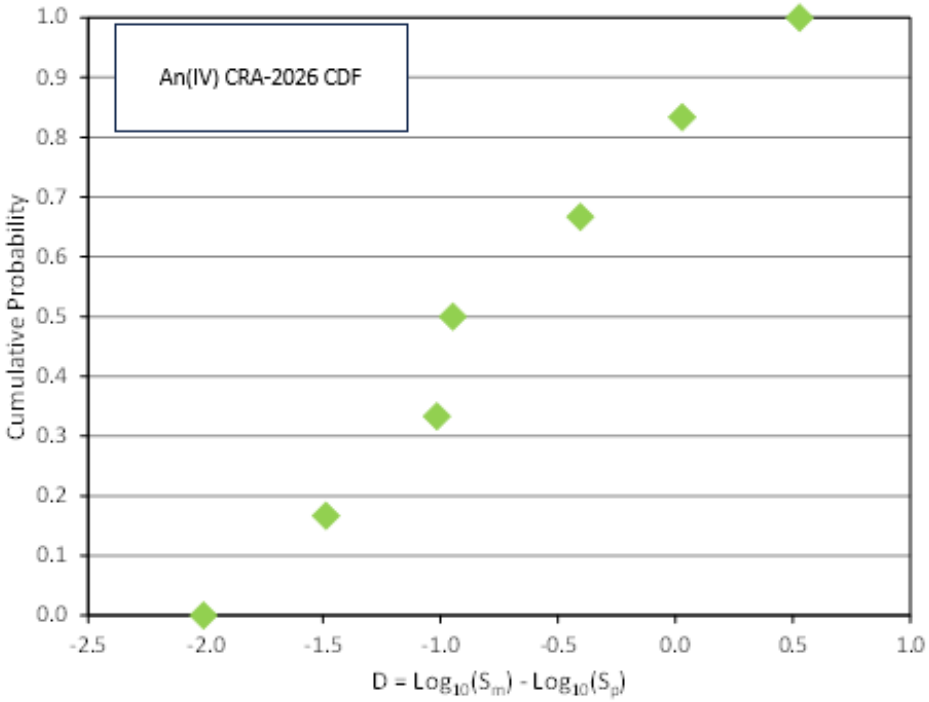


Figure GEOCHEM-6. CDF Plot for the CRA-2026 of the Difference D = log10 Sm – log10 Sp for Th(IV).

GEOCHEM-4.4.4 Alternative Analysis of Actinide Uncertainty

An alternative analysis of actinide uncertainty (Nemer 2023b) that separates bias from error and models bias deterministically and the remainder as stochastic suggests that CRA-2019 An(III) data can be adequately modeled by standard probability distributions after bias correction. The distribution of non-bias-corrected differences between measurements and model predictions is believed to be at least bounding.

GEOCHEM-4.5 Summary of Updates since CRA-2019

The Dissolved Actinide Source Term Model has been updated since CRA-2019 with: a new minimum DBR volume (Appendix GEOCHEM-1.1.1 Brine Volumes), the new thermodynamic database DAT0.FM6 (Appendix GEOCHEM-4.1.2 Use of the Pitzer Model), a refinement of the actinide oxidation state assumption (Appendix GEOCHEM-4.1.5 Redox State of the Actinides), new organic ligand concentrations from the updated PAIR (Appendix GEOCHEM-4.1.6 Effect of Organic Ligands), a new U(VI) solubility (Appendix GEOCHEM-4.4.2.4 +VI Actinides), a new $Am(OH)_3(am)$ log K, and new Pitzer parameters for $Am(OH)_2^+$ - Mg^{2+} (Appendix GEOCHEM-4.3.1.1 Comparison of the WIPP and Neck Models for An(III) Solubility).

CRA-2026 also includes: analyses of An(III) and An(IV)-silica interaction (Appendix GEOCHEM-4.2.1.2 Use of the Pitzer Model and Appendix GEOCHEM-4.2.2.1 Thorium(IV) – Silica Interactions), An(III)-borate interaction (Appendix GEOCHEM-4.2.1.1 Americium – Borate Complexation); An(III) parameterization (Appendix GEOCHEM-4.3.1 +III Actinide Parameters), and an analysis of the effect of Fe-citrate and Fe-EDTA on An solubilities (Domski 2023b). The uncertainty analysis has been updated (Appendix GEOCHEM-4.4.2 Process Model Uncertainty) and compared against newly published experimental data (GEOCHEM-4.4.3 Dissolved Actinide Source Term Uncertainty Analysis from Recent Technical Literature), and an alternative analysis of uncertainty has been described (Appendix GEOCHEM-4.4.4 Alternative Analysis of Actinide Uncertainty).

GEOCHEM-5.0 COLLOIDAL ACTINIDE SOURCE TERM

GEOCHEM-5.1 Colloidal Actinide Source Term Conceptual Model

Colloids are composed of minute particles of phases, ranging in size from approximately one nanometer (nm) to one micron. Colloids can be stable in groundwater, can harbor actinides, and can be transported by groundwater flow. The forms modeled in the WIPP PA are mineral fragment colloids, intrinsic colloids, humic colloids, and microbial colloids (U.S. DOE 1996, Section SOTERM.6.3). Actinide concentrations associated with these colloids contribute directly to WIPP PA total mobile actinide concentrations (U.S. DOE 1996, Section SOTERM.7.2).

Intrinsic colloids are macromolecules of actinides in which the actinides are a structural part of the colloid atomic makeup. These colloids form in the nanometer range and may grow into larger particles. When immature they are hydrophilic, but as they grow, they become

hydrophobic, meaning that the stability of their suspension becomes dependent on the electrostatic interactions within the solution.

Mineral fragment colloids, also known as pseudo-colloids, are hydrophobic hard-sphere particles whose suspensions are stabilized or destabilized by electrostatic forces between their surfaces and the solution. A variety of minerals/substances, either crystalline or amorphous, may form mineral fragment colloids; they are thermodynamically metastable versions of their larger or more crystalline counterpart minerals. Mineral fragment colloids provide sorptive substrates for transporting actinides and can incorporate actinides via coprecipitation mechanisms.

Humic colloids are naturally occurring organic molecules (up to 100,000 atomic mass units) stabilized in water by solvation forces. These colloids provide complexation sites for actinides.

Microbial colloids are stabilized by hydrophilic coatings on microbe surfaces. Microbes provide sorptive substrates for actinides and can also bioaccumulate actinides.

Colloids are included in the WIPP PA because colloids can increase the mobility of actinides (e.g., Abdel-Fattah et al. 2013). The colloid model is implemented in the WIPP PA to guard against the possibility of underestimating the release of actinides. Conservative assumptions are included and described for each colloid type and process model.

GEOCHEM-5.2 Colloidal Actinide Source Term Process Model

The solution composition (particularly the cation concentrations and the solution pH) is a key factor in the rate of colloid aggregation and the stability of colloids. At higher ionic strength and/or pH near the pH of net neutral charge for colloid particles (i.e., the isoelectric point, specific to the colloid, where the concentrations of positive and negative charges on the colloid surface are balanced), the rates of aggregation and flocculation tend to increase, reducing the stability of colloids.

Colloids have a high degree of stability when aggregation rates are low. This condition occurs when repulsive forces of electrostatic double layers are strong enough to prevent colloid particles from coming close enough to each other to bind together by attractive van der Waals forces. Because the chemistry of the water affects the charge and thickness of the double layer, it directly affects the magnitude of the energy barrier that inhibits close particle-particle encounters and hence aggregation. The energy barrier can be approximated by DLVO (Derjaguin and Landau 1941; Verwey and Overbeek 1948) theory by summing van der Waals forces and electric double layer forces as a function of inter-particle distance. Such calculations show that mineral fragment colloids have energy barriers to aggregation that are a function of pH and can decrease to zero at ionic strengths rising only into the tens of mM (millimole per liter) range (e.g., Hu et al. 2010; Abdel-Fattah et al. 2013). Thus, for WIPP brines, which have much higher ionic strengths (approximately 6 mole per liter), energy barriers to particle aggregation are expected to be miniscule, severely limiting radionuclide mobility via mineral fragment colloids. In the case of Pu(IV), its intrinsic colloids can associate with natural

groundwater colloids to form pseudocolloids (Abdel-Fattah et al. 2013). Data also indicate that the presence of humic acids can increase the stability of mineral fragment colloids by (1) increasing the electrostatic repulsion between particles and (2) presenting steric barriers to close encounters between mineral fragment colloid surfaces (Borgnino 2013).

Traexler et al. (2004) and Zhao and Steward (1997) extensively reviewed colloid formation from nuclear waste forms and concluded that all waste forms may yield colloids as they degrade. The models developed for high level waste disposal at Yucca Mountain (Buck and Sassani 2007) focused on both the colloid-formation processes and colloid stability within the waste package and engineered barrier system environments. That work provides a detailed discussion of the chemical environment controls on colloid stability and a rigorous quantitative model of colloid stability.

GEOCHEM-5.2.1 Mineral Fragment Colloids Process Model

The mineral fragment colloids process model considers the maximum concentration of actinides that may be mobilized by mineral fragment colloids. The concentration of mineral fragment colloids is limited by the high ionic strength expected in the waters contacting the waste (Mariner and Sassani 2014). The concentrations of actinides adsorbed to these colloids are further limited by the specific surface areas and sorption site densities of the colloids.

For the CCA, experiments were performed to measure the stability of mineral fragment colloids in WIPP brines. The colloids tested included bentonite, kaolinite, montmorillonite, vermiculite, illite, anhydrite, calcium carbonate, magnesite, hematite, limonite, goethite, magnetite, quartz, siderite, brucite, strontianite, diatomaceous earth, pyrite, and cellulosic materials (U.S. DOE 1996, Appendix SOTERM, Section SOTERM-6.3.1). The brines included simulants of Salado groundwater, "Culebra brine," and a NaCl-$CaCl_2$ solution. These brines were diluted sequentially to produce a set of solutions covering a broad range of salinity (Papenguth 1996, Attachment A).

From these experiments, stable mineral fragment colloid concentrations were converted to actinide concentrations by considering the surface area and sorption site density of the colloids. Assuming spherical particles, the associated (adsorbed) actinide concentration, CONCMIN, for an actinide and its redox state was conservatively determined for the CCA using the following relationship:

$$\text{CONCMIN} = \frac{\pi D^2 N_S N_P}{N_A} f_a f_c \qquad \text{(GEOCHEM.26)}$$

where D is the particle diameter (nm), N_S is the adsorption site density (sites nm^{-2}), N_P is the number of particles per liter of solution determined in the laboratory experiments, N_A is the Avogadro constant, and f_a and f_c are factors used to conservatively account for additional mineral fragment colloids from the Culebra that might sorb actinides (f_a) and to conservatively account for uncertainty (f_c).

Recently, the stability of silica colloids under WIPP conditions was examined (Beam 2022). In that study, no literature data were found that indicate that significant silica colloid concentrations would occur under WIPP conditions. In addition, new laboratory experiments were performed in pH-adjusted 5 M NaCl solutions to study the effect of dissolved silica on the solubility of An(III) and An(IV). No significant colloid fraction was observed and no increase in actinide solubility was observed (Beam 2022).

GEOCHEM-5.2.2 Intrinsic Colloids Process Model

The intrinsic colloid process model is based on intrinsic colloid solubility (U.S. DOE 1996, Section SOTERM.6.3.2; U.S. DOE 2019, Section SOTERM-4.0). Because the solubility of intrinsic colloids is generally low, intrinsic colloids are assumed in the WIPP PA to be present at their solubility limits for each actinide. Further, for actinides with multiple oxidation states, the highest intrinsic colloid solubility is selected among all oxidation states. Accordingly, a single parameter is used in the model to represent the intrinsic colloid contribution of an actinide to total mobile actinide concentrations. That parameter is CONCINT, the solubility-limited molar concentration of the actinide associated with intrinsic colloids.

GEOCHEM-5.2.3 Humic Substance Colloids Process Model

The humic colloids process model is based on the following general aqueous chemical reaction

$$\mathrm{An}^{m+} + \mathrm{Hs} \Leftrightarrow \mathrm{AnHs} \qquad \text{(GEOCHEM.27)}$$

where An^{m+} is the free actinide species concentration, Hs is an available humic substance complexation site, and AnHs is the actinide-humic substance complex (Mariner 2016, Section 4.1). This reaction assumes homogeneous complexation sites with no acido-basic properties and a stability constant that is conditional on pH (Reiller et al. 2008). The conditional stability constant ($\beta_{1:\mathrm{An}^{m+}}$) for this reaction is represented by

$$\beta_{1:\mathrm{An}^{m+}} = \frac{[\mathrm{AnHs}]}{[\mathrm{An}^{m+}][\mathrm{Hs}]} \qquad \text{(GEOCHEM.28)}$$

where brackets denote the equilibrium concentration (M) of the species.

Ca^{2+} and Mg^{2+} are abundant in the WIPP brines. The high concentrations of these cations and their affinity for humic complexation sites act to reduce the concentrations of actinides complexed with humic colloids (U.S. DOE 1996, Section SOTERM.6.3.3.2). The concentration of Hs is calculated from (Mariner 2016, Section 4.1)

$$[\mathrm{Hs}] = \frac{[\mathrm{Hs_{tot}}]}{\beta_{1:\mathrm{An}^{m+}}[\mathrm{An}^{m+}] + \beta_{1:Ca^{2+}}([Ca^{2+}] + [Mg^{2+}]) + 1} \qquad \text{(GEOCHEM.29)}$$

where $\beta_{1:Ca^{2+}}$ is the combined stability constant for the humic complexation of Ca^{2+} and Mg^{2+}, $([Ca^{2+}] + [Mg^{2+}])$ is the sum of the free Ca^{2+} and Mg^{2+} species concentrations (M), and $[\mathrm{Hs_{tot}}]$ is the total concentration (M) of humic complexation sites.

The equilibrium concentration (M) of AnHs is calculated from (Mariner 2016, Section 4.1)

$$[\mathrm{AnHs}] = \frac{\beta_{1:\mathrm{An}^{m+}}[\mathrm{An}^{m+}][\mathrm{Hs}_{tot}]}{\beta_{1:\mathrm{An}^{m+}}[\mathrm{An}^{m+}]+\beta_{1:\mathrm{Ca}^{2+}}([\mathrm{Ca}^{2+}]+[\mathrm{Mg}^{2+}])+1} \qquad \text{(GEOCHEM.30)}$$

The equations presented above are updated from the original CCA process model equations for actinide oxidation states III and IV. These updated equations enhance regulatory compliance by improving the consistency between model calculations and experimental observations for the ranges of pH and ionic strength expected for WIPP brines (Mariner 2016; Mariner 2018). The original CCA model equations for oxidation states III and IV are different in that the total dissolved concentrations of An, Ca, and Mg are used instead of the free species concentrations (U.S. DOE 1996, SOTERM.6.3.3.2).

For oxidation states V and VI, the process model has not been updated since the CCA. In the case of An(V), i.e., Np(V), humic complexation is weak and does not noticeably enhance mobile An(V) concentrations (Appendix GEOCHEM-5.3.3 Humic Colloids Model Parameterization). In the case of An(VI), i.e., U(VI), humic complexation has been limited by CAPHUM (Appendix GEOCHEM-5.3.3 Humic Colloids Model Parameterization).

GEOCHEM-5.2.4 Microbial Colloids Model

The microbial colloids process model determines concentrations of microbially-bound actinides as affected by dissolved actinide concentrations and microbe abundance. The model assumes a linear relationship between the dissolved actinide source term and the microbial colloid concentration of the actinide (U.S. DOE 1996, SOTERM.6.3.4), provided the concentration is below a maximum limit. Maximum microbial actinide concentrations are established using a biomass approach (Kaplan et al. 2025). While this model greatly simplifies the many processes by which microbes may harbor actinides (e.g., adsorption, precipitation, accumulation), it captures the first order effects of primary dependencies on microbial actinide concentrations (Kaplan et al. 2025).

GEOCHEM-5.3 Parameterization of Colloidal Actinide Source Term Process Model

The Table GEOCHEM-28 lists and describes the seven general colloid parameters used in the WIPP PA. The expected values of these parameters in CRA-2026 for the actinides and their oxidation states are shown in Table GEOCHEM-28. These parameters are further addressed in Appendix GEOCHEM-5.3.1 Mineral Fragment Colloids Model Parameterization through Appendix GEOCHEM-5.3.4 Microbial Colloids Model Parameterization.

The mobile actinide concentrations in Castile and Salado brines are calculated in the WIPP PA as shown in Equation (GEOCHEM.31) and Equation (GEOCHEM.32) below, provided (1) sufficient actinide inventory and (2) maximum concentration limit caps for microbial and humic colloids, as defined using CAPHUM and CAPMIC, are not invoked (U.S. DOE 1996, Appendix SOTERM, Section SOTERM-6.2):

$$\text{MobileAnCastile} = [\text{An}]_{\text{Castile}} * (1 + \text{PROPMIC} + \text{PHUMCIM}) + \text{CONCINT} + \text{CONCMIN} \quad \text{(GEOCHEM.31)}$$

$$\text{MobileAnSalado} = [\text{An}]_{\text{Salado}} * (1 + \text{PROPMIC} + \text{PHUMSIM}) + \text{CONCINT} + \text{CONCMIN} \quad \text{(GEOCHEM.32)}$$

Parameter values for $[\text{An}]_{\text{Castile}}$ and $[\text{An}]_{\text{Salado}}$ are provided by the Dissolved Actinide Source Term model (Appendix GEOCHEM-4.0 Dissolved Actinide Source Term). When the calculated humic-colloid-associated actinide concentrations exceed CAPHUM, the humic colloid contributions are limited to CAPHUM. Similarly, when total mobile concentrations exceed CAPMIC, the microbial colloid contributions are limited to CAPMIC.

The PA parameters in Table GEOCHEM-27 and Table GEOCHEM-28 are determined from the process models. Parameterization of the process models is discussed in the subsections below.

Table GEOCHEM-27. WIPP Colloid Model Parameter Summary and Description

Material	Property	Brief Description of Parameter
TH, U, NP, PU, AM	CONCMIN	Concentration of actinide associated with mobile mineral fragment colloids
TH, U, NP, PU, AM	CONCINT	Concentration of actinide associated with mobile intrinsic actinide colloids
TH+4, U+4, U+6, NP+4, NP+5, PU+3, PU+4, AM+3	PROPMIC	Proportionality constant for concentration of actinides associated with mobile microbes
PHUMOX3[1] PHUMOX4 PHUMOX5 PHUMOX6	PHUMCIM	Proportionality constant for concentration of actinides associated with mobile humic colloids; in Castile brine; actinide solubilities include organics (complexes with man-made organic ligands); solubilities were calculated assuming equilibrium with Mg-bearing minerals (brucite and hydromagnesite)
PHUMOX3[1] PHUMOX4 PHUMOX5 PHUMOX6	PHUMSIM	Proportionality constant for concentration of actinides associated with mobile humic colloids; in Salado brine; actinide solubilities include organics (complexes with man-made organic ligands); solubilities were calculated assuming equilibrium with Mg-bearing minerals (brucite and hydromagnesite)
TH+4, U+4, U+6, NP+4, NP+5, PU+3, PU+4, AM+3	CAPMIC	Maximum (cap) concentration of actinide associated with mobile microbes

Material	Property	Brief Description of Parameter
TH+4, U+4, U+6, NP+4, NP+5, PU+3, PU+4, AM+3	CAPHUM	Maximum (cap) concentration of actinide associated with mobile humic colloids

[1] Proportionality constant for actinide concentrations associated with mobile humic substances for PHUMOX3, for actinide elements with oxidation state III (that is, Pu(III) and Am(III)); PHUMOX4, oxidation state IV (Th(IV), U(IV), Np(IV), and Pu(IV)); PHUMOX5, oxidation state V (Np(V)); and PHUMOX6, oxidation state VI (U(VI)).

Table GEOCHEM-28. WIPP Colloid Parameter Values Used in CRA-2026 Final-State (FS) and Interim-State (IS) (Kaplan et al. 2025; Mariner 2025a, 2025b).

Actinide	CONCMIN[1]	CONCINT[1]	PROPMIC[2]	CAPMIC[1]	PHUMSIM[2]	PHUMCIM[2]	CAPHUM[1]
Th(IV)	2.6×10^{-8}	4.8×10^{-7}	3.1	6.95×10^{-4}	0.01 (FS) 0.02 (IS)	0.01	1.1×10^{-5}
U(IV)	2.6×10^{-8}	1.4×10^{-6}	0.0021	9.65×10^{-6}	0.01 (FS) 0.02 (IS)	0.01	1.1×10^{-5}
U(VI)	2.6×10^{-8}	1.4×10^{-6}	0.0021	9.65×10^{-6}	0.12[3]	0.51[3]	1.1×10^{-5}
Np(IV)	2.6×10^{-8}	4.3×10^{-8}	12	1.52×10^{-7}	0.01 (FS) 0.02 (IS)	0.01	1.1×10^{-5}
Np(V)	2.6×10^{-8}	4.3×10^{-8}	12	1.52×10^{-7}	0.00091[3]	0.0074[3]	1.1×10^{-5}
Pu(III)	2.6×10^{-8}	4.3×10^{-8}	2.92	4.97×10^{-7}	0.3	0.4 (FS) 0.3 (IS)	1.1×10^{-5}
Pu(IV)	2.6×10^{-8}	4.3×10^{-8}	0.3	4.07×10^{-9}	0.01 (FS) 0.02 (IS)	0.01	1.1×10^{-5}
Am(III)	2.6×10^{-8}	6.7×10^{-7}	2.92	4.97×10^{-7}	0.3	0.4 (FS) 0.3 (IS)	1.1×10^{-5}

[1] In units of moles colloidal actinide per liter

[2] In units of moles colloidal actinide per mole dissolved actinide

[3] Original CCA values

GEOCHEM-5.3.1 Mineral Fragment Colloids Model Parameterization

The CCA mineral fragment colloid stability experiments in factor-of-10 diluted WIPP brines (Appendix GEOCHEM-5.2.1 Mineral Fragment Colloids Process Model) provides a geometric mean of 1.3×10^{-9} M of mineral fragment colloid actinide sites for the hematite, goethite, and bentonite colloids (Papenguth 1996). These measurements were obtained after 12.8 to 12.9 days of equilibration. This mean value assumes, for Equation (GEOCHEM.26), an adsorption site density N_s of 1 nm^{-2}.

The f_a and f_c factors (Appendix GEOCHEM-5.2.1 Mineral Fragment Colloids Process Model) are assumed to be 2 for f_a to account for additional natural colloids potentially existing in the

Culebra, and 10 for f_c to account for uncertainty, mainly due to uncertainty in the adsorption site density (U.S. DOE 1996, Appendix SOTERM, Section SOTERM-6.3.1).

The product of these values (1.3×10^{-9} M × 2 × 10) is CONCMIN, 2.6×10^{-8} M (Table GEOCHEM-28).

GEOCHEM-5.3.2 Intrinsic Colloids Model Parameterization

During the development of the WIPP colloid model for the CCA, a review of the literature and experimental studies conducted at Lawrence Livermore National Laboratory indicated that Pu(IV) was the only actinide and oxidation state in the WIPP waste PAIR inventory that could potentially form a significant concentration of intrinsic colloids under the alkaline conditions expected in the repository (U.S. DOE 1996, Appendix SOTERM, Section SOTERM-6.3.2). Based on that work, a value of 1×10^{-9} M was chosen as the Pu(IV) CONCINT value for the CCA. The value of CONCINT was set to zero for all other actinides and oxidation states.

Since the CCA, studies have indicated that intrinsic colloids could potentially occur for each actinide in WIPP brines and for Pu at concentrations higher than 1×10^{-9} M. Intrinsic colloids are implemented in PA as element-specific values though their solubilities may depend on oxidation state. For different intrinsic colloid solubility values for an actinide among its oxidation states, the higher value is used for CONCINT.

For CRA-2026, the CONCINT values for Th and Am are set in accordance with the following requests by EPA (2022):

- Increase the Th intrinsic colloid concentration from 4.3×10^{-8} M (Reed et al. 2019) to a value of 4.8×10^{-7} M (U.S. EPA 2022, Section 8.1.5), which appears to be more consistent with the Th(IV) experimental data considered in the WIPP PA (Altmaier et al. 2004; Borkowski, 2012).
- Increase the Am intrinsic colloid concentration from 9.5×10^{-9} M, used in the CRA-2019 PA calculations (Reed et al., 2019), to 6.7×10^{-7} M (U.S. EPA 2022; Section 8.1.4), which is the upper bound concentration for the long-term Nd(III) solubility experiments carried out by Borkowski et al. (2010) and revisited by Reed et al. (2013).

These changes are addressed in Kaplan et al. (2025).

The CONCINT values for U, Np, and Pu in Table GEOCHEM-28 have not changed since CRA-2019. They were established based on data in Reed et al. (2013). The recommendation for those values is documented in Reed et al. (2019).

GEOCHEM-5.3.3 Humic Colloids Model Parameterization

The humic colloid proportionality constants used in the WIPP PA (i.e., PHUMCIM and PHUMSIM) are defined as

$$\text{PHUMCIM} = \frac{[\text{AnHs}]_C}{[\text{An}]_C} \quad \text{(GEOCHEM.33)}$$

$$\text{PHUMSIM} = \frac{[\text{AnHs}]_S}{[\text{An}]_S} \quad \text{(GEOCHEM.34)}$$

where $[\text{An}]_C$ and $[\text{An}]_S$ are the total dissolved actinide source term concentrations for the Castile and Salado brines, respectively. Substituting the process model complexation equation for [AnHs] (Appendix GEOCHEM-5.2.3 Humic Substance Colloids Process Model) gives:

$$\text{PHUMCIM} = \frac{\beta_{1:An^{m+}}[An^{m+}]_C[Hs_{tot}]}{[An]_C\left(\beta_{1:An^{m+}}[An^{m+}]_C + \beta_{1:Ca^{2+}}\left([Ca^{2+}]_C + [Mg^{2+}]_C\right)+1\right)} \quad \text{(GEOCHEM.35)}$$

$$\text{PHUMSIM} = \frac{\beta_{1:An^{m+}}[An^{m+}]_S[Hs_{tot}]}{[An]_S\left(\beta_{1:An^{m+}}[An^{m+}]_S + \beta_{1:Ca^{2+}}\left([Ca^{2+}]_S + [Mg^{2+}]_S\right)+1\right)} \quad \text{(GEOCHEM.36)}$$

The values for [An], $[An^{m+}]$, $[Ca^{2+}]$, and $[Mg^{2+}]$ for each brine are calculated by the Dissolved Actinide Source Term model (Appendix GEOCHEM-4.0 Dissolved Actinide Source Term). The value of $\beta_{1:An^{m+}}$ comes from the literature or is derived from experimental data (U.S. DOE 1996, SOTERM.6.3.3; Mariner 2016; Mariner 2018). A value of $10^{3.0}$ is used for $\beta_{1:Ca^{2+}}$ (Mariner 2016, Section 4.2.1). $[Hs_{tot}]$ is CAPHUM. CAPHUM is set at 1.1×10^{-5} M (U.S. DOE 1996, SOTERM.6.3.3.2). A conservative simplifying assumption included in these model equations is that there is no competition by other actinides or cations for the humic complexation sites. Additionally, the values used in the equations are conservative, as addressed in Section GEOCHEM-5.4.3.

The PHUMSIM and PHUMCIM proportionality constants depend on actinide oxidation state, not the actinide. The values for oxidation states V and VI have not changed since the CCA (U.S. DOE 1996, Table SOTERM-14). Values have changed, however, for oxidation states III and IV due to new data (Domski 2025a; Domski 2025b), process model updates (Mariner 2016; Mariner 2018), and recalibration of process model stability constants and proportionality constants resulting from updates to the WIPP thermodynamic database (Mariner 2023). The values of PHUMSIM and PHUMCIM for oxidation states III and IV in Table GEOCHEM-28 are updated for CRA-2026 (Mariner 2025a; Mariner 2025b).

Determination of the PHUMSIM and PHUMCIM values for An(IV) was updated for CRA-2026 by calculating a linear regression between pH and the humic complexation stability constant and using that equation to determine the stability constants used in the process model calculations (Mariner 2025a). PHUMSIM and PHUMCIM values are determined using the process model and the results of the baseline solubility analyses (e.g., pH, ionic strength, and concentrations of Ca^{+2}, Mg^{+2}, free actinide, and total dissolved actinide) and rounding up the results to the nearest single significant figure, in accordance with the previously established conservative methodology.

The difference in the PHUMSIM value for An(IV) between the Interim-State and Final-State is a result of differences in the CRA-2026 baseline solubility calculations for the two states (Domski 2025a; Domski 2025b). The free Th^{+4} species concentration is significantly higher in the Interim-State calculations. This increase causes the process model calculation for PHUMSIM to exceed 0.01. Rounding up to the nearest single significant figure, in accordance with the established methodology, caused the PHUMSIM value to increase from 0.01 to 0.02 (Mariner 2025b).

The An(V) PHUMSIM and PHUMCIM values are low (9.1×10^{-4} and 7.4×10^{-3}, respectively) and imply that humic-bound An(V) concentrations are less than 1% of the total dissolved An(V) source term concentration. Updating the An(V) humic colloid process model from the CCA model, as done for An(III) and An(IV) (Appendix GEOCHEM-5.2.3 Humic Substance Colloids Process Model), would likely reduce An(V) PHUMSIM and PHUMCIM values further, primarily because of the higher humic complexation stability constant used for Ca and Mg (Appendix GEOCHEM-5.4.3 Humic Colloids Model Uncertainty).

Until CRA-2026, the dissolved U(VI) source term concentration was set at 10^{-3} M. That concentration rendered humic-bound U(VI) concentrations essentially inconsequential in the WIPP PA calculations because the CAPHUM value (1.1×10^{-5} M) prevented humic-bound U(VI) concentrations from exceeding 1.1% of the dissolved U(VI) source term concentration. With a much lower dissolved U(VI) source term concentration for CRA-2026 (3.0×10^{-6} M as recommended in Kaplan et al. (2025)), the humic-bound U(VI) concentration decreases substantially; however, it becomes a significant component of the much lower total mobile U(VI) concentration.

The WIPP PA calculates the concentrations of actinides bound to dissolved humic colloids from the following equations:

$$[\mathrm{AnHs}]_C = \min(\mathrm{CAPHUM}, [\mathrm{An}]_C * \mathrm{PHUMCIM}) \qquad \text{(GEOCHEM.37)}$$

$$[\mathrm{AnHs}]_S = \min(\mathrm{CAPHUM}, [\mathrm{An}]_S * \mathrm{PHUMSIM}) \qquad \text{(GEOCHEM.38)}$$

As indicated, the lower value between CAPHUM and the product of [An] and the proportionality constant is used for the humic-bound actinide concentration. This prevents the humic-bound actinide concentration from exceeding CAPHUM for a given actinide.

GEOCHEM-5.3.4 Microbial Colloids Model Parameterization

In the WIPP PA, the affinity of dissolved actinide for microbial colloid surface sites is linear. This affinity is represented by PROPMIC

$$\mathrm{PROPMIC} = \frac{[\mathrm{AnMc}]}{[\mathrm{An}]} \qquad \text{(GEOCHEM.39)}$$

where [AnMc] is the total actinide concentration bound to mobile microbial colloids and [An] is the total dissolved actinide concentration calculated by the Dissolved Actinide Source Term model (Appendix GEOCHEM-4.0 Dissolved Actinide Source Term). In PA, this relationship is used to calculate [AnMc] from known values of PROPMIC and [An], except when the value exceeds CAPMIC, in which case CAPMIC sets the value of [AnMc].

The PROPMIC and CAPMIC values are specific to actinide and oxidation state. For CRA-2026, the original PROPMIC values from the CCA are applied, except for An(III) (Kaplan et al. 2025). Except for cases like An(III) in which DOE provides sufficient experimental data to justify updated PROPMIC values, EPA recommends applying the original PROPMIC values because they "bound the variability found in the literature" (EPA 2022, Section 8.3). The new PROPMIC value for An(III) is the result of experiments with Nd(III), an analog of Am(III) and Pu(III), and its interaction with WIPP microbial isolates in sodium chloride solutions and simulated WIPP brines (Swanson 2022; Swanson et al. 2023; Swanson 2024). Differences in Nd uptake between ERDA-6 and GWB brines indicate significant competition between Nd and Mg for cell surface sites. Determination of the An(III) PROPMIC and CAPMIC values for CRA-2026 is described in Kaplan et al. (2025).

CAPMIC values are also updated for CRA-2026. EPA, after examining DOE's biomass-based approach, recommends reinstating the original CCA CAPMIC values recalculated to accommodate the biomass-based approach (Kaplan et al. 2025; EPA 2022, Section 8.3). A biomass concentration of 10^{12} cells/L is shown to be reasonably bounding (EPA 2022, Section 8.3; Swanson et al. 2019). For CRA-2026, CAPMIC values are set based on actinide association with archaea and bacteria observed experimentally and scaled to the assumed biomass concentration of 10^{12} cells/L (Kaplan et al. 2025, p. 19). The exception to this scaling is the Th(IV) CAPMIC value. Experimental conditions for Th(IV) association with microbes required special interpretation due to complications, including precipitation, observed in the experiments (Kaplan et al. 2025).

The WIPP PA calculates the concentrations of actinides bound to dissolved microbial colloids using the following equation:

$$[\text{AnMc}] = \min(\text{CAPMIC}, [\text{An}] * \text{PROPMIC}) \qquad \text{(GEOCHEM.40)}$$

As indicated, the lower value between CAPMIC and the product of [An] and PROPMIC is used for the microbial-bound actinide concentration. This prevents the microbial-bound actinide concentration from exceeding CAPMIC for a given actinide and oxidation state.

GEOCHEM-5.4 Quantification of Uncertainty in the Colloids Source Term Model

GEOCHEM-5.4.1 Mineral Fragment Colloids Model Uncertainty

The mineral fragment colloids process model sets a conservative value of 2.6×10^{-8} M for the concentration of an actinide bound to mineral fragment colloids, CONCMIN. This value conservatively assumes (Mariner and Sassani 2014, Section 5.1.4.5).

1. Mineral fragment colloid sites will occur in the repository at concentrations observed in dilute brines in short-term (12 to 13 days) mineral fragment colloid stability experiments (Papenguth and Behl 1996). Mineral fragment colloid concentrations in natural systems and simple salt solutions are observed to be very low at high ionic strength (Alexander et al. 2011, Figure 5.1) suggesting mineral fragment colloid site concentrations will likely be orders of magnitude lower than CONCMIN.
2. The actinide sorption site density is 10 nm^{-2}, after including the factor of 10 uncertainty factor f_c (Appendix GEOCHEM-5.3.1 Mineral Fragment Colloids Model Parameterization).
3. Colloid sorption sites are fully loaded with actinides.
4. There is no competition among actinides for sorption sites (i.e., 2.6×10^{-8} M for each actinide).

Based on the conservative assumptions listed above, the 2.6×10^{-8} M mineral fragment colloid concentration used in the WIPP PA model is extremely high for water with ionic strength as high as the ionic strength of WIPP brines, likely by orders of magnitude. Because this value is extreme and conservative, uncertainty is not quantified and propagated in the WIPP PA model for mineral fragment colloids.

GEOCHEM-5.4.2 Intrinsic Colloids Model Uncertainty

The intrinsic colloids process model sets conservative values for CONCINT for each actinide. The conservative assumptions include:

1. Highest observed values from applicable studies are selected for CONCINT though the range of measurements may be broad.
2. For actinides with multiple oxidation states, the higher solubility is selected for CONCINT for all oxidation states.

Based on these conservative assumptions, the intrinsic colloid concentrations used in the WIPP PA model are either the highest observed values among measurements over a fairly broad range of experimental conditions or are applied equally to oxidation states that are less favorable to intrinsic colloid formation and stability. Because these intrinsic colloid concentrations are bounding and conservative, uncertainty is not quantified and propagated in the WIPP PA model for intrinsic colloids.

GEOCHEM-5.4.3 Humic Colloids Model Uncertainty

The humic colloids process model sets conservative values for all three parameters used in the WIPP PA: CAPHUM, PHUMSIM, and PHUMCIM.

The CAPHUM value of 1.1×10^{-5} M, determined by multiplying the concentration of humic colloids (2 mg L^{-1}) by the maximum measured site binding capacity (5.56 meq g^{-1}) (U.S. DOE 1996, SOTERM.6.3.3.2), ensures that the humic-bound concentration of an actinide species does not exceed the capacity of available humic colloids. This value is conservative because

1. The concentration of humic and fulvic acids in WIPP brines in the presence of MgO is likely much lower than 2 mg L^{-1}. Experiments show that humic acid concentrations in simulated brines from the Salado and Castile drop below a detection limit of approximately 1-2 mg L^{-1} within about 60 days in the presence of MgO (Wall and Mathews 2005).
2. The selected site binding capacity of 5.56 meq g^{-1} is the highest value measured among the three humic substances studied for the CCA (HAal-LBr, HAal-Gor, and FA-Suw). For those experiments, pH values were set at 4.8 and 6 to maximize actinide complexation.
3. Competition between actinides for binding sites is ignored, allowing the total effective loading for five actinides to increase above a total of 1.1×10^{-5} M.

For An(III) and An(IV), the PHUMSIM and PHUMCIM values are conservative because

1. The process model conservatively assumes that the humic colloids are composed only of humic acid. Humic acid has a significantly greater affinity for complexing actinides than fulvic acid (e.g., Sonke and Salters 2006; Stern et al. 2007; Mariner and Sassani 2014, Sections 4.2.3 and 5.3.4.2). Humic colloids in natural groundwater are a combination of humic and fulvic acids (Buffle et al. 1988).
2. The values used for the stability constant for actinide-humic complexation are derived at lower ionic strength and are not adjusted to the ~6 molar ionic strength of WIPP brines (e.g., Mariner 2016, Section 5.2; Mariner 2018, Section 5.1). High ionic strength tends to reduce humic complexation stability constants (Laszak and Choppin 2001, Fig. 4; Sonke and Salters 2006, Eq. 9).
3. To guard against overestimation of competition by calcium and magnesium for the available humic complexation sites, the values used for the stability constants for Ca-humic and Mg-humic complexation are set significantly lower than observed at the expected high ionic strength and pH of the MgO-equilibrated brines (Laszak and Choppin 2001; Mariner 2016, Section 5.2; Mariner 2018, Section 5.1).
4. Finally, the maximum [AnHs]:[An] ratios calculated by the process models for 1×, 3×, and 5× minimum brine volumes are rounded up to the nearest single significant figure or order of magnitude.

For An(V), the PHUMSIM and PHUMCIM values are conservative because

1. As in the case of An(III) and An(IV), the process model conservatively assumes that the humic colloids are composed only of humic acid, which has greater affinity for complexing actinides than fulvic acid. The humic complexation stability constant for An(V) is taken from experiments involving humic acid (U.S. DOE 1996, SOTERM.6.3.3.1; Kim and Sekine 1991).
2. As in the case of An(III) and An(IV), the stability constant used in the process model for An(V) humic complexation is for low ionic strength (0.1 M) and is not adjusted for high ionic strength, which tends to reduce stability constants.

For both An(V) and An(VI), the PHUMSIM and PHUMCIM values are conservative because

1. A low value for the stability constant for Ca and Mg complexation ($\log \beta_{1:Ca} = 2$) is used in the process model to calculate the An(V) PHUMSIM and PHUMCIM values (U.S. DOE 1996, SOTERM.6.3.3.1). At pcH 9.06 to 9.71 in NaCl solutions of 1 to 5 M, $\log \beta_{1:Ca^{2+}}$ is found to be in the range of 3.3 to 3.7 for Aldrich humic acid (Laszak and Choppin 2001, Table 3).

Based on the conservative assumptions identified above for the humic colloid process models, especially for the CAPHUM value and the values of stability constants used for high ionic strength WIPP brines, the humic colloid models used in the WIPP PA model produce extreme overestimates of humic colloid actinide concentrations for WIPP brines. Because these concentrations are demonstrably extreme and conservative, uncertainty in the humic colloid model parameters is not quantified and propagated in the WIPP PA model.

GEOCHEM-5.4.4 Microbial Colloids Model Uncertainty

The microbial colloids process model sets conservative values for PROPMIC and CAPMIC. The conservative assumptions include (Kaplan et al. 2025):

1. Competition between actinides for surface binding sites on microbial colloids is ignored.
2. Experiments count all microbes in suspension in the solutions although a significant fraction of the microbes might be considered immobile. For example, all cells in the Nd experiments settled out of suspension over time.
3. Current (and former) studies do not distinguish between precipitated actinides and actinides associated with microbes.
4. Experiments generally use uncomplexed actinides, not actinide solutions in which there might be other complexants such as EDTA, as in the case of dissolved actinide source term calculations.

Based on the conservative assumptions, especially the assumption that all microbes in laboratory experiments are mobile despite observed settling, microbial colloid concentrations calculated in the WIPP PA model are extreme and bounding. Because the microbial colloid concentrations established for the WIPP PA model are bounding and conservative, uncertainty is not quantified and propagated in the WIPP PA model for microbial colloids.

GEOCHEM-5.5 Summary of Updates since CRA-2019

The WIPP colloid model was developed for the CCA (U.S. DOE 1996, Appendix SOTERM, Section SOTERM.6.3). For CRA-2014, the WIPP PA intrinsic colloid and microbial colloid enhancement parameter values were updated based on new information (U. S. DOE 2014, Appendix SOTERM-2014, Sections SOTERM-3.9.2 and SOTERM-4.6). For CRA-2019, there were changes to the values of the An(III) and An(IV) proportionality constants for humic substance colloids and to the implementation of the microbial colloids model (U.S. DOE 2019, Appendix GEOCHEM-2019).

Since GEOCHEM-2019, the updates to the WIPP PA colloid models are as follows:

Mineral fragment colloids

- No changes

Intrinsic colloids

- Updated CONCINT values for Th and Am, as provided by the EPA

Humic colloids

- Added a regression equation in the process model to improve calculation of An(IV)-humic complexation stability constants as a function of pH
- Updated PHUMSIM and PHUMCIM values for An(III) and An(IV) due to their dependence on Dissolved Actinide Source Term calculations

Microbial colloids

- Changed PROPMIC values to CCA values for all but An(III), as requested by the EPA
- Updated PROPMIC and CAPMIC for An(III) based on Nd experimental data
- Updated CAPMIC values for other oxidation states and actinides based on biomass assumptions

GEOCHEM-6.0 REFERENCES

Abdel-Fattah, A. I., D. Zhou, H. Boukhalfa, S. Tarimala, D. Ware, and A. A. Keller. 2013. Dispersion stability and electrokinetic properties of intrinsic plutonium colloids: Implications for subsurface transport. Environmental Science & Technology, 47, pp. 5626-5634.

Alexander, W. R., J. A. Berry, M. J. Kelly, and S. W. Swanton. 2011. Review of colloids in the geosphere and their treatment in performance assessments. Report to NDA-RWMD. Serco Ltd., Oxfordshire, UK. NPO003512.

Altmaier, M., V. Neck, R. Müller, and T. Fanghänel. 2005. Solubility of $ThO_2 \cdot xH_2O$(am) in Carbonate Solution and the Formation of Ternary Th(IV) Hydroxide-Carbonate Complexes. Radiochimica Acta, 93, pp. 83-92.

Altmaier, M., V. Neck, and Th. Fanghänel. 2004. Solubility and Colloid formation of Th(IV) in concentrated NaCl and MgCl2 Solutions. Radiochimica Acta, 92, pp. 537-543.

Altmaier, M., V. Neck, M. A. Denecke, R. Yin, and T. Fanghänel. 2006. Solubility of $ThO_2 \cdot xH_2O$(am) and the Formation of Ternary Th(IV) Hydroxide-Carbonate Complexes in $NaHCO_3$-Na_2CO_3 Solutions Containing 0–4 M NaCl. Radiochimica Acta, 94, pp. 495-500.

Beam, J. C. 2022. Actinide (III/IV) – Silica Colloids in the WIPP. LCO-ACP-27, Revision 0. Carlsbad, NM: Los Alamos National Laboratory (November 7, 2022). LA-UR-22-31798.*

Bennett, D., Y. Wang, and T. Hicks. 1996. Memo to Distribution. Subject: An Evaluation of Heat Generation Processes for the WIPP. August 20, 1996. Albuquerque, NM: Sandia National Laboratories. ERMS 240635.

Borkowski, M., M. Richmann, D. T. Reed, and Y. Xiong. 2010. Complexation of Nd(III) with Tetraborate Ion and Its Effect on Actinide(III) Solubility in WIPP Brine. Radiochimica Acta, 98: 9-11 (Migration 2009), pp. 577–582.

Borkowski, M. 2012. Numerical Values for Graphs Presented in Report LCO-ACP-17 Entitled Solubility of An(IV) in WIPP Brine: Thorium Analog Studies in WIPP Simulated Brine, and for Graphs Published in Borkowski, M., et al., Radiochimica Acta, 98 (9-11), 577–582 (2010). LANL-CO ACRSP ACP-01/2012, Rev.0. Carlsbad, NM: Los Alamos National Laboratory. LA-UR 12–26640.

Brunell, S. 2025. Memo to Records Center. Subject: Update to CRA-2026 PA Parameters Due to Revised WIPP Repository Dimensions. April 7, 2025. Carlsbad, NM: Sandia National Laboratories.*

Brush, L. H., and Y. Xiong. 2003a. Calculation of Actinide Solubilities for the WIPP Compliance Recertification Application. Carlsbad, NM: Sandia National Laboratories (May 8, 2003). ERMS 529131.

Brush, L. H., and Y. Xiong. 2003b. Calculation of Actinide Solubilities for the WIPP Compliance Recertification Application. AP-098. Carlsbad, NM: Sandia National Laboratories (March 20, 2003). ERMS 526862.

Brush, L. H., and Y. Xiong. 2003c. Calculation of Actinide Solubilities for the WIPP Compliance Recertification Application. AP-098, Rev. 1. Carlsbad, NM: Sandia National Laboratories (April 15, 2003). ERMS 527714.

Brush, L. H., and Y. Xiong. 2003d. Calculation of Organic Ligand Concentrations for the WIPP Compliance Recertification Application. Carlsbad, NM: Sandia National Laboratories (April 14, 2003). ERMS 527567.

Brush, L. H. 2005. Results of Calculations of Actinide Solubilities for the WIPP Performance Assessment Baseline Calculations. Carlsbad, NM: Sandia National Laboratories (May 18, 2005). ERMS 539800.

Brush, L.H., and J.W. Garner. 2005. Memo to D.S. Kessel. Subject: Additional Justification of the Insignificant Effect of Np on the Long-Term Performance of the WIPP. February 1, 2005. Carlsbad, NM: Sandia National Laboratories. ERMS 538533.

Brush, L. H., and Y. Xiong, 2005a. Calculation of Actinide Solubilities for the WIPP Performance-Assessment Baseline Calculations. AP-120, Rev. 0. Carlsbad, NM: Sandia National Laboratories (April 4, 2005). ERMS 539255.

Brush, L. H., and Y. Xiong. 2005b. Calculation of Organic-Ligand Concentrations for the WIPP Performance-Assessment Baseline Calculations. Carlsbad, NM: Sandia National Laboratories (May 4, 2005). ERMS 539635.

Brush, L.H., and G.T. Roselle. 2006. Geochemical Information for Calculation of the MgO Effective Excess Factor. Carlsbad, NM: Sandia National Laboratories, pp. 36.*

Brush, L. H., Y.-L. Xiong, and J. Long. 2009. Results of the Calculations of Actinide Solubilities for the CRA-2009 PABC. Analysis Report. Carlsbad, NM: Sandia National Laboratories (October 7, 2009). ERMS 552201.

Brush, L. H., and P. S. Domski. 2013. Prediction of Baseline Actinide Solubilities for the WIPP CRA-2014 PA. Analysis Report. Carlsbad, NM: Sandia National Laboratories (January 21, 2013). ERMS 559138.

Buck, E. and D. C. Sassani. 2007. Waste Form and In-Drift Colloids-Associated Radionuclide Concentrations: Abstraction and Summary. MDL-EBS-PA-000004 REV 03. Albuquerque, NM: Sandia National Laboratories.

Buffle, J., K. J. Wilkinson, S. Stoll, M. Filella, & J. Zhang. 1998. A generalized description of aquatic colloidal interactions: the three-colloidal component approach. Environmental Science & Technology, 32: 19, pp. 2887-2899.*

Clayton, D. J. 2008. Memo to Larry Brush. Subject: Update to the Calculation of the Minimum Brine Volume for a Direct Brine Release. April 2, 2008. Carlsbad, NM: Sandia National Laboratories. ERMS 548522.

Clayton, D.J. 2013. Memo to Records Center. Subject: Justification of Chemistry Parameters for Use in BRAGFLO for AP-164, Revision 1. March 13, 2013. Carlsbad, NM: Sandia National Laboratories. ERMS 559466.

Day, B. 2015. Memo to Records Center. Subject: Review of the Technical Basis for REFCON: ASDRUM, DRROOM, and VROOM Performance Assessment Analysis Parameters with Comparison to the Currently Emplaced Steel Surface Area per Unit Volume in the WIPP Repository. September 15, 2015. Carlsbad, NM: Sandia National Laboratories. ERMS 564670.*

Day, B. 2019. Memo to Records Center. Subject: Reassessment of Need and Parameter Justification for Modeling Gas Generation due to Radiolysis of Brine and Cellulose/Plastic/Rubber in WIPP for CRA-2019. February 12, 2019. Carlsbad, NM: Sandia National Laboratories. ERMS 570873.

Derjaguin, B. V. and L. Landau. 1941. Theory of stability of strongly charged lyophobic sols and of the adhesion of strongly charged particles in solutions of electrolytes. Acta Physicochim, 17, pp. 633-662.

Docherty, P. 2024. Memo to Records Center. Subject: Update to WIPP PA Parameter DBRMINBV. April 30, 2024. Carlsbad, NM: Sandia National Laboratories. ERMS 581499.*

Domski, P. S. 2018. Memo to Records Center. Subject: Recommended Ranges of pcH, Ionic Strength, Total Inorganic Carbon (TIC), and Carbon Dioxide Fugacity for WIPP Baseline Solubility Uncertainty Calculations. June 25, 2018. Carlsbad, NM: Sandia National Laboratory. ERMS 570102.

Domski, P. S. 2019. Memo to Records Center. Subject: Technical Aspects of the Baseline Solubility Model for the CRA-2019 PA. June 10, 2019. Carlsbad, NM: Sandia National Laboratories. ERMS 571535.

Domski, P. S. and C. Sisk-Scott. 2019. Prediction of Baseline Actinide Solubilities for CRA2019 with an Updated EQ3/6 Pitzer Thermodynamic Database, DATA0.FM4. Carlsbad, NM: Sandia National Laboratories (April 1, 2019). ERMS 571178.

Domski, P.S. 2022. Memo to Records Center. Subject: EPA Issue 23: Implementation of the Neck et al. (2009) Am(III) Model. July 21, 2022. Carlsbad, NM: Sandia National Laboratories. ERMS 577677.*

Domski, P.S. 2023a. An Update to the WIPP EQ3/6 Database DATA0.FM1 with the Creation of DATA0.FM6. Carlsbad, NM: Sandia National Laboratories. May 9, 2023. ERMS 579370.*

Domski, P. S. 2023b. Prediction of Baseline Actinide Solubilities for the Replacement Panels Planned Change Request (RPPCR) Performance Assessment. Carlsbad, NM: Sandia National Laboratories. May 30, 2023. ERMS 579503.*

Domski, P.S. and M. B. Nemer. 2023a. On the Occurrence and Solubility of the Magnesium Hydroxy-Chloride Phases: Phase 3 and Phase 5 in the WIPP Near-Field Environment. March 2, 2023. Carlsbad, NM: Sandia National Laboratories. SAND2023-01265O.*

Domski, P.S. and M. B. Nemer. 2023b. Memo to Records Center. Subject: Revised Literature Screening Criteria for the WIPP Actinide Solubility Uncertainty Analysis, Revision 1. March 2, 2023. Carlsbad, NM: Sandia National Laboratories. SAND2023-01264O.*

Domski, P.S. 2024. Memo to Records Center. Subject: The Silica Thermodynamic Model: Should it be Included in the WIPP Thermodynamic Database? November 6, 2024. Carlsbad, NM: Sandia National Laboratories.*

Domski, P.S. 2025a. Prediction of Baseline Actinide Solubilities for the 2026 WIPP Compliance Recertification Application Performance Assessment Interim-State Analysis (CRA-2026 IS). Carlsbad, NM: Sandia National Laboratories (June 26, 2025).*

Domski, P.S. 2025b. Prediction of Baseline Actinide Solubilities for the 2026 WIPP Compliance Recertification Application Performance Assessment Final-State Analysis (CRA-2026 FS). Carlsbad, NM: Sandia National Laboratories (April 3, 2025).*

Domski, P.S. 2025c. Uncertainty Analysis of Actinide Solubilities for the 2026 Compliance Recertification Application (CRA-2026). Carlsbad, NM: Sandia National Laboratories (March 13, 2025).*

Ekberg, C., Y. Albinsson, M. J. Comarmond, and P. L. Brown. 2000. Studies on the Complexation Behavior of Thorium(IV). 1. Hydrolysis Equilibria. Journal of Solution Chemistry, 29: 1.

Feng, M., and D. Kicker. 2025. Input Parameter Report for the 2026 Compliance Recertification Application Performance Assessment: Interim State Repository (CRA-2026 IS). Revision 0. Carlsbad, NM: Sandia National Laboratories (October 23, 2025).*

Francis, A. J., J. B. Gillow, and M. R. Giles. 1997. Microbial gas generation under expected Waste Isolation Pilot Plant repository conditions. Albuquerque, NM: Sandia National Laboratories. SAND 96-2582.

Gautier, Q., P. Bénézeth, V. Mavromatis, J. Schott. 2014. Hydromagnesite solubility product and growth kinetics in aqueous solution from 25 to 75°C. Geochim Cosmochim Acta, 138, pp. 1-20.*

Guillaumont, R., T. Fanghänel, J. Fuger, I. Grenthe, V. Neck, D.A. Palmer, and M.H. Rand. 2003. Update on the Chemical Thermodynamics of Uranium, Neptunium, Plutonium, Americium and Technetium. Chemical Thermodynamics, 5. Amsterdam, Netherlands: Elsevier.

Hu, J. D., Y. Zevi, X. M. Kou, J. Xiao, X. J. Wang, and Y. Jin. 2010. Effect of dissolved organic matter on the stability of magnetite nanoparticles under different pH and ionic strength conditions. Science of the Total Environment, 408: 16, pp. 3477-3489.

Internation Commission on Radiological Protection. 2008. Nuclear Decay Data for Dosimetric Calculations. ICRP, 38: 3.*

Jang, J., P. Hora, L. Kirkes, C. Miller, and L. Zhang. 2021. Analysis Report documenting Solubility and Complexation of Iron, Lead, Magnesium, Neodymium, and Boron in the WIPP-Relevant Brines under TPs 06-03, 08-02, 12-02, 14-03, 14-05, 16-02, 19-01, and 20-01. Revision 0. Carlsbad, NM: Sandia National Laboratories (November 23, 2021). ERMS 576381. SAND2022-13723R.*

Jang, J., and I. Foli. 2023. Solubility and Complexation of Iron, Lead, Magnesium, Neodymium, Boron, and Calcium in Brines. Revision 1. Carlsbad, NM: Sandia National Laboratories. (February 1, 2023). ERMS 578806.*

Kaplan, U., J. Swanson, and C. K. Aslani. 2025. LANL ACRSP Parameter Recommendations for CRA-2026 Performance Assessment. LCO-ACP-41, Revision 1. Carlsbad, NM: Los Alamos National Laboratory (May 28, 2025).*

Kim, J. L. and T. Sekine. 1991. Complexation of neptunium(V) with humic acid. Radiochimica Acta, 55: 4, pp. 187-192.

King, S. 2021a. Memo to Records Center. Subject: Repository volume, DRZ volume, and minimum brine volume for a direct brine release for a repository with new panels. December 20, 2021. Carlsbad, NM: Sandia National Laboratories. ERMS 576475.*

King, S. 2021b. Memo to Records Center. Subject: Recalculation of iron surface area for iron corrosion in the WIPP PA calculation. December 15, 2021. Carlsbad, NM: Sandia National Laboratories. ERMS 576428.*

King, S., P. Docherty, and C. Hansen. 2023a. Impact Analysis of High Plutonium Loading in a Single WIPP Waste Panel. Revision 0. Carlsbad, NM: Sandia National Laboratories (November 8, 2023). ERMS 580466.*

King, S., C. Hansen, and P. Hora. 2023b. Memo to Records Center. Subject: Evaluation of radiolytic gas generation from adsorbed water and from CPR materials, Revision 1. June 21, 2023. Carlsbad, NM: Sandia National Laboratories. ERMS 579454. *

King, S. and T. Zeitler. 2025. Analysis Report for Parameter Sampling in the 2026 Compliance Recertification Application Performance Assessment. Revision 0. Carlsbad, NM: Sandia National Laboratories.*

Kirchner, T. B. 2013. Sensitivity of the CRA-2014 Performance Assessment Releases to Parameters. Sandia National Laboratories, Carlsbad NM (May 17, 2013). ERMS 560043.

Kirkes, G.R. 2019. Features, Events and Processes Assessment for the Compliance Recertification Application – 2019. Revision 0. Carlsbad, NM: Sandia National Laboratories (October 11, 2019). ERMS 571366.

Kutahyali Aslani, C. 2022. Solubility of An $(OH)_3$ am and An $(OH)_3$ cr in the presence of Citrate and EDTA. LCO-ACP-29, Revision 0. Los Alamos, NM: Los Alamos National Laboratory (November 30, 2022). LA-UR-22-32478.*

Laszak, I., and G. R. Choppin. 2001. Interaction study between Ca2+ and humic acids in brine media. Radiochimica Acta, 89: 10, pp. 653-659.

Mariner, P. E. and D. C. Sassani. 2014. Analysis report for WIPP colloid model constraints and performance assessment parameters. Carlsbad, NM: Sandia National Laboratories. SAND2014-1961.

Mariner, P. E. 2016. Actinide(IV)-Humic Complexation in the WIPP Performance Assessment. Carlsbad, NM: Sandia National Laboratories (October 13, 2016). ERMS 567222.

Mariner, P. E. 2018. Actinide(III)-Humic Complexation in the WIPP Performance Assessment. Carlsbad, NM: Sandia National Laboratories (March 29, 2018). ERMS 569599.

Mariner, P. E. 2023. Memo to Records Center. Subject: Updates to the WIPP humic colloids models for An(III) and An(IV). July 26, 2023. Carlsbad, NM: Sandia National Laboratories. ERMS 580251.*

Mariner, P. E. 2025a. Memo to Records Center. Subject: CRA-2026 FS updates to the WIPP humic colloids models for An(III) and An(IV). April 14, 2025. Carlsbad, NM: Sandia National Laboratories.*

Mariner, P. E. 2025b. Memo to Records Center. Subject: CRA-2026 IS updates to the WIPP humic colloids models for An(III) and An(IV). July 9, 2025. Carlsbad, NM: Sandia National Laboratories.*

McCormick, J., G. R. Kirkes., and C. Hansen. 2024. Conceptual Models in WIPP Performance Assessment. Carlsbad, NM: Sandia National Laboratories (October 8, 2024).*

Miller, C. 2022. EPA Technical Exchange: Thermodynamic Database Issue Resolution. Carlsbad, NM: Sandia National Laboratories (October 25, 2022). SAND2022-14863C. ERMS 578293.*

Moriyama, H., T. Sasaki, T. Kobayashi, and I. Takagi. 2005. Systematics of Hydrolysis Constants of Tetravalent Actinide Ions. Journal of Nuclear Science and Technology, 42: 7, pp. 626-635. DOI: 10.1080/18811248.2004.9726430.

Morss, L. R., and C. W. Williams. 1994. Synthesis of crystalline americium hydroxide, $Am(OH)_3$, and determination of its enthalpy of formation; estimation of the solubility-product constants of actinide (III) hydroxides. Radiochimica Acta, 66/67, pp. 89-93.

Moulin, C., B. Amekraza, S. Hubert, and V. Moulin. 2001. Study of Thorium Hydrolysis Species by Electrospray-Ionization Mass Spectrometry. Analytica Chimica Acta, 441, pp. 269–79.

Narlesky, J.E., M.A. Stroud, P.H. Smith, D. M. Wayne, R. E. Mason, L.A. Worl. 2012. Characterization of Representative Materials in Support of Safe, Long Term Storage of Surplus Plutonium in DOE-STD-3013 Containers. Los Alamos, NM: Los Alamos National Laboratory. LA-UR-12-23790.*

Neck, V., and J. I. Kim. 2001. Solubility and hydrolysis of tetravalent actinides. Radiochimica Acta, 89, pp. 1-16.

Neck, V., R. Muller, M. Bouby, M. Altmaier, J. Rothe, M. A. Denecke, and J. I. Kim. 2002. Solubility of amorphous Th(IV) hydroxide - application of LIBD to determine the solubility product and EXAFS for aqueous speciation. Radiochimica Acta, 90: 9-11, pp. 485-494.

Neck, V., M. Altmaier, R. Muller, A. Bauer, T. Fanghänel, and J. I. Kim. 2003. Solubility of crystalline thorium dioxide. Radiochimica Acta, 91: 5, pp. 253-262.

Neck, V., M. Altmaier, and Th. Fanghänel. 2006. Ion Interaction (SIT) Coefficients for the Th4+ Ion and Trace Activity Coefficients in NaClO4, NaNO3 and NaCl Solution Determined by Solvent Extraction with TBP. Radiochimica Acta, 94, pp. 501–07.

Neck, V., M. Altmaier, T. Rabung, J. Luetzenkirchen, and T. Fanghänel. 2009. Thermodynamics of Trivalent Actinides and Neodymium in NaCl, $MgCl_2$, and $CaCl_2$ Solutions: Solubility, Hydrolysis, and Ternary Ca-M(III)-OH Complexes. Pure and Applied Chemistry, 81: 9, pp. 1555—1568.

Nemer, M. B., J. S. Stein, and W. Zelinski. 2005. Analysis Report for BRAGFLO Preliminary Modeling Results with New Gas Generation Rates Based Upon Recent Experimental Results. Carlsbad, NM: Sandia National Laboratories (April 20, 2005). ERMS 539437.

Nemer, M.B., and D.J. Clayton. 2008. Analysis Package for Salado Flow Modeling, 2009 Compliance Recertification Application Calculation. Carlsbad, NM: Sandia National Laboratories (April 9, 2008). ERMS 548607.

Nemer, M., Y. Xiong, A. E. Ismail, and J. Jang. 2011. Solubility of $Fe_2(OH)_3Cl$ (pure-iron end-member of hibbingite) in NaCl and Na_2SO_4 brines. Chemical Geology, 280, pp. 26-32.

Nemer, M.B. 2023a. Evaluation of the An(III)-Borate Interaction, Revision 1. Albuquerque, NM: Sandia National Laboratories. SAND2023-07488O. ERMS 580267.*

Nemer, M. B. 2023b. Alternatives to the Current Uncertainty Methodology. Albuquerque, NM. Sandia National Laboratories. ERMS 578712.*

Nemer, M.B. 2025. Memo to Records Center. Subject: MgO hydration rates for the CRA-2026 under AP-208. March 18, 2025. Albuquerque, NM: Sandia National Laboratories.*

Novak, C. F., and R. C. Moore. 1996. Memo to M.D. Siegel. Subject: Estimates of Dissolved Concentrations for +III, +IV, +V, and +VI Actinides in Salado and Castile Brine Under Anticipated Repository Conditions. March 28, 1996. WPO 36207. ERMS 236207.

Novak, C. F., R. C. Moore, and R. V. Bynum. 1996. Prediction of Dissolved Actinide Concentrations in Concentrated Electrolyte Solutions: A Conceptual Model and Model Results for the Waste Isolation Pilot Plant (WIPP). Proceedings of the International Conference on Deep Geological Disposal of Radioactive Waste, Winnipeg, Manitoba, Canada (September 16-19, 1996). ERMS 243072.

Novak, C.F. 1997. Memo to R.V. Bynum. Subject: Calculation of Actinide Solubilities in WIPP SPC and ERDA-6 Brines under MgO Backfill Scenarios Containing either Nesquehonite or Hydromagnesite as the Mg-CO3 Solubility-Limiting Phase. April 21, 1997. Albuquerque, NM: Sandia National Laboratories. ERMS 246124.

Okamoto, Y., Y. Mochizuki, and S. Tsushima. 2003. Theoretical study of hydrolysis reactions of tetravalent thorium ion. Chemical Physics Letters, 373, pp. 213–217.

Papenguth, H. W. 1996. Memo to C. T. Stockman. Subject: Parameter Record Package for Colloidal Actinide Source Term Parameters. May 7, 1996. Attachment A: Rationale for Definition of Parameter Values for Humic Substances. Carlsbad, NM: Sandia National Laboratories. ERMS 416348.

Papenguth, H. W., and Y. K. Behl. 1996. Test Plan for Evaluation of Colloid-Facilitated Actinide Transport at the Waste Isolation Pilot Plant. Test Plan TP 96-01. Carlsbad, NM: Sandia National Laboratories (January 16, 1996). ERMS 417319.

Pitzer, K. S. 1973. Thermodynamics of electrolytes. I. Theoretical basis and general equations. The Journal of Physical Chemistry, 77, pp. 268-277.

Popielak, R. S., R. L. Beauheim, S. R. Black, W. E. Coons, C. T. Ellingson, and R. L. Olsen. 1983. Brine Reservoirs in the Castile Formation, Waste Isolation Pilot Plant Project, Southeastern New Mexico. Carlsbad, NM: U.S. Department of Energy. TME 3153.

Powers, D. W., S. J. Lambert, S. E. Shaffer, I. R. Hill, and W. D. Weart, eds. 1978. Geological Characterization Report, Waste Isolation Pilot Plant (WIPP) Site, Southeastern New Mexico. 2 vols. Albuquerque, NM: Sandia National Laboratories. SAND78-1596. ERMS 205448.

Rai, D., D. A. Moore, C. S. Oakes, and M. Yui. 2000. Thermodynamic Model for the Solubility of Thorium Dioxide in the Na^+-Cl^--OH^--H2O System at 23 °C and 90 °C. Radiochimica Acta, 88, pp. 297-306.

Rai, D., M. Yui, D. A. Moore, G. J. Lumetta, K. M. Rosso, Y. Xia, A. R. Felmy, and F. N. Skomurski. 2008. Thermodynamic Model for ThO_2(am) Solubility in Alkaline Silica Solutions. Journal of Solution Chemistry, 37: 12, pp. 1725-1746.

Reed, D.T., S. Okajima, L.H. Brush, and M.A. Molecke. 1993. Radiolytically-Induced Gas Production in Plutonium-Spiked WIPP Brine, Scientific Basis for Nuclear Waste Management XVL Materials Research Society Symposium Proceedings, Boston, MA, November 30 - December 4, 1992, 294, pp. 431--438. Pittsburgh, PA: Materials Research Society. SAND92-7283C. ERMS 228637.

Reed, D., J. Swanson, J. F. Lucchini, and M. Richmann. 2013. Intrinsic, mineral and microbial colloid enhancement parameters for the WIPP actinide source term. LANL-CO ACRSP/LCO-ACP-18. Los Alamos, NM: Los Alamos National Laboratory (February 20, 2013). ACP-1302-09-17-01.

Reed, D. T., J. Swanson, and F. Stanley. 2019. LANL/ACRSP Parameter Recommendations for the CRA-2019 Deferred Performance Assessment. LANL-CO ACRSP/LCO-ACP-24. Los Alamos, NM: Los Alamos National Laboratory. LA-UR 19-22787

Reiller, P. E., N. D. M. Evans, and G. Szabo. 2008. Complexation parameters for the actinides(IV)-humic acid system: a search for consistency and application to laboratory and field observations. Radiochimica Acta, 96:6, pp. 345-358.

Roselle, G. T. 2013. Determination of Corrosion Rates from Iron/Lead Corrosion Experiments to be used for Gas Generation Calculations. Analysis Report, Revision 1. Carlsbad, NM: Sandia National Laboratories (January 23, 2013). ERMS 559077.

Simonnet, M., N. Barre, R. Drot, C. Le Naour, V. Sladkov, and S. Delpech. 2016. Multiparametric Study of Thorium Oxide Dissolution in Aqueous Media. Radiochimica Acta, 104: 10, pp. 691–700.

Snider, A. C. 2003. Verification of the Definition of Generic Weep Brine and the Development of a Recipe for This Brine. Carlsbad, NM: Sandia National Laboratories (April 22, 2003). ERMS 527505.

Sonke, J. E., and V. J. M. Salters. 2006. Lanthanide-humic substances complexation. I. Experimental evidence for a lanthanide contraction effect. Geochimica Et Cosmochimica Acta, 70: 6, pp. 1495-1506.

Stein, J. S. 2005. Memo to L. H. Brush. Subject: Estimate of Volume of Brine in Repository that Leads to a Brine Release. April 13, 2005. Carlsbad, NM: Sandia National Laboratories. ERMS 539372.

Stern, J. C., J. E. Sonke, and V. J. M. Salters. 2007. A capillary electrophoresis-ICP-MS study of rare earth element complexation by humic acids. Chemical Geology, 246: 3-4, pp. 170-180.

Swanson, J.S., C. Hazelton, F.E. Stanley, and D.T. Reed. 2019. Review of the Microbial Colloid Contribution to the WIPP Actinide Source Term. LCO-ACP-23, Rev. 0. Carlsbad, NM: Los Alamos National Laboratory (March 15, 2019). LA-UR-19-22310.

Swanson J. 2022. Biologically Influenced Transport of the +3 Actinide Oxidation State from the WIPP Environment, Using Neodymium as an Analog. LCO-ACP-32, Rev. 0. Carlsbad, NM: Los Alamos National Laboratory (December 14, 2022). LA-UR-22-32936.*

Swanson J., A. Navarrette, J. Knox, H. Kim, F. Stanley. 2023. Microbial Influence on the Mobility of +3 Actinides from a Salt-Based Nuclear Waste Repository. Microorganisms 2023, 11: 1370. 11061370.*

Swanson, J. 2024. Biologically Influenced Transport of the +3 Actinide Oxidation State from the WIPP Environment, Using Neodymium as an Analog. Report LCO-ACP-32, Revision 1. Carlsbad, NM: Los Alamos National Laboratory.*

Telander, M. R., and R. E. Westerman. 1993. Hydrogen Generation by Metal Corrosion in Simulated Waste Isolation Pilot Plant Environments: Progress Report for the Period November 1989 Through December 1992. Albuquerque, NM: Sandia National Laboratories. SAND92-7347. ERMS 223456.

Traexler, K. A., S. Utsunomiya, A. B. Kersting, and R. C. Ewing. 2004. Colloid transport of radionuclides: Yucca Mountain performance assessment. Scientific Basis for Nuclear Waste Management XXVII, Symposium held April 12-16, 2004, San Francisco, CA. Warrendale, PA: Materials Research Society, 807, 1-6.

Trovato, E.R. 1997. Untitled Letter to G. Dials. April 25, 1997. U. S. Environmental Protection Agency Office of Radiation and Indoor Air, Washington, DC.

U. S. Department of Energy (U.S. DOE). 1996. Title 40 CFR Part 191 Compliance Certification Application for the Waste Isolation Pilot Plant (October). Carlsbad, NM: Carlsbad Field Office. DOE/CAO-1996-2184.

U. S. DOE. 2004. Title 40 CFR Part 191 Compliance Recertification Application for the Waste Isolation Pilot Plant (March). Carlsbad, NM: Carlsbad Field Office. DOE/WIPP 2004-3231.

U. S. DOE. 2009. Title 40 CFR Part 191 Compliance Recertification Application for the Waste Isolation Pilot Plant. Carlsbad, NM: Carlsbad Field Office. DOE/WIPP 2009-3424.

U. S. DOE. 2014. Title 40 CFR Part 191 Subparts B and C Compliance Recertification Application for the Waste Isolation Pilot Plant. Carlsbad, NM: Carlsbad Field Office. DOE/WIPP 2014-3503.

U. S. DOE. 2019. Title 40 CFR Title 40 CFR Part 191 Subparts B and C Compliance Recertification Application for the Waste Isolation Pilot Plant. Carlsbad, NM: Carlsbad Field Office. DOE/WIPP 2019-3609.*

U. S. DOE. 2024a. Letter from DOE/M. Gerle to EPA/T. Peake Response 2 to U.S. Environmental Protection Agency's Questions on the Replacement Panels Planned Change Request. *

U. S. DOE. 2024b. Letter from DOE/M. Gerle to EPA/T. Peake. Response 3 to the U.S Environmental Protection Agency's Questions on the Replacement Panels Planned Changed Request.*

U. S. DOE. 2025. Letter from DOE/M. Gerle to EPA/T. Peake Response 7 to U.S. Environmental Protection Agency's Questions on the Replacement Panels Planned Change Request.*

U. S. Environmental Protection Agency (U.S. EPA). 1998. Technical Support Document for Section 194.24: EPA's Evaluation of DOE's Actinide Source Term, Environmental Protection Agency: Office of Radiation and Indoor Air. Washington DC. Docket A-93-02, Item V-B-17.

U. S. EPA. 2006. Technical Support Document for Section 194.24: Evaluation of the Compliance Recertification – Actinide Source Term and Culebra Dolomite Distribution Coefficient Values. Washington, DC: U.S. Environmental Protection Agency, Office of Air and Radiation. EPA Air Docket A 98-49, Item II B1-3.

U.S. EPA. 2017. Technical Support Document for Section 194.24: Evaluation of the Compliance Recertification Actinide Source Term, Backfill Efficacy, and Culebra Dolomite Distribution Coefficient Values. Washington, DC: Office of Air and Radiation. Docket: EPA-HQ-OAR-2014-0609.

U.S. EPA. 2022. Technical Support Document for Section 194.24: Evaluation of the Compliance Recertification (CRA-2019) Actinide Source Term, Gas Generation, Backfill Efficacy, Water Balance, Culebra Dolomite Distribution Coefficient Values. DOCKET: EPA-HQ-OAR-2019-0534-0052.*

Van Soest, G. 2025. Interim State Performance Assessment Inventory Report – 2024. INV-IPA-24, Revision 0. Carlsbad, NM: Los Alamos National Laboratory (May 27, 2025).*

Verwey, E. J. W., and J. T. G. Overbeek. 1948. Theory of the stability of lyophobic colloids. Amsterdam, Netherlands: Elsevier.

Wall, N. A., and S. A. Mathews. 2005. Sustainability of humic acids in the presence of magnesium oxide. Applied Geochemistry, 20, pp. 1704-1713.

Wang, Y., and L. H. Brush. 1996. Memo to M.S. Tierney. Subject: Estimates of Gas-Generation Parameters for the Long-Term WIPP Performance Assessment. January 26, 1996. Carlsbad, NM: Sandia National Laboratories. ERMS 231943.

Wang, Z., R. C. Moore, A. R. Felmy, M. J. Mason, and R. K. Kukkadapu. 2001. A study of the corrosion products of mild steel in high ionic strength brines. Waste Management 21: 335-341.

Wilson, C., D. Porter, J. Gibbons, E. Oswald, G. Sjoblom, and F. Caporuscio. 1996. Conceptual Models Supplementary Peer Review Report (December). Carlsbad, NM: Carlsbad Area Office. ERMS 243153.

Wolery, T.J., and R.L. Jarek. 2003. Software User's Manual: EQ3/6, Version 8.0. Albuquerque, NM: Sandia National Laboratories. Software Document No. 10813-UM-8.0-00.

Wolery, T. J., Y.-L. Xiong, and J. J. Long. 2010. Verification and Validation Plan/Validation Document for EQ3/6 Version 8.0a for Actinide Chemistry, Document Version 8.10. Carlsbad, NM: Sandia National Laboratories. ERMS 550239.

Xiong, Y.-L. 2011. E-mail to Jennifer Long. Subject: Release of EQ3/6 Database DATA0.FM1. March 9, 2011. Carlsbad, NM: Sandia National Laboratories. ERMS 555152.

Xiong, Y.-L, L. Kirkes, and C. Marrs. 2017. Long-Term Experimental Determination of Solubilities of Micro-Crystalline Nd (III) Hydroxide in High Ionic Strength Solutions: Applications to Nuclear Waste Management. Aquatic Geochemistry 23, pp. 359-375.

Zeitler, T. R., and C. Hansen. 2015a. Memo to Records Center. Cumulative distribution for STEEL:CORRMCO2.November 3, 2015. Carlsbad, NM: Sandia National Laboratories. ERMS 565009.

Zeitler, T. R., and C. Hansen. 2015b. Memo to Records Center. Subject: Updated calculation of the cumulative distribution for STEEL:HUMCORR. December 8, 2015. Carlsbad, NM: Sandia National Laboratories. ERMS 565108.

Zhao, P., and S. A. Steward. 1997. Literature review of intrinsic actinide colloids related to spent fuel waste package release rates. Livermore, CA: Lawrence Livermore National Laboratory. UCRL-ID-126039.